INVESTIGATION OF THE MECHANICAL BEHAVIOR OF CARBON FIBER- CARBON NANOFIBER COMPOSITE FOR ENERGY STORAGE APPLICATION IN FLYWHEEL

A Dissertation

by

JAMSHID KAVOSI

Submitted to the Office of Graduate and Professional Studies of
Texas A&M University
in partial fulfillment of the requirements for the degree of

DOCTOR OF PHILOSOPHY

Chair of Committee,	Mohammad Naraghi
Co-Chair of Committee,	Terry S. Creasy
Committee Members,	Hung-Jue Sue
	Matt Pharr
Head of Department,	Ibrahim Karaman

August 2020

Major Subject: Materials Science and Engineering

ABSTRACT

The main goal of this study is to unravel the mechanics of hybrid composite flywheels with carbon microfibers and carbon nanofibers (CNFs) reinforcements under centrifugal forces and evaluate the role of nanoscale fillers in delaying failure. This work is driven by the desire to more efficiently store energy in a flywheel in which the maximum energy density is limited by the ability of the material to withstand centrifugal forces. The limiting factor for flywheel energy storage is material strength since the flywheel will burst due to centrifugal stresses if spun at too high of angular velocity, yet its stored energy is proportional to the square of the rpm.

In a typical flywheel in which the fibers are placed in the hoop direction for ease in manufacturing, the energy storage and the maximum RPM is limited not by fiber failure, but by matrix-dominated failure modes especially in the hoop direction. To avoid such failures, our study is focused on improving the resin strength via nanomaterials, and to enhance the fracture toughness of hybrid composites in mode I.

 In this dissertation, we have studied the role of electrospun carbon nanofibers (CNFs) in the region of experiencing high radial stress in the composite flywheel. Three major objectives of this research study are I) identification of the trade-offs between surface functionalization of CNFs as a means to enhance CNF-matrix load transfer and the mechanics of individual carbon nanofiber, II) investigation of the mechanics of CNF/epoxy nanocomposite and hybrid nano/micro fiber-reinforced composites as a function of dispersion, surface chemistry and mechanics of individual CNFs, and III) investigation of the failure mechanisms of flywheel subjected to centrifugal forces as a function of the nanofillers content. The first two objectives were mainly carried out via experimentation, including material processing and characterization at multiple length scales,

while the last objective was mostly carried out via finite elements analysis based on input from the prior objectives.

Our studies pointed to an increase of at most 25% in the interlaminar fracture toughness of the carbon fiber composite laminate due to the introduction of CNFs mat interleafs. The study also points to distinct difficulties associated with increasing crack initiation and growth fracture toughness, as related to the least resistant crack growth path. Our computational results pointed to an increase in the energy density of the flywheel to about ~14% by introduction of the CNFs mat in the interlayer regions.

ACKNOWLEDGEMENTS

I would like to express my deepest appreciation to my advisor and committee chair, Dr. Mohammad Naraghi, who possesses an attitude of a genius, a spirit of adventure, a limitless energy and an infectious enthusiasm towards research. This dissertation would not be possible without his guidance, and encouragement. I would also like to thank my co-advisor Dr. Terry S. Creasy for his guidance and support throughout the course of this research and letting me use his lab to perform the experiments. Also, I would like to thank my committee members, Dr. H.J. Sue and Dr. Matt Pharr for their guidance throughout the course of this research study. I also would like to thank Dr. Alan Palazzolo and Dr. Reza Tafreshi for their limitless support throughout the course of this research study.

Thanks also go to my friends and lab members, Frank Gardea, Yijun Chen, Kai Morikawa, Sevketcan Sariyaka, Sumit Khatri and the department of Materials Science and Engineering faculty and staff for making my time at Texas A&M University a great experience. I also would like to thank Rodney Inmon for helping and assisting me to run an experiment. I would like to thank my friends for all the good times, Behrouz, Farid, Nima, and Farhad

Finally, thanks to my mother and father for their encouragement and to my sisters for their support.

CONTRIBUTORS AND FUNDING SOURCES

Contributors

This work was supervised by a dissertation committee consisting of Professor Mohammad Naraghi of the Department of Aerospace Engineering and Professor Terry S. Creasy, Hung-Jue Sue, and Matt Pharr of the Department of Materials Science and Engineering.

Funding Sources

NOMENCLATURE

σ_f	Fracture strength
E	Elastic modulus
G_c	Surface energy
α	Proportionality constant
K_{IC}	Fracture toughness
$a_{critical}$	Critical flaw size
V_f	Fiber volume fraction
E_f	Fiber elastic modulus
P_c	Load at the peak load
δ_c	Displacement at the peak load
w	Width of the specimen
E_f	Fiber elastic modulus
K	Shape factor
σ_u	Materials strength
ρ	Density
σ_r	Radial stress
ω	Angular velocity
ε_r	Radial strain
ε_θ	Circumferential strain
υ_L	Poisson's ratio

I	Moment of Inertia
E_L	Longitudinal modulus
E_T	Transverse modulus
P	Inner pressure
Q	Outer pressure
δ	Misfit

TABLE OF CONTENTS

LIST OF FIGURES

x

1. INTRODUCTION

Flywheel energy storage systems are a clean and efficient method that can meet the energy leveling demands. The energy is stored in a flywheel as kinetic energy by spinning the flywheel and released on demand [1]. These mechanical batteries have been around for over 100 years and were used in early industrial systems to store energy. Although the concept of storing energy in a rotating mass is an old idea, the relatively recent advent of advanced fiber composite materials offers a potential for improved energy storage and conversion using rotating electrochemical devices. Similar to other energy storage systems, such as electrochemical batteries, energy density (energy stored in the battery per its unit mass) is one of the main parameters which defines the battery's performance. The achievable energy density of a flywheels, such as a circumferentially wound ring or cylinder, is proportional to the material's specific strength. This proportionality favors using materials with high specific strength such as fiber composites to enhance the energy density of the flywheel. Recently, NASA intended to have composite flywheels in space station for energy storage [2]. Flywheels have been also proposed for satellite altitude control. There are also investigations of hybrid and all-electric combat vehicles and weapons. Composite flywheels are crucial part of their systems.

One of the earliest studies which demonstrates that composite materials with significantly large specific strength are well suited for the flywheel application was by Rabenhorst et al. [3] They reported that the use of the 70% graphite/epoxy for the flywheel outperform the flywheel fabricated with the steel that was considered to be the highest strength isotropic material for a flywheel rotor.

DeTeresa et al. [4] examined the performance of commercial high-performance reinforcement fibers for the application to flywheel power supplies and concluded that carbon

fibers are preferred for highest performance energy storage application. Alongside, the materials selection, proper design would also result in a better performance of the flywheel. Around this scheme, further research has been undertaken to study the additional improvement that could be made by modifying the design of the rotor or inducing certain residual stress state in some way.

However, many flywheel designs are limited not by fiber failure, but by matrix-dominated failure modes. The existing composite flywheels are running at near capacity and the faster spin speeds may result in catastrophic failure. SEM image analysis of the Beacon Power, LLC flywheel component [3] shows the voids and potential break-down sites for a flywheel coupon (Figure. 1-1). Transverse failures are anticipated at higher speeds, possibly originating from the voids observed in the inner and outer part of the ring. Therefore, methods to improve the 'strength' of the flywheel rim are required. Typically, fillers are added to a matrix to alter the properties.
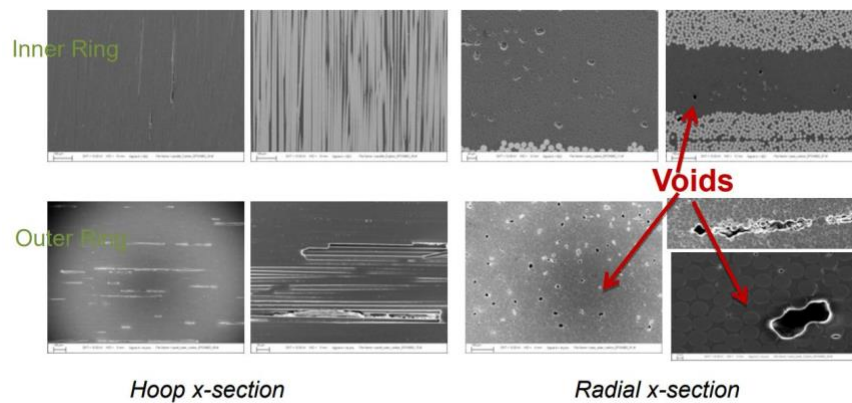
Figure 1-1: SEM image of a failed composite flywheel of the Beacon Power, LLC which shows the voids and potential break-down sites.

In this study, we proposed to implement electrospun carbon nanofibers in the region of experiencing high stresses to improve the composite matrix. Electrospun carbon nanofibers with the diameter of 200-500 nm were fabricated via thermal stabilization and carbonization of the electrospun PAN Nanofibers. Unlike other commercial carbonaceous nanofillers, such as carbon nanotubes (CNTs) and vapor grown carbon nanofibers (VGCNFs), which are in powder form, electrospun carbon nanofibers (CNFs) are practically continuous and have nearly circular cross-sections, suitable as continuous reinforcements for structural composites.

To benefit from the mechanical load bearing capability of CNFs in developing strong composites, it is essential to enhance the adhesion between the CNFs and matrix via surface modification of the CNFs as a means to facilitate load transfer between the CNF and the matrix and also to enhance the wetting of the CNFs. The surface functionalization is believed to induce surface functional groups which can form covalent bonds or dispersive interactions with a polymer matrix, leading to enhanced matrix-filler load transfer [5, 6].

To address this knowledge gap, second chapter of this report is dedicated to study the surface morphology, chemistry, and mechanical properties of individual surface functionalized CNFs. Herein, surface functionalization is perfomred in two steps including exposure of the CNFs mat to nitric acid followed by the chemical functionalization with melamine to graft amino-rich groups on the surface of the CNFs.

Exposure of the CNFs to the Nitric acid lead to formation of the functional groups such as carboxyl and hydroxyl groups on the CNFs surface which lead to formation of the covalent bonds with polymer matrix. Melamine has a conjugated structure containing both sp_2 hybridized carbon, making it suitable for both noncovalent functionalization via π-π interactions and covalent functionalization through the chemical bonding of amine group to the epoxy matrix. Herein, we

3

grafted the melamine on the surface of the CNFs to fully benefit from the amine groups in the melamine which led to enhancement in the interfacial strength of the CNFs and epoxy matrix.

As mentioned earlier the dominant failure mechanism of the flywheels is the matrix failure. Number of investigations have shown that the properties of the hybrid multiscale fiber reinforced composites, in which nanofillers are dispersed as a second phase in the matrices, can be improved substantially [7]. Various types of nanoscale materials including carbon nanotubes (CNTs), vapor grown carbon nanofibers (VGCNFs), organoclays, and silica nanoparticles have been studied to prepare resin dispersed with nanofillers to reinforce the resin-rich interlaminar region [8-11]. Specific to the CNFs, the ability to control the microstructure and morphology by tuning the carbonization parameters makes them an interesting candidate for enhancement of fracture toughness. In addition, recent studies suggest that electrospun CNFs can be developed in the form of nano-springs, which can be used to enhance fracture toughness in a composite by means of mechanical interlocking [12]. Despite all the promises that CNFs hold for improving fracutre properties of composites, very limited works have evaluated the functionality of the electropsun CNFs in reinforcing the interlaminar region of the laminated composite. Among the few studies on this subject, Chen et al. [13] reported an increase of about ~86% in interlmainar shear strength of the of carbon fiber/epoxy compsite by use of the electrospun carbon nanofibers mat. The same group also evaluated [14] the role of the well-dispersed electrospun carbon nanofibers in the epoxy resin in reinforcing the hybrid multi-scale composites. Their results pointed to an increase in the mechanical properties of the composites inlcuding impact absorpotion energy and flexural tensile strength of the composite to about 18% and 23% by incorporating a small quantity of carbon nanofibers of about 0.3 wt. % in the epoxy resin.

To address this knowledge gap, the third chapter of this report is dedicated to study the mechanics of CNFs/epoxy coupons containing electrospun functionalized CNFs and hybrid multiscale carbon fiber-carbon nanofiber composites. Mode I interlaminar fracture behavior of woven carbon fiber-epoxy laminates that reinforced with CNFs are well-studied. The CNFs have been introduced into the composite in two forms: (1) as mats of the electrospun carbon nanofibers, and (2) thin film of B-staged electrospun carbon nanofiber/epoxy in the intelaminar region.

Finally, in the last chapter of this report we have presented the recent trends in developing composite flywheels in which fiber choice, architecture and volume fraction are designed to achieve enhanced energy density. First, we presented a comparison between various types of energy storage systems, mainly the electrochemical devices such as lithium ion batteries and FESS. This comparison will highlight the benefits of FESS in terms of reliability, safe temperature range of operation, energy and power density. Next, many manufacturable designs are presented and discussed in some details. Finally, we have presented our approach toward fabricating the hybrid multiscale flywheel, in which the nanofibers were placed in the region of experiencing high radial stress. Our results pointed to an increase of at most ~14% in the energy density of the flywheel.

1.1. Goal and objectives

Materials Scientists predicted that composites fabricated with nanoscale reinforcing agents such as nanotubes, nanofibers, and platelets will have an exceptional mechanical properties. However, nanocomposites fabricated so far are only limited to few volume fraction of nano-reinforcement fillers and the results obtained so far are not comparable to advanced composites fabricated with high-performance continuous microfibers. The reasons include inadequate dispersion, poor alignment, and weak bonding of the nanofillers in the epoxy matrix.

5

The ultimate goal of this research work is to unravel the mechanics of hybrid composite flywheels with carbon microfibers and carbon nanofibers reinforcements under centrifugal forces, and evaluate the role of nanoscale fillers in delaying failure caused by centrifugal forces and enhance gravimetric energy storage. This goal perfectly facilitate to fabricate the high-performance composite flywheel with longer durability and higher efficiency. To achieve this goal, we have identified three main objectives. The schematic summary of the goal and three different objectives are shown in the Figure 1-2.

Objective 1: study the trade-off between surface functionalization of CNFs as a means to enhance CNF matrix load transfer and the mechanics of individual carbon nanofibers

Objective 2: study the mechanics of flat panel CNF/epoxy nanocomposite and hybrid nano/micro fiber reinforced composites as a function of dispersion, surface chemistry and mechanic of individual CNFs.

Objective 3: Study the failure mechanism of flywheel subjected to centrifugal forces as a function of nanoscale fillers content.
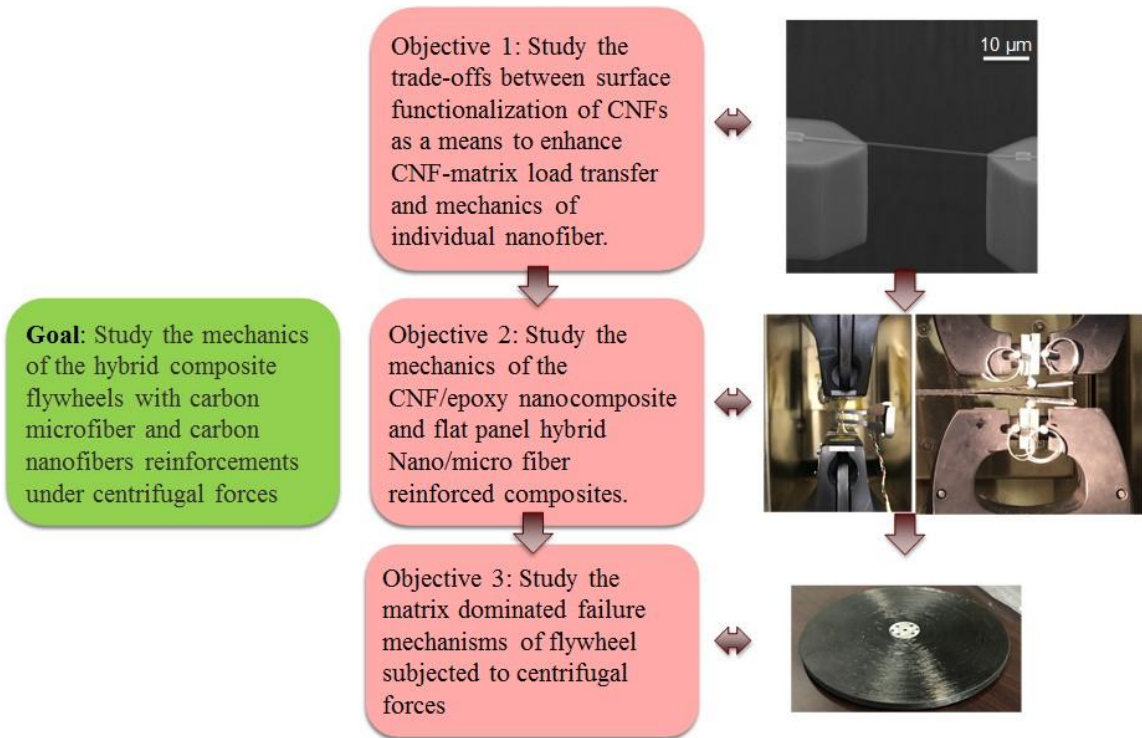
Figure 1-2: Goal of our current study followed by the three main objectives of our research work

2. STUDY THE ROLE OF SURFACE FUNCTIONALIZATION OF CNFS AS A MEANS TO ENHANCE CNF-MATRIX LOAD TRANSFER AND THE MECHANICS OF INDIVIDUAL CARBON NANOFIBER

2.1. Introduction

Carbon nanomaterials such as carbon nanotubes (CNTs), carbon nanofibers (CNFs) and graphene nanoplatelets (GNPs) maybe employed as nanofiller to other materials, such as polymers, that can enhance mechanical properties. These efforts are motivated by nanomaterial's remarkable properties, such as strength and modulus as high as 100 GPa and 1 TPa, respectively, for graphene and CNTs [15-18]. The reported relative improvements in mechanical properties are amazing. For instance, adding just 0.01 wt.% of functionalized graphene sheets to poly(methyl methacrylate) (PMMA) has led to a 33% increase in elastic modulus compared to the base polymer, far exceeding the rule of mixture predictions [19]. A more recent example has measured 14% improvement in strength by adding only 0.5 wt. % functionalized CNTs to epoxy [20].

While relative improvement in properties by adding carbon nanofillers is impressive, the carbon nanofillers content in nanocomposites is often below 2 wt. % [21, 22]. Only in rare case, higher nanofiller loadings have been studied [23, 24]. This is mainly due to agglomerated nanoparticles or poor nanofiller wettability by the matrix that adversely affects load transfer between fillers and matrix [20, 22].

An effective approach to reduce agglomeration is to functionalize the surface of the nanofiller. This approach not only enhances the filler's dispersion in the matrix during processing (often from liquid phase in a solvent, melt or pre-cured epoxy), but also increases the load transfer between the filler and matrix in the cured phase via for instance forming covalent bonds between

the filler and matrix and mechanical interlocking (caused by inducing surface undulations in nanomaterials) [20, 25-27]. However, in carbon nanomaterials, chemical functionalization changes the surface bond types, from sp2 hybridized C-C bond (graphitic bonds) to sp3 bonds to accommodate the functional groups. An unintended consequence of that is a drop in mechanical strength, as the sp3 bonds act as defects [28, 29]. For certain defects, such as vacancies in graphene, the drop-in strength can be significant, claiming more than 60% of the pristine material's strength [30]. The defects include the C atoms around vacancies or voids in the material, from where the cracks will start [28, 31].

The loss in carbon nanomaterial strength can be explained based on size effects. The high surface to volume ratio in nanomaterials increases the overall contribution that surface defects have on strength [30]. While in carbon nanomaterials, functionalization always reduces the filler's strength, in carbon microfibers, mild functionalization may not affect the strength or may even remove surface flaws and increase the strength [32, 33]. Moreover, the drop in strength with oxidation in nanomaterials with layered structures such as CNTs and GNP (and Graphene) can be even more intense. That is because the load transfer from the matrix to the filler occurs in the outmost layer (a single atomic thick layer), and chemical functionalization-induced defects will disrupt the load path within this layer. Hence, using functionalized carbon nanofillers to improve nanocomposite mechanical properties brings tradeoffs between (a) improvement in dispersion and load transfer between filler and matrix, and (b) reduction in filler properties.

A remedy for the above problem is sought in an emerging carbon nanomaterials class where the covalent bonds within the nanofiller are not limited to a plane. This category is carbon nanofibers (CNFs) that are formed by pyrolyzing polymeric precursors [34-37]. Unlike CNTs and GNPs with layered structure (with in plane covalent bonds) and weak van-der-Waals interactions

between layers, the CNF microstructure consists of a crosslinked amorphous carbon and turbostratic layer network. However, given the high surface to volume ratio, which is inherent to all nanomaterials, it is not clear whether an optimum defect density/surface functionalization exists in CNFs that can enhance nanomaterial dispersion within a matrix without considerable loss in nanofiller strength.

To address this knowledge gap, we studied the surface morphology, chemistry, and mechanical properties for individual, surface-functionalized CNFs followed by the mechanically testing CNFs epoxy coupons. The studies included characterizing individual CNFs mechanically with respect to surface functionalization and performing fracture mechanics analysis. Epoxy composite with both pristine and functionalized CNFs were fabricated and mechanically tested. Fracture mechanics estimates of critical flaw sizes were presented to further shed light on the experimentally measured values. Finally, the CNF composites mechanical properties were related to the CNFs and interface properties. The experiments at two length scales, the scale for individual CNFs and for their composites, provided valuable knowledge about the role the filler interface has on nanocomposite mechanics.

2.2. Experimental

2.2.1. Fabricating electrospun carbon nanofibers

Carbon nanofibers (CNFs) were fabricated by thermally stabilizing and carbonizing electrospun polyacrylonitrile (PAN) nanofibers. The overall approach is presented in our earlier works [36] with minor changes as presented here. PAN powder with an average molecular weight of Mw=150,000 g/mol was dissolved in N, N-dimethylformamide (DMF) and magnetically stirred for 24 hours at room temperature to obtain a 10 wt.% solution. The raw materials were obtained from Sigma-Aldrich. The continuous PAN nanofibers landed on the electrically grounded roller,

forming a nearly unidirectional fiber mat. The rotating collector's tip velocity was ~1 m/s. The electrospinning voltage was 25 kV, and the needle-to-collector distance was set to 20 cm.

PAN nanofiber mats stretched under hanging weights equivalent to ~19 MPa engineering stress as the mats heated from 100-135°C to achieve a drawing ratio of 2. This draw ratio came from previous research studies that nearly doubled CNF strength while leading to insignificant adhesion between them [8]. The hot-drawn PAN nanofibers were thermally stabilized in a convection oven by heating from room temperature to 275° C at 5 °C/min (2 hours hold time at the peak temperature), and carbonized at a 1400 °C peak temperature in a tube furnace for (1 hour hold time at the peak temperature) in an inert nitrogen atmosphere.

2.2.2. Functionalizing the CNFs surface

CNF surface functionalization occurred in concentrated HNO_3 (68 wt. %). To this end, a CNF ribbon was collected on the Teflon (PTFE) clips and immersed in nitric acid at 100°C for 15, 30, 60, and 120 minute durations. The acid treatment conditions were partly adopted from Bahl et al. [33]. Concentrated nitric acid was obtained from Sigma-Aldrich. Following this step, surface-functionalized CNFs received a distilled water rinse until they reached the pH value between 5.5–6.5; subsequently, the nanofibers were dried at 60°C for ~4 hours.

2.2.3. Mechanical and materials characterization

The pristine (as-fabricated) CNFs and surface functionalized CNFs underwent material and mechanical characterization. The CNFs diameters were measured by imaging them in SEM. At least 35 samples were tested for each fabrication condition, to obtain a statistically reliable diameter distribution. The CNFs surface chemistry was analyzed via X-ray photoelectron spectroscopy (XPS) using an Omicron XPS/UPS system with an Argus detector relying on dual Mg/Al X-ray source (Scienta Omicron GmbH, Taunusstein, Germany). Acid functionalization

effects were also studied by Fourier Transform IR (FTIR) spectroscopy. For this purpose, Thermo Nicolet 380 FTIR spectrometer with a manual infrared (IR) polarizer obtained from PIKE Technologies was employed. Individual CNFs mechanical properties were also measured via micromachined tension test devices. At least four measurements was performed for each fabrication condition. More details about the mechanical testing devices and the measurement approach is presented in our earlier work [36, 38, 39].

2.2.4. Fabricating and characterizing CNFs nanocomposite

Surface functionalization should in principle support load transfer between the CNFs and a conventional polymer matrix such as epoxies via combined dispersive and covalent bonds. To evaluate and quantify the effect surface functionalization has on the nanocomposite mechanics, CNF-epoxy nanocomposites were fabricated following the procedure described by Gardea et al. [40] with minor adjustments. This procedure is tuned to partially cure the epoxy while the CNF-epoxy is mixed, to increase the mixture viscosity and to prevent CNFs agglomeration. In this study, we used EPIKOTE™ resin 862 (Bisphenol-F epoxy resin) with EPIKURE™ curing agent W. To prepare the nanocomposites, the CNF mats were cut to 0.5 cm long pieces and then dispersed in the 20 ml of ethanol with ultrasonicator bath for 80 minutes. Immediately after, the CNFs/solvent solution with 20 ml extra ethanol was added to EPIKOTE™ resin 862 (Bisphenol-F (BPF) epoxy resin). The appropriate curing agent amount (EPIKURE™ curing agent W) was set (100:26.4 by weight) as provided by the manufacturer in two steps. The first 20% of the required curing agent was added to the solution and magnetically stirred at 500 rpm at 120℃ for 3 hours. This step increases the solution viscosity to prevent CNF agglomeration. Following this pre-curing step, the solution was cooled to about 80℃, the remaining curing agent was added, and the mixture degassed at 500 rpm for 30 minutes. Thereafter, the CNF/epoxy solution was poured into a preheated mold

12

at 120℃ with a curing cycle set to 8 h at 40 °C followed by 1 h at 121 °C and another 2.5 h at 177 °C. The first 8 hour curing at 40℃ increases the viscosity. This step reduces the thermo-mechanical viscosity drop while curing at higher temperatures, thus, the 40 °C step limits CNF agglomerate formation. At least 5 dog-bone samples for each condition following the standard ASTM D638 were fabricated and tested.

2.3. Results and discussion

2.3.1. Surface morphology of functionalized CNFs

Pristine and acid functionalized CNF mats were imaged in SEM. Figure 2-1 (a)-(c) presents SEM images showing the fibers. As shown, a 15 minute surface treatment is insignificant in changing the CNF surface morphology. However, pits and etches on the CNF surface—with an approximate dimension about 10-15 nm along the fiber—are evident after 30 minutes of acid functionalization. Given the CNFs' heterogeneous structure, composed of partially graphitic domains with various degrees of graphitization and amorphous carbon [41], selective etching in less-graphitic domains on the CNF surface can lead to pitting.

Figure 2-1(d)-(f) shows the CNF diameter distribution before and after acid treatment for 15 and 30 minutes. The fiber diameter distribution during the early stages is nearly the same. Pristine CNFs are about 103 ± 17 nm diameter, and changed to 101 ± 17 nm and 100 ± 17 nm after 15 and 30 minutes of acid treatment, respectively. Pit formation in 30-minute treated CNFs indicates surface etching. However, direct and precise diameter changes—down to a few nanometers—resulting from acid functionalization is unfeasible here because the diameter has a standard deviation (~17 nm) introduced by bending instability during electrospinning. During the early stages, i.e., the first 15 minutes, acid treatment has likely removed only the loosely bound hydrocarbons on the CNF surface; those loose hydrocarbons can be a few atomic-layers thick [32,

13

42]. This is evident in the sharper carbon skeleton peaks in the FTIR spectra after functionalization as presented in the next section.

2.3.2. Chemically characterizing CNF surface

The CNF surface chemistry, the surface functional groups formed, and their relative concentration was studied via FTIR and XPS. The FTIR spectrum for as-fabricated CNFs and acid treated CNFs with different acid treatment durations appears in Figure 2-2. In pristine and functionalized CNFs, a peak was observed at 1520 cm-1, which is assigned to the carbon skeleton [43, 44]. Acid treatment strengthens these peaks and shifts it to higher wavenumber (1575 cm-1). This finding suggests the weakly bonded hydrocarbon layer left the CNF surface during acid treatment.

There is also a peak at 1230 cm-1, corresponding to C-O bond stretching in carboxylic groups, that strengthened upon acid treatment. This peak is observed in both pristine and functionalized samples. Pristine CNFs add oxygen during stabilization and from oxygen impurities present during carbonization. Moreover, in functionalized CNFs, a peak emerges at 1742 cm-1, which is assigned to C=O stretching vibration in carbonyl and carboxyl groups. There is also a broad peak at 3100-3600 cm-1, which is assigned to –OH group in carboxyl and alcohol group [45].
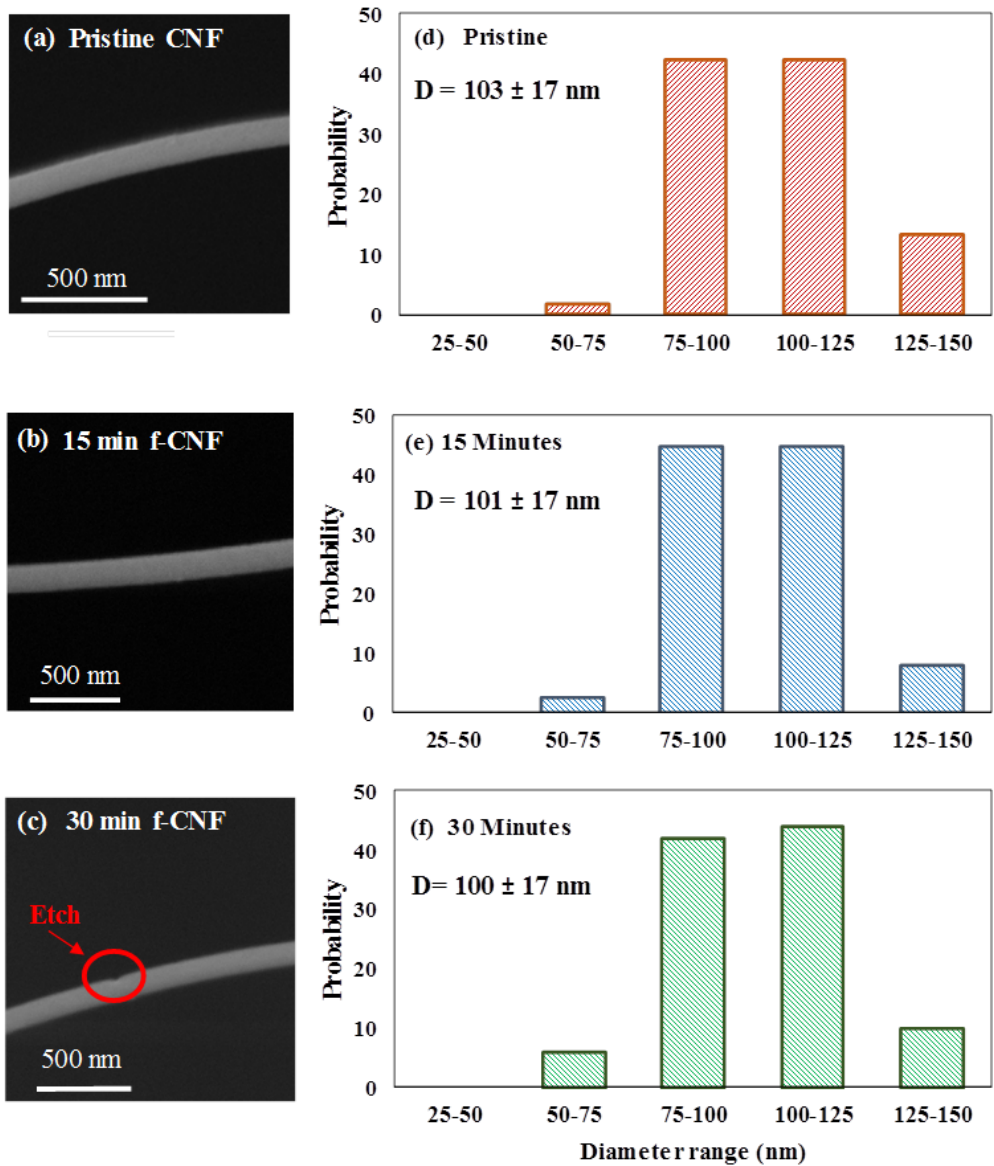
Figure 2-1: (a) –(c) SEM images showing CNF before and after 15 and 30 minutes acid functionalization. (d)-(f) the CNF diameter distribution with functionalization time.
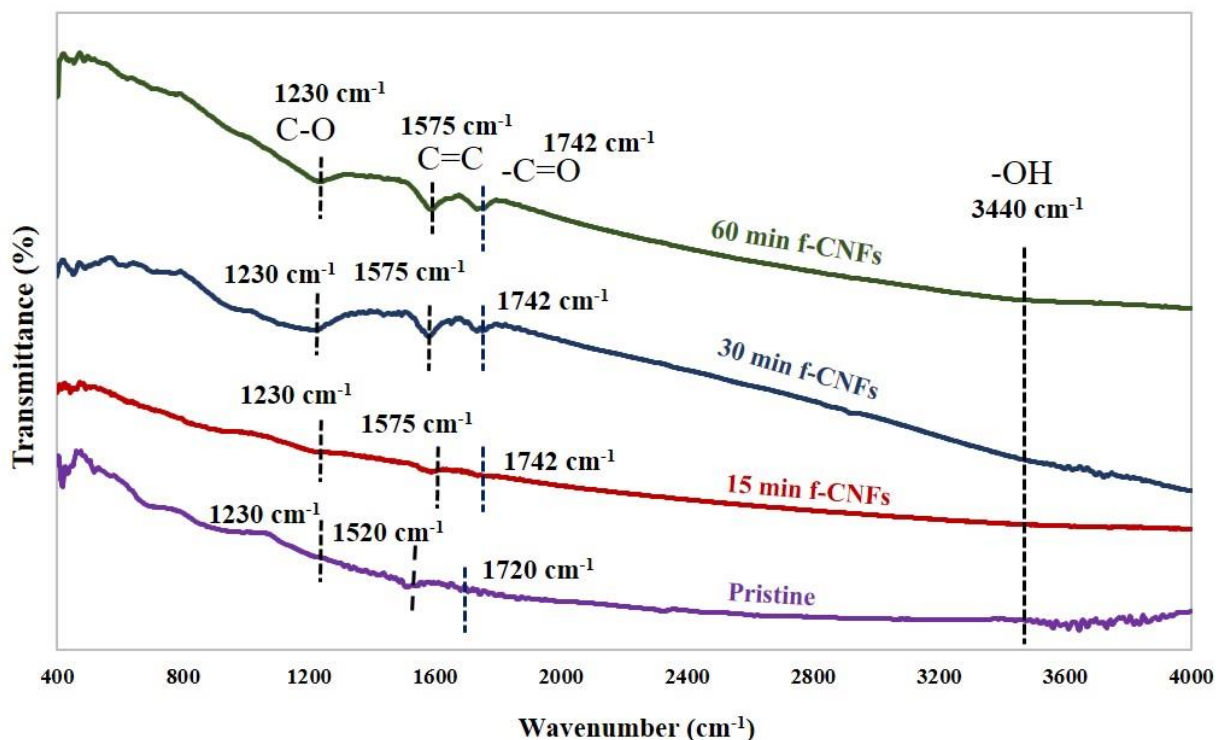
Figure 2-2: FT-IR spectra before and after CNFs receive acid treatment for 15, 30, and 60 minutes

Based on the FTIR spectrum, the acid treatment duration effectively controls functionalization intensity. After 60 minutes nitric acid treatment, the peaks associated with the oxygen moieties are much stronger than those formed in shorter acid treatment durations. The surface functional groups for pristine and functionalized CNFs were studied further via XPS. The surveys for all CNFs mainly consist of C 1s peak, at a 284.4 eV binding energy, and O 1s, at 532.6 eV binding energy. In functionalized CNFs the O 1s peak is stronger because there is surface oxidation.

High-resolution XPS spectra of C1s provided further information about the functional groups. The C1s spectrum of XPS for various treatment durations CNFs is shown in Figure 2-3 (a)-(d). The spectra have each been resolved into five individual peaks that represent graphitic

16

carbon (284.4 eV), carbon present in hydroxyl or ethers group (285.9-286.0 eV), carbonyl group (287.4-287.5 eV), carboxyl or ether group (288.5-288.7 eV), and a weak carbonate groups (290.6-290.7 eV).

According to the elemental composition taken from the XPS survey, Figure 2-3(e), the oxidative functionalization after only 15 minutes acid treatment leads to an 11% atomic oxygen to carbon ratio; this is a ~5 fold increase from 2% in pristine CNFs. However, further acid treatment for 30, 60, and 120 minutes only slightly increase the oxygen content to 13, 12, 16 %, respectively. The increase in oxygen content comes from functional groups such as hydroxyl, carboxyl, and carbonyl groups that form on CNF surfaces. The oxygen absorption rate reduces after fifteen minutes treatment by almost an order of magnitude. This is expected because, in the early treatment stage, surface oxidation may lead to oxidized graphitic domain edges on the CNF surface. As the number of un-oxidized edges available drops over time, the oxidation rate falls.

Based on the spectra shown in the Figure 2-3(a)-(d), carbonyl and carboxyl group percentages increase abruptly during the first 15 minutes during acid functionalization, followed by a moderate increase after longer acid treatments. The overall alcohol group percentages did not change substantially during acid functionalization. This data suggests that hydroxyl groups (-OH) formed on the CNF surface during acid functionalization are consumed to form -COOH and C=O groups [46], Figure 2-3(f). Hence, progressive exposure to aqueous nitric acid increasingly enriches CNFs surface with oxygen moieties, specifically carbonyl and carboxyl groups.
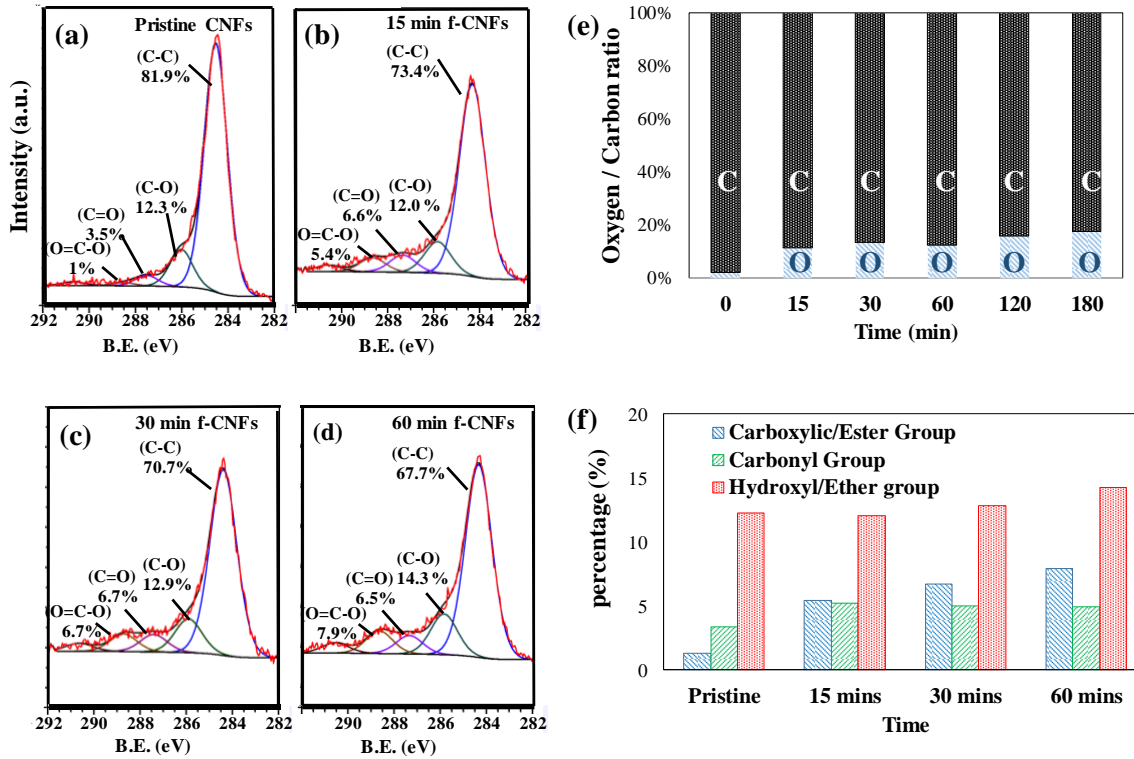
Figure 2-3. (a)-(d): CNFs carbon 1s spectra after 0, 15, 30, and 60 minutes acid functionalization, (e) relative oxygen to carbon ratio of CNFs at different acid functionalization times (f) relative contribution from each functional group in the CNF C 1s spectrum

2.3.3. Mechanical properties of the CNFs as a function of O/C contents

As discussed in the introduction, chemical functionalization may adversely affect strength in carbon nanomaterials by disrupting graphitic bonds. Unlike nanomaterials such as CNTs and GNP with layered structure, [28-30], the highly crosslinked C bond network within the CNFs' structure, obtained via pyrolyzing and crosslinking the precursor polymer chains, may make the material more resistant to flaws that are induced via chemical functionalization. This is because their crosslinked network structure will provide load transfer path around surface flaws. To evaluate this phenomenon, we studied CNF mechanical properties at three functionalization conditions: (i) as fabricated CNFs, i.e., no acid functionalization, (ii) after 15 minutes and (iii) 30

18

minutes functionalization. Single CNF nanofiber mechanical properties before and after acid treatment were characterized by using a MEMS-based nano-mechanical testing platform. More details about the testing device can be found in previous works [41, 47, 48].
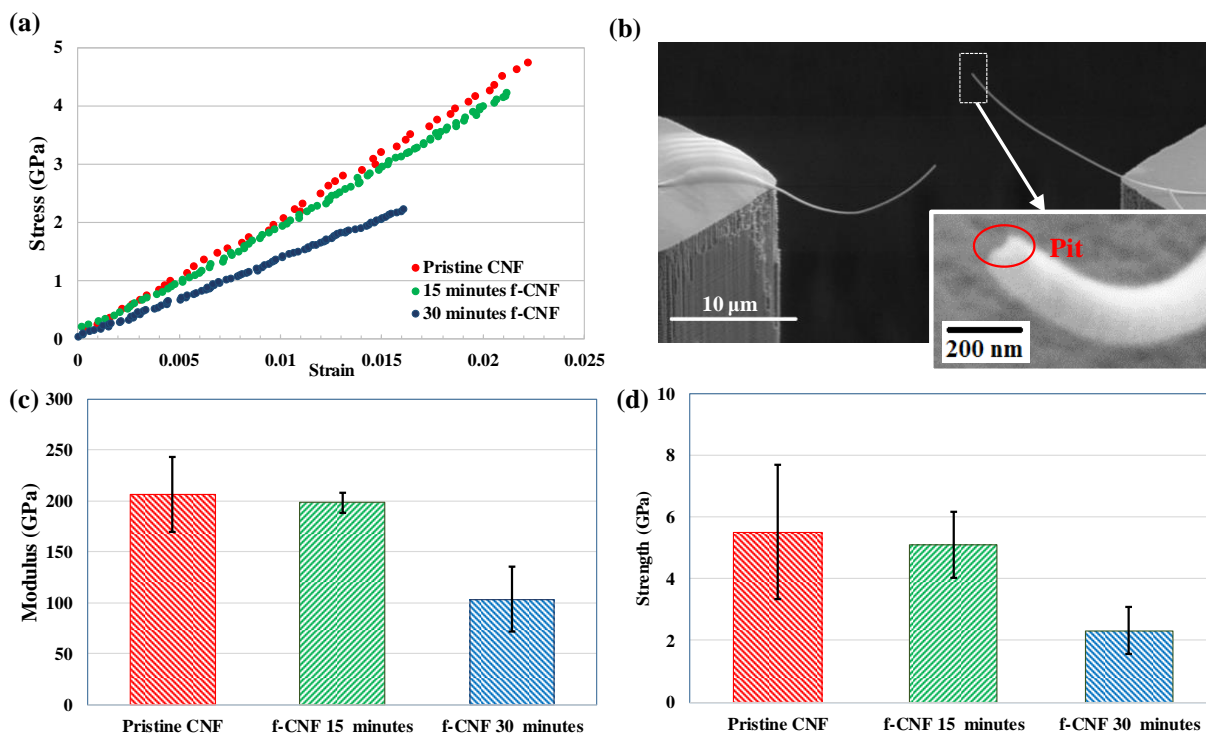
Figure 2-4. (a) Representative stress-strain curve for the pristine, 15 minutes functionalized CNF, and 30 minutes functionalized CNF, (b) 30 minutes functionalized carbon nanofiber mounted on the MEMS device after nano-mechanical testing, insert shows the fracture surface with the etch on the surface,(c) CNF tensile strength versus functionalization time, (d) CNF tensile modulus versus functionalization time.

Representative CNF stress-strain curves appear in Figure 2-4(a). As shown in the figure, in all tested cases, the CNF mechanical behavior is linear elastic up to failure. Figure 2-4(b) presents an SEM image showing a CNF tested in tension using the MEMS device. A close-up image revealing the fracture surface appears in an insert within Figure 2-4(b). The average modulus and strength values appear in Figure 2-4(c) and (d), respectively. While the average

19

tensile strength and modulus for CNFs during the 15 minutes acid functionalization are approximately unchanged—within the measurement's uncertainty—the scatter in the measured strength and modulus drops considerably (by ~50% or more). This is potentially due to surface defects—such as the loosely bound layer of hydrocarbons on the surface—getting removed during early functionalization.

However, further acid treatment for 30 minutes led to more than 50% decrease in the strength and modulus. SEM images provide insights into the cause. As shown in Figure 2-1(c) and Figure 2-4(b) insert, extended acid treatment forms pits and voids on the CNF surface. These are likely the locations along the CNFs with lower graphitization—locations that were removed selectively via acid treatment. In all 30-minute acid treated CNFs, we observed at least one pit in the gage length for every case, suggesting a linear density with more than 1 defect with a characteristic length (pit depth or length) of ~10-15 nm.

It is illustrative to compare strength loss in CNFs with the strength lost in carbon fibers after similar acid treatment. While CNFs lost ~50% after 30 minutes acid treatment at 100°C, similar treatments only reduce carbon fiber strength by ~7% [49]. This indicates the pronounced effect surface modifications have on the CNF strength compared to carbon fibers because the CNFs have much higher surface to volume ratio. In other words, a surface flaw with measuring ~10 nm, as shown in Figure 2-1(c) insert, has a more pronounced effect on a ~120 nm thick CNF than on a 5 μm thick carbon fiber. The higher specific area of carbon nanofibers means that the number of active sites per fiber unit volume where flaws can form is higher than in regular carbon fiber. Hence, CNFs are more sensitive to acid treatment compared to carbon fibers. This is attributed to the higher surface to volume ratio in nanomaterials, that means the surface defect density will be higher for the same acid treatment conditions.
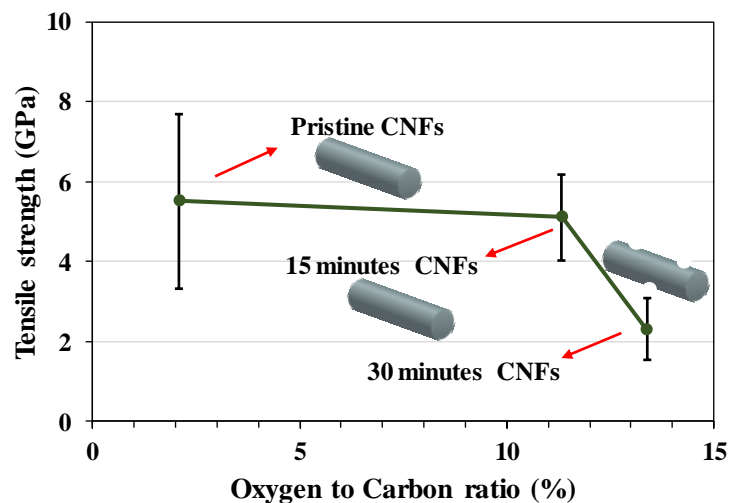
Figure 2-5. CNF tensile strength versus O/C ratio for three functionalization conditions

The changes in CNFs mechanical properties in conjunction with their surface morphology during acid functionalization appears in Figure 2-5. In this figure, the horizontal axis is the atomic ratio for oxygen to carbon, O/C, which measures oxidation progress, as obtained from XPS results in section 2.3.2. As mentioned earlier, the oxygen absorption rate in CNFs increases abruptly in the first few minutes during acid functionalization, followed by a moderate increase for the longer exposure to nitric acid. This jump comes at a negligible decrease in tensile strength, although the difference between the two cases is within the uncertainty of the measurement—a favorable condition for wettability of CNFs inside a matrix. However, further acid treatment can only marginally increase the oxygen-containing groups on the surface, while it drastically lowers strength by inducing surface defects. A fracture analysis study provides further insights into CNFs flaw resilience specially relative to other C-based nanomaterials.

2.3.4. Insight into CNF flaw-resilience from fracture mechanics

As shown in the previous section, a measurable reduction in CNF strength with functionalization is observed only when the surface flaws (e.g., the depth of the surface pits) have

grown to ~30-50 nm. In other words, there seems to exist a critical flaw size; the strength is insensitive to flaws smaller than the critical size. Following a similar argument as present in [50], this critical flaw size can be explained as follows. According to the Griffith criterion, the fracture strength of a sample σ_f with a flaw size of a can be approximated as [50]

$$\sigma_f = \alpha \sqrt{\frac{EG_c}{a}}$$ Eq. (1)

where E, G_c and α are respectively the elastic modulus and surface energy of the nanofiber and α is a proportionality constant. Ignoring the CNF surface curvature, α is close to $1/\sqrt{\pi}$. For the CNFs to be insensitive to flaws (such as pits that form on the surface), the flaw size a should be smaller than or equal to a critical flaw size $a_{critical}$ such that the fracture strength becomes equal to the theoretical strength (σ_{theory}, the material's strength without any cracks). Setting $\sigma_f = \sigma_{theory}$ and expressing surface energy with respect to the critical stress intensity factor for mode I failure as $G_c = K_{Ic}^2/E$, the critical flaw size can be estimated as

$$a_{critical} = \frac{1}{\alpha^2}\left(\frac{K_{IC}}{\sigma_{theory}}\right)^2$$ Eq. (2)

Setting $K_{IC} \approx 1\ MPa\sqrt{m}$ from [51], $\sigma_{theory} \sim 5.51 \pm 2.1\ GPa$ (from tests on unfunctionlized CNFs), and $\alpha^2 \sim 1/\pi$, the critical flaw size can be estimated as $a_{critical} \approx 16 \pm 10\ nm$. It is indeed rewarding to note that flaw sizes larger than this critical value were observed in the 30 minute functionlized samples where a major drop in strength was observed (Figure 2-1(c) and Figure 2-4(d)), while no such large surface defects and consequently negligible drop in strength was observed in the 15 minute functionalized CNFs.

It is illustrative to compare the critical flaw size in CNFs with those in other carbon nanomaterials such as graphene. In graphene, the critical stress intensity factor for mode I failure

is measured to be $K_{IC} \approx 4 - 6 \, MPa\sqrt{m}$ and strength for graphene with no cracks can reach 40 GPa [52]. Therefore, according to Eq. 2 the critical flaw size in graphene is ~3-5 nm. Comparable or even smaller critical flaw size can also be estimated for CNTs by using the reported theoretical strength and fracture toughness for CNTs [53]. Thus, it seems that the critical flaw size in CNTs and graphene is much lower than for CNFs.

In this comparison, one has to note the major differences in the microstructures. CNFs are composed of less graphitic structures. In otherwords, it seems that the remarkable strength in highly graphitic nanomaterials such as graphene comes at a cost to flaw tolerance and structural robustness. The latter should be given major consideration in nanomaterials when using them for laod bearing application. That is because failure is often progressive and starts from the weakest link. This consideration may help refocus the research on nanomaterials towards fabrication processes where defects are more controllable, such as pyrolysis [47].

2.3.5. Mechanical behavior of CNFs/epoxy composite

To evaluate the effect surface functionalization has on CNFs mechanical properties in the CNF-epoxy nanocomposites, nanocomposites with 1 wt. % pristine CNFs and 1 wt. % functionalized CNFs were fabricated and subjected to mechanical characterization. The surface functionalization was limited to 15 minutes to minimize defect formation on CNFs. To improve dispersion, the epoxy's curing profile was modified to reduce CNF mobility during, as discussed in the experimental section. The CNF dispersion in cured epoxy was evaluated under an optical microscope. The curing profile for all the samples subjected to mechanical tests includes heating for 8 h at 40 °C followed by 1 h at 121 °C and another 2.5 h at 177 °C. This curing profile led to a good CNF dispersion within the epoxy is obvious from optical images in Figure 2-6(a). A subtle but critical step in the curing cycle is the preheating for 8 h at 40 °C. This step gradually increases

the epoxy viscosity by crosslinking at a low temperature where an instantaneous drop in viscosity from thermos-physical effects is negligible. This step is significant as shown in the optical images from samples made without this step where massive CNFs agglomeration appears, Figure 2-6(b).
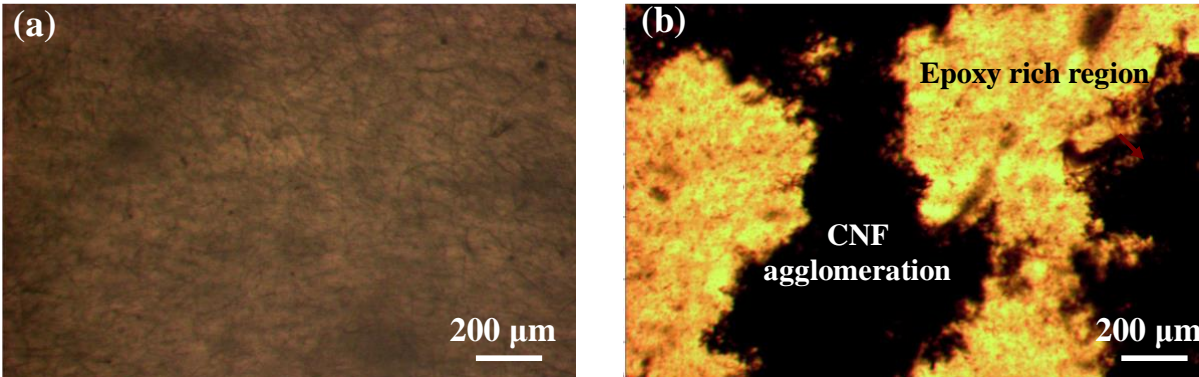
Figure 2-6. Effect that slow curing at 40 C for 8 hours provides (a) Composite containing 1 wt% functionalized CNFs with low temperature hold (b) Composite containing 1 wt% functionalized CNFs without low temperature hold shows agglomerations

Dog bone samples were tested in tension and their mechanical properties were evaluated. The mechanical characterization used only samples obtained from the modified curing cycle with good CNF dispersion evaluated from optical microscope. Example stress-strain curves for neat epoxy, and epoxy reinforced with functionalized and un-functionalized (pristine) CNFs appear in Figure 2-7(a). Figure 2-7(b), (c) and (d) show tensile strength, modulus, and energy to failure (area under the stress strain curve) for various samples, respectively.

As shown in Figure 2-7, adding 1 wt.% pristine CNFs (unfunctionalized) to the epoxy led to a considerable increase in modulus by ~31%, a moderate, ~11% strength improvement and a 15% drop in energy to failure. The increase in elastic modulus is close to the rule of mixture predictions when considering the CNF elastic modulus reported in Figure 2-4. The loss in energy to failure is merely indicates the loss in ductility from added CNFs.

Replacing pristine CNFs with functionalized CNF as filler for the epoxy matrix does not change the elastic modulus, as evident Figure 2-7(b), while it leads to enhancement in strength

(21% improvement with respect to neat matrix), Figure 2-7(c). Because the strengths in individual pristine and functionalized CNFs are nearly the same (Figure 2-5), the higher strength and energy to failure found in nanocomposites with functionalized CNFs compared to pristine CNFs should be attributed to the enhanced interfacial load transfer facilitated by surface functional groups.

The nanocomposite's fracture surface provides more evidence to support the claim that there is weaker CNF-epoxy bonding in un-functionalized CNFs. Figure 2-7 (e) and (f) show the fracture surfaces for composite specimens containing functionalized and pristine CNFs in epoxy, respectively. A clear difference between the functionalized and pristine CNFs is that composite specimen containing pristine CNFs were more prone to form agglomerates compared to pristine CNFs. The sites showing agglomerated CNFs are more numerous for the pristine CNFs/epoxy composite, an indication of weaker CNF-epoxy interaction that manifest itself in the lower tensile strength for nanocomposites with pristine CNFs.
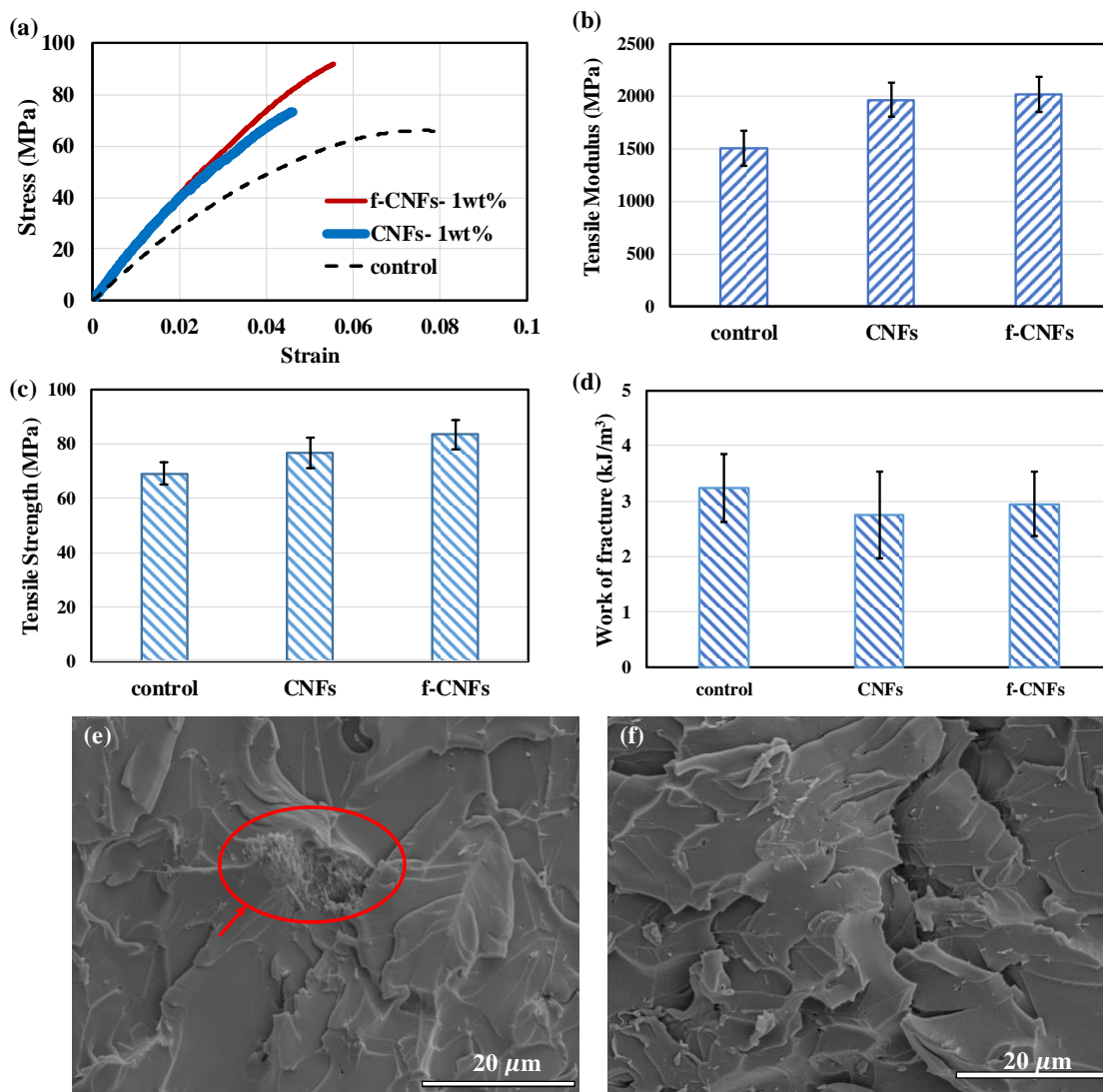
Figure 2-7.(a) Stress- strain behavior for the epoxy, 1 wt. % pristine CNFs/ epoxy composite, and 1 wt. % functionalized CNFs/ epoxy composite and (b) Elastic modulus, (c) Tensile strength, (d) Energy to failure of the 1 wt. % pristine and functionalized carbon nanofibers/ epoxy composite (e) & (f) SEM image shows the fracture surface in the composite specimen containing 1 wt% pristine and functionalized CNFs.

2.4. Conclusion

Chemical functionalization, intended to enhance carbon nanomaterial interactions with a polymer matrix, may adversely affect the strength in individual nanomaterials by disrupting their graphitic structure. In this work, we evaluated the strength loss caused by functionalization in

CNFs that are composed of a highly crosslinked network containing amorphous and graphitic carbon and compared that with the trend observed in nanomaterials with layered structures such as CNTs, as well as with carbon microfibers. Fracture strength estimations of the critical flaw size in CNFs, CNTs and graphene revealed that despite having a high surface area, carbon nanomaterials with crosslinked microstructure are resilient to flaws as big as 10-30 nm, while nanomaterials with layered structure (such as CNTs) experience a dramatic loss in strength with much lower flaw sizes (1-3 nm). Hence, it seems that remarkably high-strength graphitic nanomaterials such as graphene and CNT—with strengths that are higher than CNFs—come at a cost to flaw tolerance and robustness. In addition, when compared, CNFs and carbon fibers with similar O/C ratio revealed that the nanomaterials can be much more sensitive to acid treatment effects on strength. This is attributed to the higher surface to volume ratio for nanomaterials that results in higher surface defects (oxidized sites) per unit surface area.

In addition, a 1 wt. % carbon nanofibers epoxy composite showed an improvement in the tensile strength when the CNFs are functionalized, compared to composites with pristine CNFs, because higher interfacial bonding between the CNFs and epoxy matrix comes from grafting functional groups on the CNFs surfaces. Our current approach effectively enhanced the surface functional groups, without sacrificing mechanical properties in carbon nanofiber, and that correspondingly enhances the load-bearing capability of the CNFs along with interfacial bonding to the fiber-matrix interface.

3. STUDY THE MECHANICS FLAT COMPOSITE PANEL CNF/EPOXY NANOCOMPOSITE AND HYBRID NANO/MICRO FIBER REINFORCED COMPOSITES

3.1. Introduction

Polymer Matrix composites (PMCs) reinforced with high-performance continuous fibers such as carbon and glass fibers have been widely used for applications ranging from aerospace vehicles to medical and energy storage devices [54-58]. These fibers, with superior strength and stiffness, offer considerable structural stability and volume/mass saving in such applications. However, because their laminated structure, delamination between reinforcing plies is a primary concern for engineers and a common failure mechanism [59, 60]. Interlaminar delamination is arguably the most common advanced composite failure mode and has led to disastrous structural failures.

Many techniques have been introduced to improve the delamination resistance. Most techniques rely on through-the-thickness reinforcements to delay interlaminar delamination, for instance via three-dimensional (3D)-weaving [61], stiching [62], braiding [63], and using z-pins to adhere laminates [64-68]. However, these techniques are labor intensive and require additional manufacturing processes that increase the resulting part cost. Emerging nanotechnologies have offered new opportunities to address this problem in ways that would have been unimaginable before. The most basic nanomaterial trait is abundant free surface, owed to their characteristic material sizes. As a result, uniformly dispersed nanomaterials within a matrix can provide ample oppurtunities to resist a crack growth along the matrix-nanofiller interface via mechanisms such as crack pinning, crack deflection, crack bowing, crack front trapping and cavitation [5, 69, 70].

Different nanofillers, such as carbon nanotubes (CNT), carbon nanofibers (CNF) and polymeric nanofibers, have been introduced into the fiber-reinforced composite via various methods. Given the two filler length scales (nanofillers and carbon/glass microfibers), these composites have been referred to in the literature as hybrid or hierarchical composites. In some applications, the nanofillers were first introduced to the matrix, followed by infusing the modified matrix into the fiber tow. From a fabrication view, attempts to infuse the nanofiller suspension with vacuum assisted resin transfer molding (VARTM) was limited to very low nanofillers content, often less than 1 wt.% [71]. The rather sharp rise in matrix viscosity from adding nanofillers is a major processing barier here. Hence, the nanofiller flow within the resin in between the fibers is often ununiform, leading to nanofiller agglomeration. Variations with added processing complexities have also been introduced such as the so-called Injection and Double VARTM (IDVARTM) by Fan et al., [72] where the spacing between fibers was temporarily increased during the infusion phase to improve flow in resin with nanofillers. Despite the added processing complexity, a rather uniform dispersion with 1 wt.% of CNTs was reported. Other techniques to incorporate nanofillers without relying on the matrix flow include spraying solvent-borne nanofillers onto the fabric surface, and incorporating B-staged interleafs of nanofillers/epoxy film. Unlike the spraying method, dispering the nanofillers in a B-staged film is maintained once the nanofiller are introduced into the laminate.

The total improvement achieved in interlaminar shear strength and fracture toughness also depends on the filler type and the load transfer between the matrix and the filler. Arguably, the most widely studied nanomaterials for this purpose is CNTs, which have been directly added to the matrix or an entangled CNTs (bucky paper) network as interleaves or interlayers for the composite [73, 74]. Adding CNTs has shown to increase the Mode I and II fracture toughness to

as high as 100% and 75% respectively [75-77]. Even more dramatic improvements in composite interlaminar fracture toughness has been achieved by using polymeric nanofibers. In this regard, prioneered by Dzenis and Reneker [78], experiments have shown that electrospun polymer nanofibers in a minute quantity can improve the interlaminar fracture toughness significantly. For instance, outstanding improvement (~281%) in the carbon fiber/epoxy composite laminate's interlaminar fracture toughness was achieved by adding electrospun polysulfone (PSF) nanofibirous mats [79]. In all cases, the mechanisms that lead to the enhancement in fracture properties include crack deflection, nanofiber pull-out, plastic deformation, and crack bridging. Literature is abundant with the number of papers studying the effect of adding polymeric electrospun nanofibirous mat in improving the fracture toughness of the composite [80]. These improvements in mechanical properties are achieved with minimal weight penalty or decrease in other composite properties.

An emerging nanomaterial class that has been the focus in recent studies in hybrid/hierarchical composites is electrospun carbon nanofibers (CNFs). These nanofibers are fabricated via thermally stabilizing and carbonizing electrospun polyacrylonitrile (PAN) nanofiber precursors. The ability to control nanofiber's microstructure and morphology by tuning the carbonization parameters, as well as the aspect ratio of nanofibers (mats of continuous fibers vs. short nanofibers), makes them an interesting candidate for enhancing fracture toughness of composites [81]. In addition, recent studies suggest that electrospun CNFs can be formed into nano-springs, which can be used to enhance fracture toughness in a composite by mechanical interlocking [12]. Despite all the promisses that CNFs hold for improving composites fracture properties, limited works have evaluated the electropsun CNFs functionality in reinforcing the laminated composite's interlaminar region. Among the few studies on this subject, Chen et al. [13]

reported that interlaminar shear strength in the of carbon fiber/epoxy composite increased by ~86% in when electrospun carbon nanofiber mat was used. The same group also evaluated [14] the role that well-dispersed electrospun carbon nanofibers within the epoxy resin had in reinforcing the hybrid multi-scale composites. Their results pointed to an increase in the composite mechanical properties including impact absorpotion energy and flexural tensile strength of the composite to about 18% and 23% by incorporating a small quantity of carbon nanofibers of about 0.3 wt. % in the epoxy resin. Another study by Dhakate et al., revealed a 190% increase in the interlaminar shear strength by adding only 1.1 wt.% of partially algined CNFs as interlayers to carbon fiber reinforced composites [82].

Despite all the work on CNF reinforced composites, the effect of CNFs on interlaminar fracture behavior (Mode I) is largely unexplored. In this study, for the first time we have investigated the Mode I interlaminar fracture behavior of unidirectional carbon fiber-epoxy laminates that have been reinforced with CNFs. The CNFs have been introduced into the composite in two forms: (1) as mats of the electrospun carbon nanofibers, and (2) thin film of B-staged electrospun carbon nanofiber/epoxy in the intelaminar region. The study included innovative chemical functionalization of CNFs with melamine to better couple them with the matrix. Chemical functionalization was perfomred in two steps including exposure of the CNFs mat with nitric acid followed by functionalization with melamine to graft amine-rich groups on the surface of the CNFs. Post-mortem microscopic inspection of the fracture surfaces was performed to determine crack paths and crack morphology.

3.2. Experimental

3.2.1. Fabrication of the electrospun carbon nanofibers

The fabrication process of the electrospun carbon nanofibers (CNFs) is presented in details in an earlier work [36]. In short, Carbon nanofibers (CNFs) were fabricated via thermal stabilization and pyrolysis of electrospun polyacrylonitrile (PAN) nanofibers. PAN powder with an average molecular weight of Mw=150,000 g/mol was purchased from Sigma-Aldrich. PAN powders were dissolved in N, N-dimethylformamide (DMF), and magnetically stirred to obtain a 10 wt. % solution. The continuous and nearly unidirectional mat of PAN nanofibers were collected on the electrically grounded roller.

Subsequent to electrospinning, PAN nanofibers mat were drawn by hanging weights equivalent to ~19 MPa engineering stress while it was heated in the range of 100-135°C to achieve a drawing ratio of 2. This draw ratio was chosen based on the results from previous research studies which nearly doubled the strength of CNFs [83]. The hot-drawn PAN nanofibers were thermally stabilized in a convection oven by heating from room temperature to 275° C at a rate of 5 °C/min (2 hours hold time at the peak temperature), and carbonized at a peak temperature of 1400 °C in a tube furnace for (1 hour hold time at the peak temperature) in an inert nitrogen atmosphere.

3.2.2. Fabrication of oxidized CNFs

The CNFs were functionalized to enhance their wettability inside the matrix. To this end, CNFs were oxidized inside nitric acid. Oxidation of CNFs was carried out in concentrated HNO_3 (68 wt. %). Concentrated nitric acid was purchased from Sigma-Aldrich. A ribbon of CNFs was collected on the Teflon (PTFE) clips and immersed in nitric acid at 100°C for 15 minutes. The Oxidized CNFs were subsequently rinsed with water and dried at 60 °C for 4 hours. Acid functionalization for 15 minutes led to grafting of carboxyl groups on the surface of the CNFs

without any sacrifice in mechanical properties of the CNFs. In this paper oxidized CNFs are designated as O-CNFs.

3.2.3. Fabrication and characterization of the melamine functionalized CNFs

Melamine has a conjugated structure containing both sp_2 hybridized carbon, making it suitable for both noncovalent functionalization via π -π interactions and covalent functionalization through the chemical bonding of amine group to the epoxy matrix. Noncovalent functionalization of the CNFs, comparing to CNTs and GNPs, due to small number of the sp_2 hybridized carbon on their surface is of less importance. To fully benefit from the amine groups in the melamine and enhancing the interfacial strength between CNFs and epoxy matrix, we graft melamine on the surface of the CNFs. To this end, 10 mg/mL solution of the Melamine in DMF with addition of 0.5 mg/mL of a coupling agent Hexafluorophosphate azabenzotriazole tetramethyl uronium (HATU) in DMF solution were ultra-sonicated for 10-15 minutes. Mat of Oxidized CNFs were collected on the Teflon clips and immersed in the Melamine/ DMF solution for 4 hours. Melamine was chemically absorbed on the surface of the O-CNFs. The HATU was used as a coupling agent between Melamine and the oxygen groups on CNFs (**Figure 3-1**). Melamine functionalized CNFs were rinsed with water and dried at 60 °C for several hours. In this paper, Melamine functionalized CNFs are designated as M-CNFs. To ensure grafting of the melamine on the CNFs, XPS analysis were performed to characterize the functional groups on their surface. As mentioned earlier the morphology of the CNFs were not modified due to melamine functionalization.

33
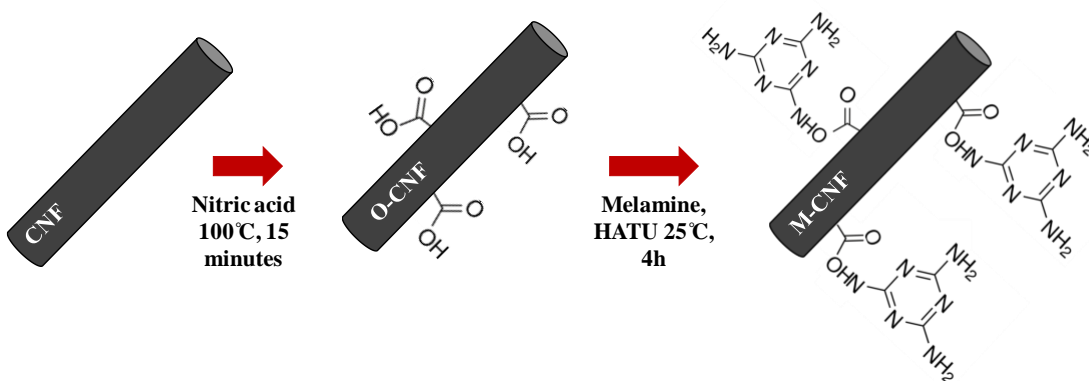
Figure 3-1. Schematic of the Melamine functionalization of the carbon nanofibers

3.2.4. Fabrication and characterization of the CNFs/epoxy nanocomposite

The Melamine functionalized CNFs (M-CNFs) should in principle facilitate load transfer between the CNFs and conventional polymer matrix such as epoxies via a combination of dispersive and covalent bonds mediated by functional amine groups on the surface of the M-CNFs. To evaluate and quantify the effect of surface functionalization of CNFs on the mechanics of matrix, CNF-epoxy nanocomposites were fabricated and tested following the procedure described in our earlier works with minor adjustments [40].

In this study, we used EPIKOTE™ resin 862 (Bisphenol-F epoxy resin) with EPIKURE™ curing agent W as the matrix. To prepare the nanocomposites, the CNF mats were cut to 1-2 mm long pieces and then dispersed in DMF ultrasonically for 3 hours, maintaining the concentration of 2 mg/mL. The choice of DMF as solvent was due to high zeta potential (~ -40 mv) of the CNFs particles in the DMF solvent, indicating good dispersion. The resulting CNFs dispersion was then filtered and washed with acetone multiple times. The filter cake was then dispersed again in acetone ultrasonically for two more hours, maintaining the concentration of 10 mg/mL. During this procedure, the CNFs become randomly oriented in three dimensions.

The CNFs/acetone solution was added to EPIKOTETM resin 862 (Bisphenol-F epoxy resin). The appropriate amount of curing agent (EPIKURETM curing agent W) was set (100:26.4 by weight) as provided by the manufacturer. About 20% of the required mass of the curing agent was added to the solution and magnetically stirred at 700 rpm at 120 ℃ for 3 hours. This step increases the viscosity of the solution to prevent CNFs agglomeration (B-staged). Following this pre-curing step, the solution was cooled to about 80 ℃, and the remaining amount of the curing agent was added and degassed at 500 rpm for 30 minutes. Thereafter, the CNFs/epoxy solution was poured into a preheated mold at 120 ℃ with a curing cycle set to 8 h at 40 °C followed by 1 h at 121 °C and another 2.5 h at 177 °C. The first 8 hour curing at 40 ℃ increases the viscosity of the solution. This step will reduce the thermo-mechanical drop in viscosity during the curing at higher temperatures, thus, it limits the formation of CNF agglomerates. To evaluate the mechanical properties of the nanocomposites, a minimum of 5 dog bone samples for each condition following the standard ASTM D638 has been fabricated and tested in tension to failure. The gage length of the dog bone samples was 1.5 cm, and they were stretched at a nominal strain rate of 0.1 % per minute.

3.2.5. Fabrication of the hybrid flat panel composite

The laminates were fabricated using the heated vacuum-assisted resin transfer molding process, wherein a glass plate mold is heated by temperature-controlled heating pad placed underneath. Unidirectional carbon fiber fabric made from T700S fiber (Toray, Inc.) was obtained from a 3rd party vendor (Composite Envisions, USA). The fabric is a no-crimp one, 609.6 mm wide and 5.3 mm thick which is continuous along the fiber direction. The weft fiber is a polyester thread that holds 12K carbon fiber tows together in a bundle--that is, without disrupting, crimping, or piercing the tow structure. The polyester thread is in a basket weave (over one/under one) placed

at every 5 mm. Each DCB laminate contained 8 plies unidirectional carbon fiber fabric with measuring 30.5 cm × 30.5 cm stacked to obtain 3 mm thick panels.

To perform the mode I fracture tests, Teflon films with a thickness of 25 micron was placed in the mid-plane of the laminate covering the half of the midplane to generate the precrack. Specimen dimensions and test parameters were according to ASTM D5528, and the samples were cut via waterjet from the panel. The DCB Mode I fracture specimens were 170 mm long and 25.4 mm wide. Hinged loading tabs (cut from aluminum piano hinge) were bonded to the outer faces of the specimens at the pre-cracked end using the Wests System epoxy (105 epoxy resin/ 205 fast hardener). The crack tip advancement was videotaped. In this way, the crack length prior to each instance of crack growth could be measured optically. To this end, the video and data acquisition were synchronized.

Three different types of specimens were fabricated. The first set of the specimen is the control sample without any modification (i.e., no CNFs) to the inter-laminar region. In the second set, melamine functionalized carbon nanofibers (M-CNFs) dried mat were placed with tweezer in the mid-plane ahead of the crack tip, maintaining the alignment of the microfibers with the nanofibers in the mat. The mass of the M-CNF was ~2-3 mg per DCB sample, and it covered a length of ~ 5 cm ahead of the crack tip. In the third set, B-staged M-CNFs/epoxy solution was prepared following the procedure mentioned in the previous section (2 wt.%), and then poured in the crack frontline and hot-pressed under 453.6 Kg (1000 lbs) for 8 hours at 40 °C. Subsequently, the neat resin infusion was carried out via the VARTM method to fabricate the composite laminates, and the composite was cured as explained in section 3.2.4.

To avoid confusion, we refer to the two approaches as hybrid composites with M-CNF interleave and interlayer, respectively.

3.3. Results and discussion

3.3.1. Surface characterization of the CNFs

The surface chemistry and formation of the functional groups on the surface of the CNFs were studied via XPS. High-resolution XPS spectra of C1s provided detailed information about the nature of the functional groups on the surface of CNFs. The survey spectrum of the as-fabricated CNFs, CNFs after acid treatment and after treatment with Melamine is presented respectively in Figure 3-2(a), 3-2(c) and 3-2(e), mainly consisting of C 1s peak, at a binding energy of 284.6 eV, O 1s at a binding energy of 532.6 eV and N 1s at a binding energy of 399 eV. In the oxidized CNFs compared to as-fabricated CNFs, the O 1s peak is considerably stronger due to the surface oxidation (compare parts (a) and (b)). After melamine treatment, strong peak of N1s also appears which represent grafting of the melamine on the surface of CNFs, Figure 3-2(e).

The C1s spectrum of XPS at different stages of the functionalization of CNFs is shown in Figure 3-3 (b), 3-3(d), and 3-3(f). The C 1s spectra have been resolved into five individual component peaks [84, 85] that represent graphitic carbon (284.4 eV), carbon present in hydroxyl or ethers group (285.9-286.0 eV), carbonyl group (287.4-287.5 eV), carboxyl or ether group (288.9 eV), and carbonate groups (290.6-290.7 eV). In the Melamine functionalized CNFs new peak also appears around 288.0 eV which confirms the presence of amide group (CO-NH). This is a direct evidence of the formation of the chemical bonding between melamine and carboxylic group on the surface oxidized CNFs.
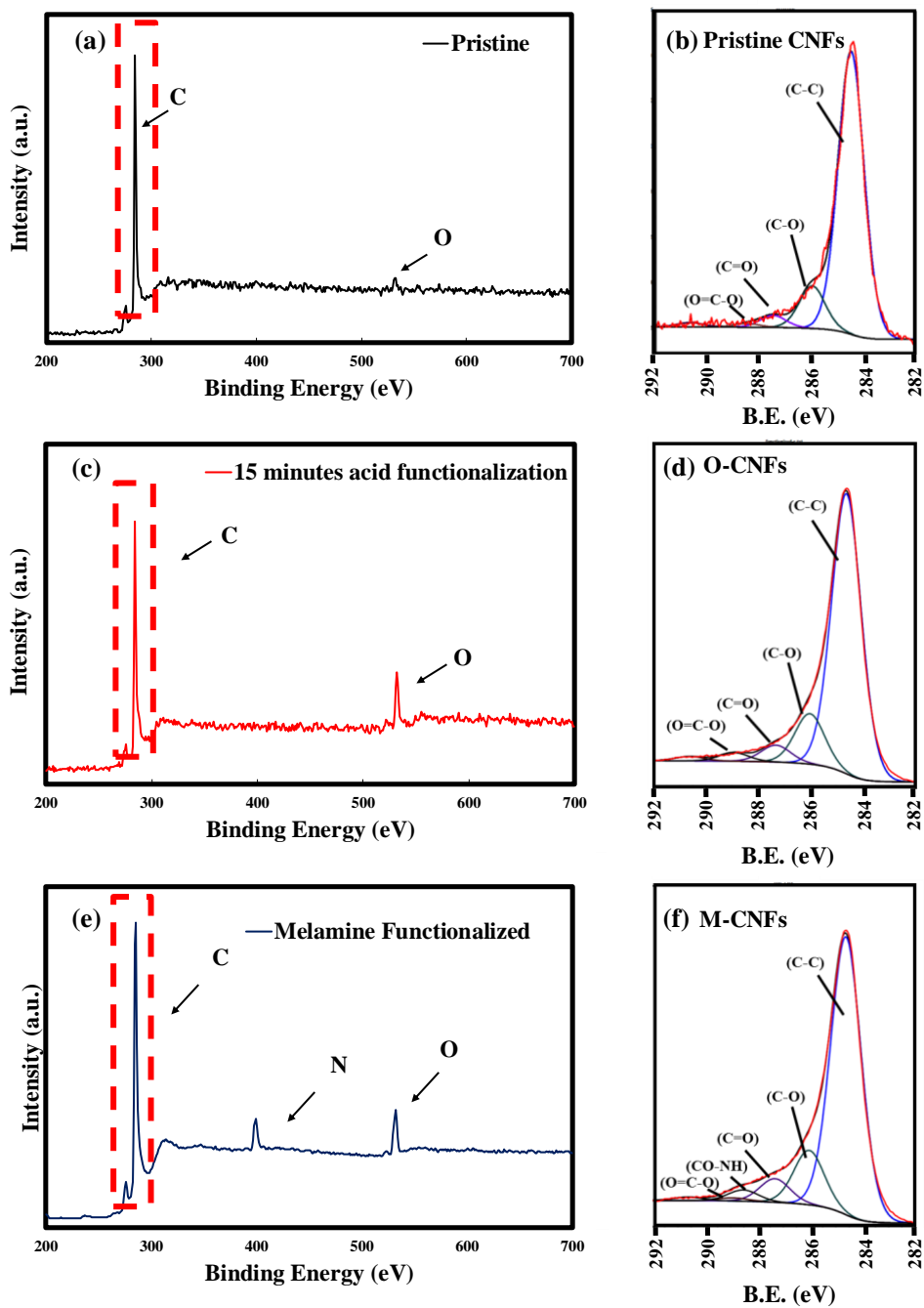
Figure 3-2. (a) XPS survey of the pristine CNFs, (b) C 1s peak of the pristine CNFs, (c) XPS survey of the oxidized CNFs, (d) C 1s peak of the oxidized CNFs, (e) XPS survey of the melamine functionalized CNFs, (f) C 1s peak of the melamine functionalized CNFs

3.3.2. Mechanical properties of the CNFs/epoxy nanocomposite

Mechanical properties of the polymer nanocomposite is greatly dependent on the dispersion of the nanofillers and interfacial bonding between the filler and matrix in the polymer matrix. The surface functionalization of the CNFs with melamine (amine groups) should in principle increase the wettability and interfacial bonding of the CNFs with the epoxy matrix via combination of the dispersive and covalent bonds. For instance, Peng et al. [86] reported an increase of 85% in the interfacial shear strength (IFSS) of the conventional carbon fiber due to introduction of poly(amido amine) (PAMAM) on the surface of the conventional carbon fibers. Zhao et al. [87] showed an increase of about 30% in IFSS of the conventional carbon fiber by grafting melamine on their surface.

In this study, in order to evaluate the role of the surface functionalization with melamine we studied the mechanical properties of the epoxy matrix which was reinforced with acid functionalized CNFs and melamine functionalized CNFs (for each case at 1 and 2 wt. %), and compared those to the neat epoxy (control sample). The results of the tension tests is presented in Figure 3-3. Representative stress-strain curves of the nanocomposites (at 2 wt. %) and the neat epoxy is shown in Figure 3-3a. The mechanical properties of the samples, modulus, strength and work of fracture, at various loadings of the CNFs were then extracted from the stress-strain curves and plotted in Figure 3-3(b)-(d). Each data point represents an average and standard deviation of a minimum of three samples tested from the same processing condition. The Work of fracture was defined as the area under the stress-strain curve.

As shown in Figure 3-3(b), the addition of 1 wt. % O-CNFs increases the average modulus of the composite from 1.5 ± 0.11 GPa for the neat epoxy to 2.02 ± 0.19 GPa. Increasing the O-CNF content to 2 wt. % further increases the average modulus to 2.14 ± 0.04 GPa. A relatively

comparable improvement in strength is also observed in O-CNF nanocomposites, Figure 3-3(c). This trend is expected, and it reflects the reinforcing effect of the O-CNFs.

The functionalization of the CNFs with melamine led to improvement in the mechanical properties of the nanocomposite compared to both the neat epoxy and the O-CNFs. For instance, the modulus of 1 wt.% and 2 wt.% nanocomposites are very close to each other (respectively, 2.63±0.29 GPa and 2.65±0.09 GPa), and they are considerably higher than the modulus of the control sample. The difference in the average elastic modulus of the M-CNF nanocomposites and the control sample is ~1.2 GPa. This improvement in modulus can be contrasted with rule of mixture predictions for the case of randomly oriented CNFs. In the case of 1 wt.% nanocomposite, knowing the density of the CNFs and the matrix (1.8 g/cm3 and 1.2 g/cm3, respectively) and the modulus of the CNFs from our earlier work of 206.8 GPa, the volume fraction of the CNF is roughly ~ 0.7 %. It should be noted that Cai et al. [88] reported the modulus of the CNFs to be around 165 GPa which is slightly different from the value reported by Kavosi et al [89]. This is due to the slightly different processing condition of the CNFs. Herein, we chose the processing condition lead to higher elastic modulus.

Rule of mixture predicts an increase in the modulus of $\Delta E \sim \eta_0 V_f E_f$, which is ~ 0.29-0.54 GPa (value of η_0 is taken to be in the range of 0.2-0.375 for the case of fibers that are randomly oriented in the 3D space or 2D planes [90]), significantly lower than the measured improvement in modulus in M-CNF nanocomposites (value of 1.2 GPa). Even in case of 2 wt. % M-CNFs, the rule of mixture predicts an improvement in modulus of ~0.58-1.1 GPa, which is still lower than the measured improvements in modulus. The under-predicted values of the modulus of the M-CNFs based on rule of mixture, especially in the case of the 1 wt.% M-CNFs, can only be explained by considering the development of an interphase region of epoxy around the M-CNFs that is

distinctly stiffer than the rest of the epoxy. The formation of this interphase region can be attributed to the strong interactions between the amine functional groups that are abundant on the surface of the CNFs and the matrix [91]. These strong interactions can enhance crosslinking and packing of the matrix chains around CNF, leading to improved stiffness. It is also interesting to note that doubling the content of the M-CNFs to 2 wt.% does not result in a noticeable change in modulus, which can be explained by considering a plateau in interphase volume that is reached around the 1 wt.%. The plateau can be reached when the neighboring interphase regions grow sufficiently large to interfere with each other. The fact that the modulus of the O-CNF nanocomposites lie in between the values of the neat matrix and the M-CNFs suggests a more compliant interphase region (likely with lower degree of crosslinking) along the interface of the O-CNFs and matrix.

It is not trivial to estimate the volume fraction of the interphase, especially considering that in all likelihood the interphase will have a gradient of properties. However, volume fraction of the interphase region can roughly be calculated using the data reported for the conventional carbon microfiber (carbon fiber) composites with epoxy resin matrix, assuming that the formation of the interphase is a surface phenomenon (as such it is the same for CNFs and carbon fibers). For instance, Gu et al. [92] reported the ratio of the ratio of interphase modulus to matrix modulus to be E_{int}/E_m~4-5. Assuming a value of E_m of 1.50 GPa (from our experiments), the modulus of the 1 wt.% M-CNFs composite (average of 2.63 GPa) can be calculated using the modified rule of mixture as $E_c = \eta_0 V_f E_f, + E_m V_m + E_{in} V_{in}$, where E_i and V_i respectively stand for the modulus and volume fraction of the three phases (fiber, matrix and interphase). Also note $V_f + V_m + V_{in} \sim 1$ (assuming zero porosity). In the case of 1 wt.% M-CNFs, $V_{CNF} \sim 07\%$. Hence, for E_{int}/E_m~4-5, and $\eta_0 V_f E_f$ of 0.29-0.54 GPa, the volume fraction of the interphase will be 10-19%. A similar calculation for the 2 wt. % M-CNFs composite suggests that even at 2 wt. % M-CNFs, the Volume

fraction of the interphase region for 2 wt. % M.CNFs is almost the same as 1 wt% M-CNFs nanocomposite, suggesting that the interphase region is almost saturated at 1 wt.%. The mechanism for the saturation of the interphase is not clear to us at the moment and further investigation needs to be performed to evaluate that.

As it can be deduced from Figure 3-3 (c), nanocomposites containing 1 wt.% and 2 wt.% melamine functionalized CNFs has ~25 % and ~30 % higher strength values compared to the control specimen, respectively. Unlike modulus, the strength of the M-CNFs and O-CNF nanocomposites are comparable. Among all the measured mechanical properties, the work of adhesion does not show a noticeable trend with adding CNFs. That is because by adding CNFs, the material becomes slightly more brittle. As a result, the effect of increased strength in enhancing the work of fracture is partly offset by the loss in ductility.
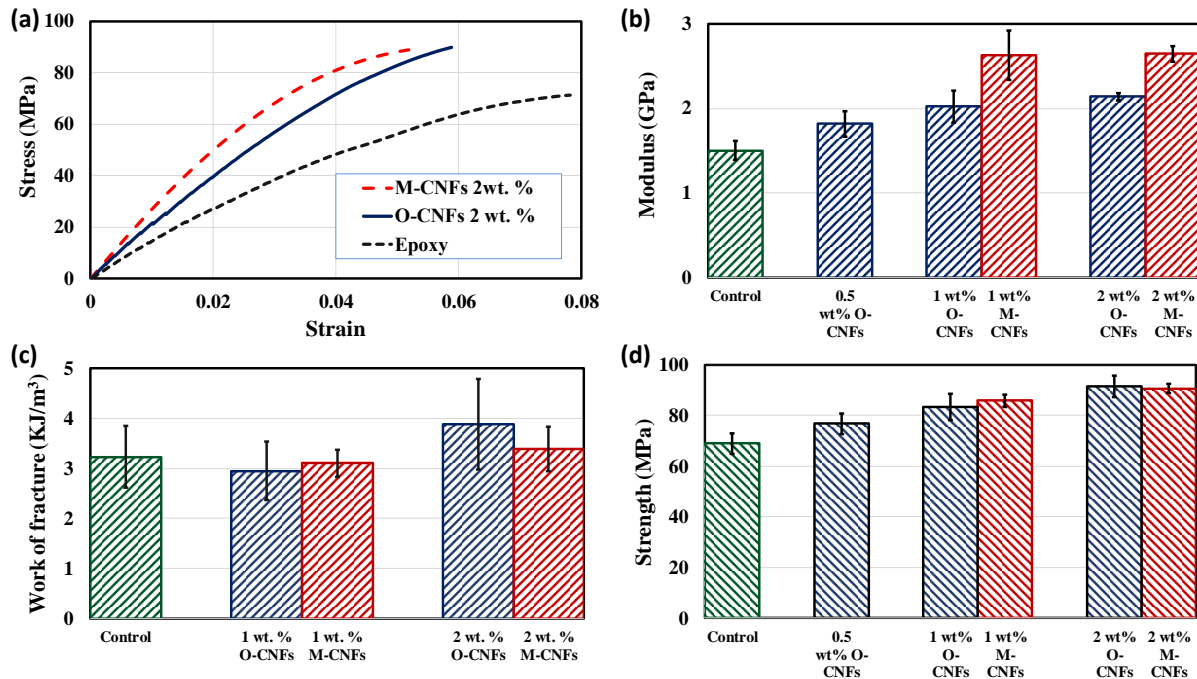
Figure 3-3. (a) typical stress- strain curve for M-CNFs/epoxy nanocomposite, (b) Modulus, (c) Strength, (d) Work of Fracture of the CNFs/epoxy nanocomposite at different mass ratio

More insight into the failure mechanisms of the nanocomposites were obtained via fractography. The fracture surface of the O-CNF and M-CNF nanocomposite were evaluated via SEM imaging. Figure 3-4 (a)-(b) are the micrographs of the fracture surface of the 1 wt.% O-CNF nanocomposite, and Figure 3-4(c)-(d) show representative fracture surfaces of the 1wt. % M-CNF nanocomposite.

A qualitative comparison between the fracture surfaces of the two nanocomposite shows a considerable difference in the number of CNF pull-out events between M-CNFs nanocomposites and O-CNFs nanocomposite. The CNF pull out events are considerably more abundant in O-CNF nanocomposites compared to M-CNF nanocomposites. This is a direct evidence in support of the stronger interfacial interactions between epoxy and M-CNFs (compared to O-CNFs). This is a results of the grafting the amino-rich groups on the surface of the carbon nanofibers, which can covalently bond with the epoxy to form strong interfaces.
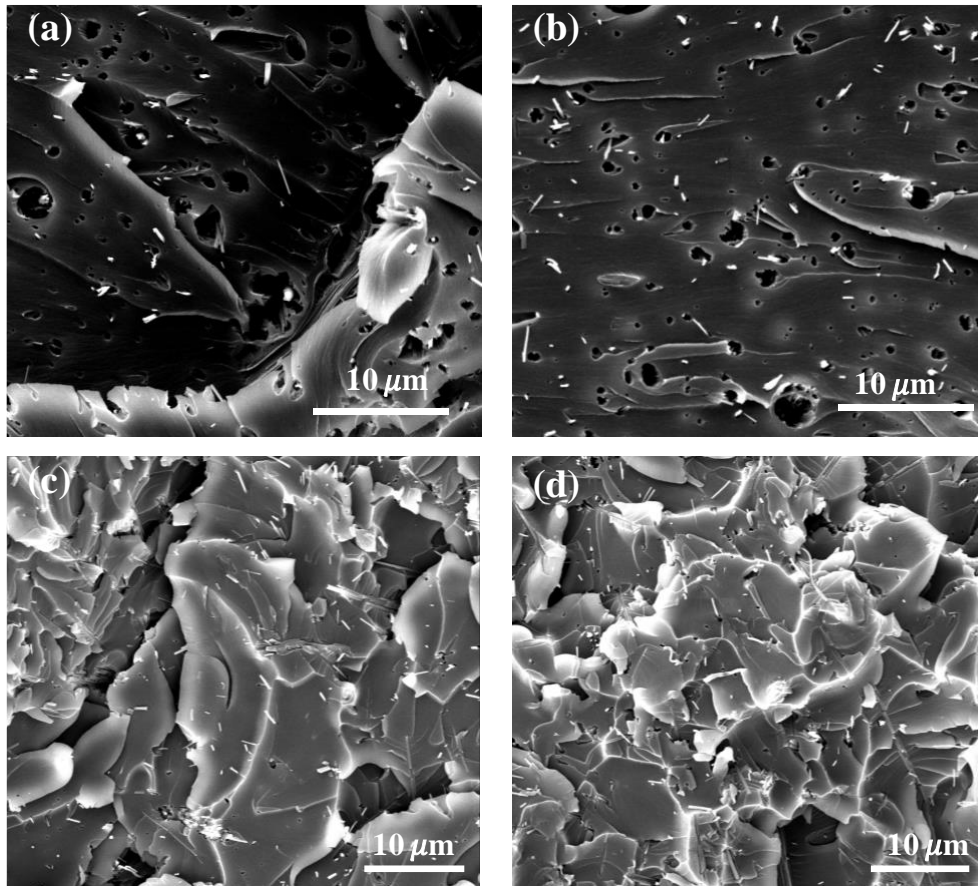
Figure 3-4. (a), (b) SEM micrograph of the fracture surface of the oxidized CNFs/epoxy nanocomposite. (c), (d) SEM micrograph of the fracture surface of the melamine functionalized CNFs/epoxy nanocomposite.

3.3.3. Fracture toughness of the hybrid composite

Interlaminar facture toughness of the hybrid carbon fiber/carbon nanofiber composites were evaluated by double cantilever beam (DCB) test following the ASTM D5528. In this section, we limited our study to CNFs that were functionalized with melamine (M-CNFs), as in M-CNFs, the amine-rich groups reacted well with the matrix, evident in the improvement in elastic modulus, presented in 3.3.2. To evaluate the effect of CNFs and their method of dispersion on fracture toughness of hybrid composites three types of specimens has been prepared and tested: (1) Control

samples with no CNFs, (2) Carbon fiber composites interleaved with M-CNFs mat, and (3) Carbon fiber composites reinforced with M-CNFs/epoxy interlayer.

The experiments and data reduction to obtain fracture toughness, G_{IC}, is in accordance with the method suggested by ASTM D5528. The load-displacement curve of each sample was collected in a displacement-controlled MTS machine. The fracture toughness corresponding to a crack length a can be determined as:

$$G_{IC} = \frac{3P_c\delta_c}{2wa}$$
<div align="right">Eq. (3)</div>

where w is the width of the specimen, and P_c and δ_c are the load and displacement at the peak load respectively. Figure 3-5(a) shows typical load-displacement (P - δ) curves for each panel type. The mechanical response for all specimens starts with an initial linear rise of the force with displacement, during this phase no crack growth is observed. This initial linear response is followed by a sudden drop in the load (i.e., drop in sample stiffness), which is concurrent with a visible crack growth. This is followed by several instances of load build-up (with no noticeable crack growth) and a subsequent, often larger and sudden decreases in load throughout and associated crack growth during the remainder of the tests. The range of crack growth studied (in most cases below 20 mm, where CNFs were placed) was sufficiently small such that the compliance of the beam corresponding to each increment of crack growth (ratio of the applied force to the displacement) scaled with the third power of the crack length, as expected from Euler Bernoulli beam theory. This saw-toothed response is commonly observed in woven composites and is characterized by a stick-slip behavior as the crack is arrested by the fiber microstructure during each load build-up, until sufficient load is applied to further propagate the crack. Toughening is achieved through fiber and nanofiber bridging behind the crack tip and was seen

throughout the specimens tested. Interlaminar fracture toughness were calculated by using the peak loads, the corresponding displacement and crack length prior to each event of crack propagation using Equation 1. The displacement and crack length were both measured using the image processing tools.

Representative examples of the load-displacement curves of the control samples and the two hybrid composites with M-CNFs are shown in Figure 3-5(b). From the peak loads, the crack initiation fracture toughness was estimated by using Equation 1 for a minimum of three samples per sample type, and the average values are plotted in Figure 3-5 (c). The error bars in the figure represent the standard deviations from a three or more measured samples per sample type. As shown in the Figure, compared to the control sample (with no M-CNFs), the average interlaminar fracture toughness ($G_{IC\text{-}Initiation}$) for crack initiation is increased about ~25% when the composite interface is reinforced with M-CNFs mats, and a more moderate increase of ~15% for the case of the carbon fiber reinforced composite reinforced with M-CNFs/epoxy B-staged interlayer is observed. The results clearly demonstrate the significant contribution of the M-CNFs in delaying crack initiation when the CNF mats are used at the interface. It is to be noted that the considerable improvement in toughness specially with M-CNF mats is achieved by adding an insignificant amount of CNFs, less than 0.11% of the total weight of the composite. The weight of the CNFs mat interleaved in the mid-layer of each DCB samples was ~2-3 mg. In comparison, the average amount of the CNFs dispersed in the M-CNF/epoxy specimen is around ~20 mg (2 wt.% of the epoxy, with good dispersion).

Given the high standard deviation of the B-staged samples, which is partly inherent to fracture toughness measurements, we also carried out the following statistical analysis. One of the well accepted metrics for evaluating improvement of a method over another, especially when

uncertainties are not negligible, is the t-test. The hypothesis evaluated for the t-test is that the CNF modified composites have an improved fracture toughness compared to the control sample. For the case of sample set 3 (B-staged M-CNFs/epoxy interlayer composite), the p-value for testing the hypothesis is 0.132 (much more than the acceptance threshold of 5%). Hence, the hypothesis cannot be accepted, and the improvement in the values of the G_{IC} in this sample relative to the control sample is not statistically significant. However, for the sample set (2) where the inter-layer region is reinforced with CNFs mat the p-value is 0.4% which is so much smaller than 0.05, and clearly shows improvement over control specimens beyond statistical uncertainties in the sample.
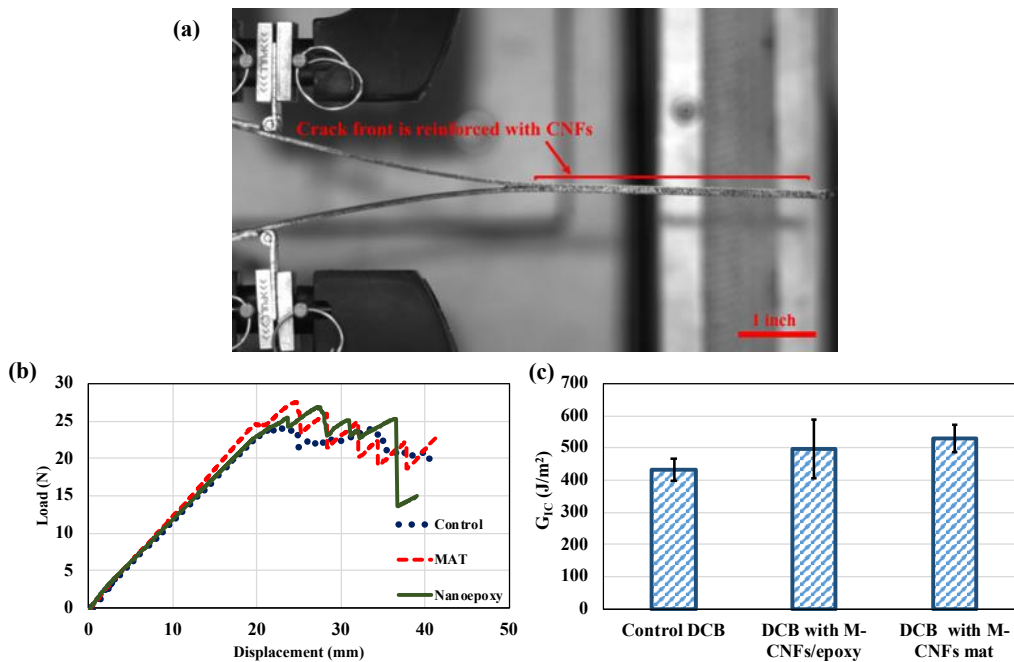
Figure 3-5. (a) DCB specimen in test (b)Typical load-displacement curve for 3 different DCB cases of:(I) Control, (II) carbon fiber composite interleaved with CNFs mat, (III) carbon fiber composite interleaved with CNFs/epoxy, (c) Fracture toughness (GIC-Initiation) for three different cases of the (I) control, (II) CNFs/epoxy in the mid-layer, (III) CNFs mat in the mid-layer

We also investigated the resistance of the hybrid composites to crack growth. To this end, at each instance of the crack growth, we calculated the mode I fracture toughness by using

Equation 1, with the corresponding displacement and crack length as input. Representative resistance curves of the three composite types ($G_{IC\text{-}Growth}$ vs. a) are shown in the Figure 3-6. Comparing the resistance curves of the control specimen to that of the composites interleaved with CNFs mat and CNFs/epoxy interleaf shows that the fracture toughness is increasing for the control specimen while the fracture toughness is decreasing for two other cases. The decrease of the fracture toughness with crack length is an indication of unstable crack growth.
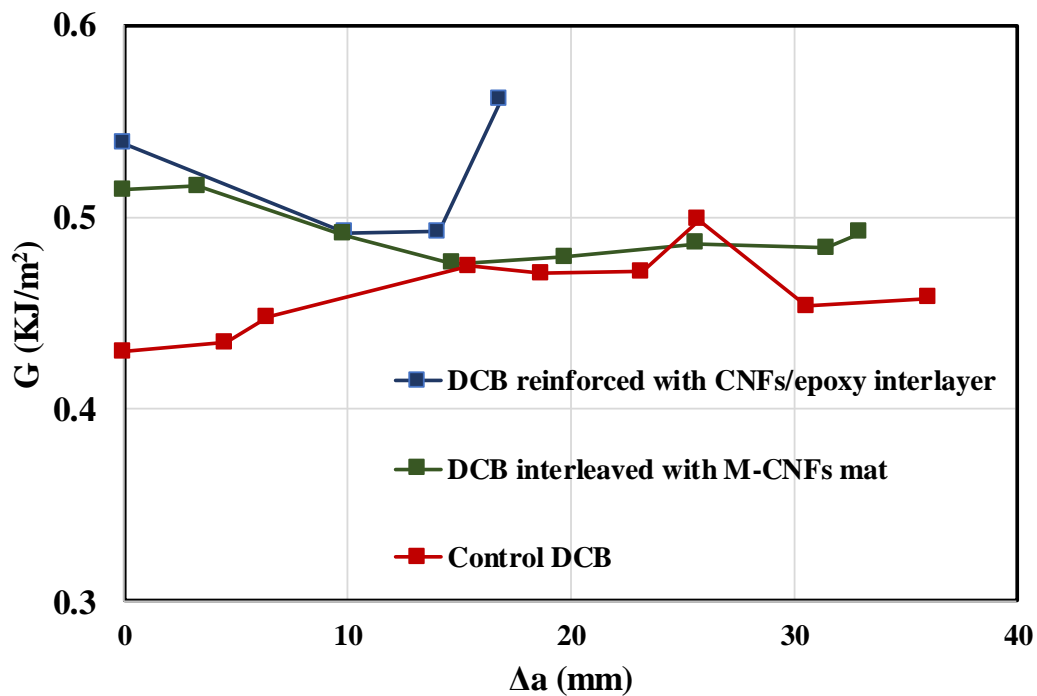
Figure 3-6. Resistance curve (G vs. Δa) for three different specimen

Figure 3-7 shows the fracture surface of the carbon fiber composite specimen reinforced with CNFs mat in the mid-layer. As shown in the SEM image, at the beginning of the test the M-CNFs bridged the crack. However, after the crack initiation, the crack will follow the least resistance path in terms of the energy required for the crack growth. The SEM images in Figure 3-7 suggests that this path includes breaking the CNF mats, such that the crack front changed its path

48

and passed through the epoxy-rich region between nanofibers mat and carbon fibers laminate. This behavior explains the drop in the $G_{IC\text{-}Growth}$ in the beginning of the test which is due to the tearing of the nanofibers mat and deflection of the crack-front to the epoxy-rich region. After this drop, the CNFs do not contribute to energy dissipation; thus, the $G_{IC\text{-}Growth}$ values became comparable to the control sample and change with the comparable rate.

A slightly different phenomenon is observed in the specimens reinforced with the CNFs/epoxy interleaf. Since the CNFs/epoxy is B-staged and has the higher viscosity, fibers beneath and above the CNFs/epoxy thin film were not wetted and this led to poor adhesion between the fibers and CNFs/epoxy thin film which led to unstable crack growth in this region, compatible with big standard deviation in the fracture toughness. Since some part of the fibers were wet by epoxy, nanofibers were able to bridge the cracks in those parts, but in parts of the composite which were not wet, crack were deflected and this led to unstable crack growth.

Considering the measured improvements in the fracture toughness (more improvement with less scatter in toughness in case of M-CNF mats whereas less M-CNFs were used compared to the M-CNF/epoxy sample) and SEM images, it becomes clear that the method of processing M-CNFs into the composite is more important than the relative mass of the M-CNFs in improving the toughness.
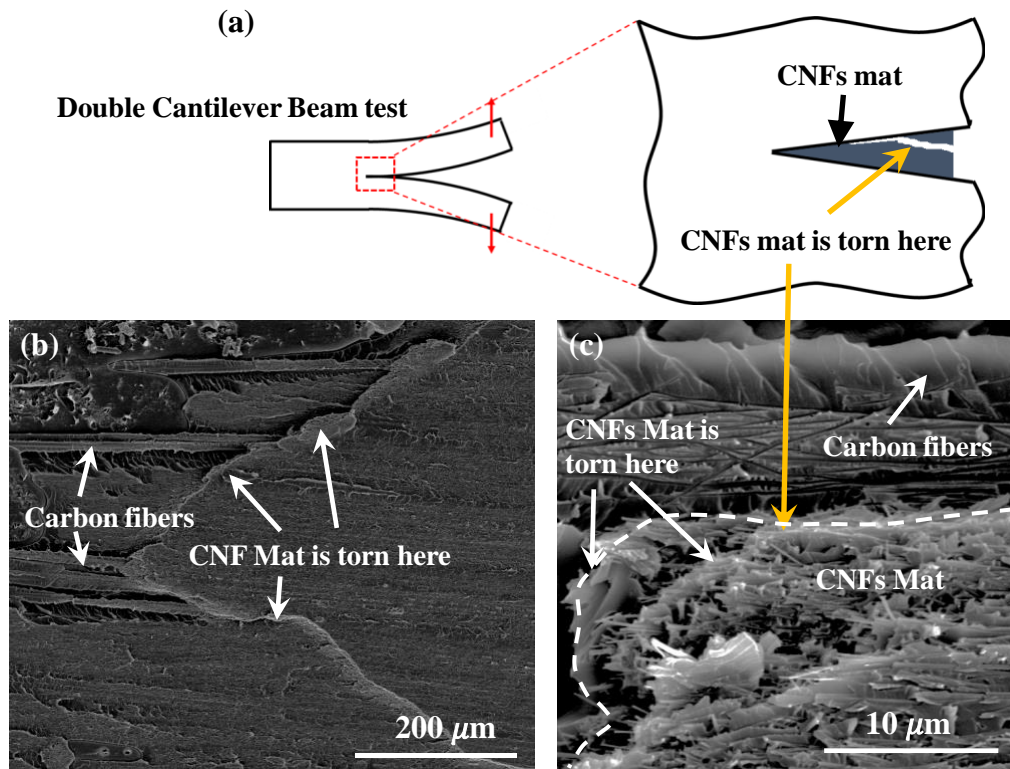
Figure 3-7. (a) schematic of fracture of specimen reinforced with CNFs mat (b), (c) fracture surface of specimen reinforced with CNFs mat at two different magnification

3.4. Conclusion

The effect of melamine functionalization on mechanical properties of CNFs/ epoxy nanocomposites and fracture toughness of hybrid composites was studied. It is showed that melamine functionalization improves the interfacial bonding between the nanofillers and the polymer matrix, and it leads to a ~76% increase in the modulus for the nanocomposite containing 2 wt.% CNFs. The observed increase in modulus exceeds the rule of mixture predictions; this indicates a higher stiffness matrix interphase region developed around the M-CNFs. Order of magnitude estimates of the volume fraction of interphase was also presented.

Moreover, we studied the effect of CNFs mat and 2 wt. % CNFs/epoxy interleaves (B-staged) on mode I fracture toughness in the unidirectional fabric carbon fiber/epoxy composite.

Melamine functionalized CNF mats showed 25% increase over the control specimen, and moderate improvement, 15%, for the B-staged CNF epoxy interleaves was observed. The improvement in mode I toughness with CNF mats was statistically significant, while in case of the B-staged samples, statistical analysis revealed insignificant improvement. This behavior can be explained by considering the fracture path in the resin-rich regions, which bypasses the CNFs especially in the case of B-staged samples due to higher viscosity of the resin of the interleaf during processing the composite. The results suggest that adding M-CNFs can effectively increase the crack initiation fracture toughness, but the crack follows an unstable growth pattern. While CNFs bridge crack growth and delay crack initiation, SEM images suggest that the crack finds a lower resistance path by tearing the CNFs or propagating along the resin-rich interface between the CNF mats and the fibers.

4. STUDY THE MATRIX DOMINATED FAILURE MECHANISMS OF FLYWHEEL SUBJECTED TO CENTRIFUGAL FORCES

4.1. Introduction

Flywheel energy storage systems (FESS) are a clean and efficient method to level supply and demand in energy grids. The energy is stored in a flywheel as kinetic energy by spinning the flywheel and released on demand; therefore, FESSs are "mechanical batteries"[1]. The FESS have been around for over 100 years and were used in early industrial systems. Similar to other energy storage systems, such as electrochemical batteries, energy density (energy stored in the battery per its unit mass) is one of the main parameters which defines the battery's performance. The achievable energy density of a FESS, such as a circumferentially wound ring or cylinder, is proportional to the material's specific strength. This proportionality favors using materials with high specific strength such as fiber composites to enhance the energy density of the flywheel.

In this report, we have presented the recent trends in developing composite flywheels in which fiber choice, architecture and volume fraction are designed to achieve enhanced energy density. First, we present a comparison between various types of energy storage systems, mainly the electrochemical devices such as lithium ion batteries and FESS. This comparison will highlight the benefits of EFSS in terms of reliability, safe temperature range of operation, energy and power density. Next, many manufacturable designs are presented and discussed in some details. While continuous fiber reinforced composites have very high strength to density ratio, especially in the direction of the fibers, they are highly anisotropic materials. As such, the performance of the composite flywheel is often limited because of tensile stresses that develop in the wheel in the direction transverse to fibers due to centrifugal forces. Additional tensile stresses may also evolve

during the curing process primarily due to anisotropic thermal expansion in individual plies. Therefore, different designs suggested to manipulate the radial stress are also presented here. Theoretically optimal designs of FESS are also presented. In theory, the optimized design of a FESS would be the rotor with continuously varying stiffness and density along the radial direction. However, manufacturing challenges associated with continuously varying the flywheel properties can make these designs highly uneconomical. Partly to accomplish the radial variation in properties and partly to induce residual compressive stresses during processing which can balance tensile stresses caused by centrifugal forces multi-ring designs have also been discussed. The multi-ring rotor is preferred from a manufacturing standpoint, and there are many options for discrete changes such as density, pre-fit stresses, materials selections, elastomeric interlayers, and fiber selection and orientation.

Lastly, potential future research directions targeting enhanced energy storage in FESS is presented. In particular, two potential future directions, the use of nanotechnology and additive manufacturing to respectively make flywheels out of materials with enhanced strength and more uniform stress distribution are presented.

4.2. Various energy storage systems compared

In our modern society, energy storage devices (ESD) benefit two main commercial power divisions: transportation and electrical power utilities [93]. Given the seasonal, weekly, daily and even hourly changes in these sector's energy demands, various ESDs can be used in these applications to level demand and supply. Flywheel energy storage systems, chemical batteries, and ultracapacitors are the main contributors to energy storage technologies. Flywheel energy storage devices have certain advantages in both sectors compared to the chemical batteries and

Supercapacitors because flywheels balance power, energy density, environmental friendliness, lifespan, temperature sensitivity, and safety, as discussed below in detail.
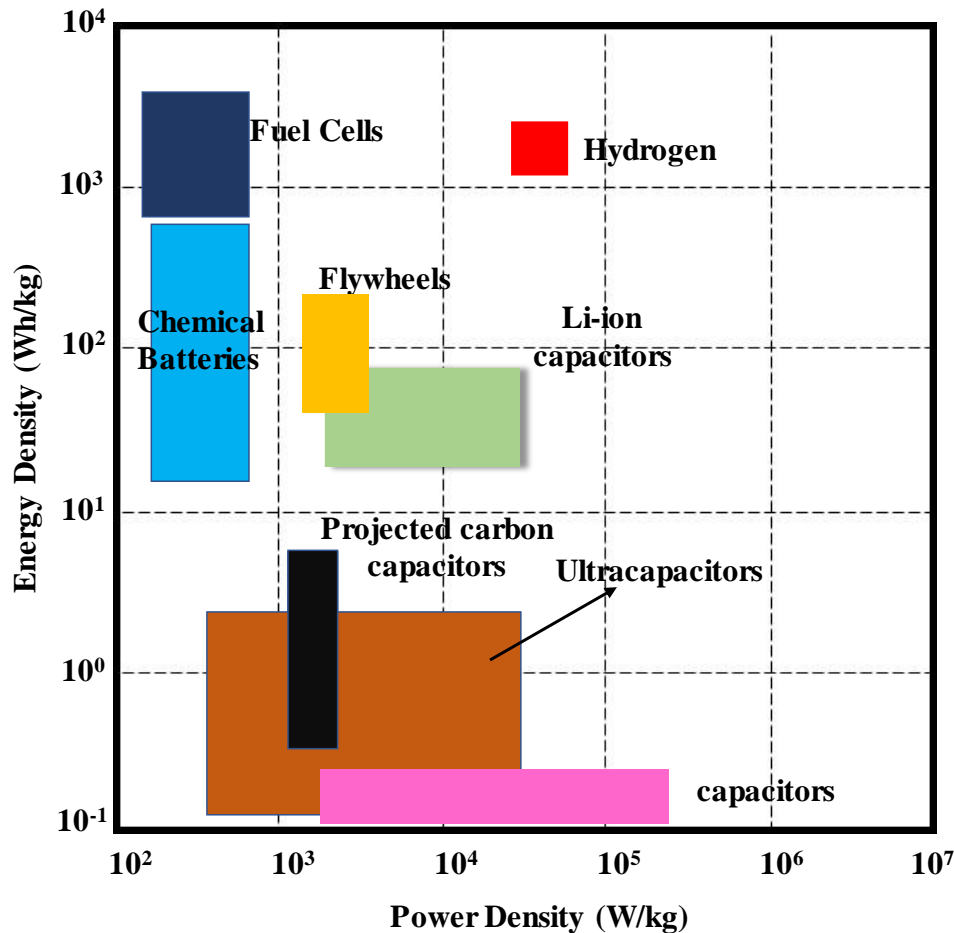
Figure 4-1. Ragone plot showing the energy density versus power density of several energy storage devices. The data is obtained from various sources in the literature including [94-98]

Two main parameters often used to evaluate the performance of an energy storage device are energy density and power density, respectively the total energy stored and the maximum power retrieved per unit mass. Some current industry technology product data provides a rough comparison of both performance metrics in a Ragone plot, Figure 4-1. An ideal EDS should appear

in the Ragone plot's top-right portion, which means an EDS can store a large amount of energy and release it quickly [95].

Electrochemical batteries, such as Li-ion batteries (LIB), are well-suited for the technologies that demand high energy density. Specific to the chemical batteries, LIBs showed the promising potential to be used on a large scale. LIBs—because they have high specific energy densities and stable cycling performance—have been widely used in various applications including the electric vehicles (EVs), portable devices, and grid energy storage [99, 100]. LIBs showed promising energy densities—as high as~250 Wh.Kg$_{-1}$—that can be further enhanced to ~650 Wh.Kg$_{-1}$ and ~950 Wh.Kg$_{-1}$ with using the Li-S and Li-air system, respectively. Nevertheless, LIBs appear on the Ragone plot's top left, presenting a tradeoff between energy storage and power. This limitation is inherent to ion diffusion [101]. In addition, electrochemical batteries become less efficient the faster they are charged and can be damaged if charged too quickly. Li-ion batteries also have cycle life limitations caused by battery aging [102].

The LIBs also suffer from fire hazards and poor low-temperature performance; both pose major challenges in battery thermal management [99, 103-106]. For instance, if LIBs operate improperly, they can release energy abruptly and that can lead to fire or explosion. The main failure mode in the LIBs system is thermal runaway, which happens when the exothermic reaction between Li and air goes out of control. Battery performance depends on operating temperature because high or low temperature affect ion transport. As the battery temperature exceeds ~80 °C, the exothermic chemical reaction rate inside the batteries increases and further heats the cell. The continuously rising temperature may result in a fire or an explosion. Also, if the battery is damaged and a short circuit results, the battery may ignite. Accidents related to the LIBs occur frequently

in cellphones, laptops, and electric vehicles. These life-threatening accidents have highlighted the safety issues to be resolved for future high-energy battery systems [107].

Ultracapacitors are also attractive energy storage technologies because they too have high power density. Ultracapacitors, also known as supercapacitors, have a structure similar to conventional capacitors but they store energy using an electrolyte solution between two high surface area electrodes [108, 109]. Electric double-layer capacitors, pseudo-capacitors, and hybrid capacitors are three supercapacitor types. High life cycles—as much as 10_5 cycles for around 40 years—and high power density are distinctive characteristics of Supercapacitors [110]. Supercapacitors are more effective at rapid and regenerative energy storage than chemical batteries. However, they also present a tradeoff between energy and power densities, and they appear on the opposite corner of the Ragone plot than LIBs because Supercapacitors provide high power but low energy density. Because the ion transport occurs in a short distance without an electrochemical reaction, these devices are highly efficient with low resistive losses. As a result, supercapacitors have significantly reduced cooling requirements. Nonetheless, there are many disadvantages with supercapacitors. The main issue with Supercapacitors is high self-discharge rate that keeps designers from using the Supercapacitor as the only energy source in vehicles [111]. Also, Supercapacitor system needs containment in case there is a dielectric breakdown that makes the supercapacitors explode. Another Supercapacitor issue: limited temperature range. The electrolyte is a liquid and at low temperatures the electrolyte solidifies. Even before solidification, ion transport is lowered by cold temperatures, and this reduction increased internal resistance in the Supercapacitors [112]. Finally, if a voltage difference is maintained for an extended time, dielectric absorption can occur, preventing the supercapacitors from fully discharging.

Unlike electrochemical energy storage devices, FESSs offer a good balance between energy density and power density. The flywheel's energy density scales with the mechanical strength required to withstand high centrifugal forces, and recent efforts put the flywheels energy density as high as ~80-100 W.h/Kg, which is similar to that of best LIBs [113]. In addition, operating systems can extract the kinetic energy stored in the flywheel controllably in times as short as seconds, with power densities similar to supercapacitors [114]. For instance, in the transportation industry, given wide environmental conditions, there is a need for high power in a compact, reliable, and lightweight package. Moreover, flywheels have operational life that can match the vehicle life. Also, unlike LIBs and supercapacitors, active temperature control might not be required for some flywheel systems; these factors significantly reduce weight, space, and cost requirements .

The FESSs are also useful in the power utility industry that needs a long lasting, low maintenance energy storage technology that is less temperature-sensitive than chemical batteries. As an example, one utility equipment provider, Beacon Power Corporation, produces commercial flywheels that Beacon claims require maintenance only once every twenty years. Given all the benefits of FESSs regarding low maintenance, low temperature sensitivity, and a good balance between energy density and power density, they are also considered as an enabling technology for many other applications including space-satellites in low earth orbits, pulse power transfer for hybrid electric vehicles, and many stationary applications [115, 116].

4.2.1. Material choice vs. geometrical design of FESS

The kinetic energy stored in the flywheel, E_k, is proportional to the second power of the flywheel angular velocity, ω, as

$$E_k = \frac{1}{2}I\omega^2 \hspace{10cm} \text{Eq. (4)}$$

where I is the moment of inertia. The faster the angular velocity of the flywheel, the higher the energy stored in it. An upper limit on the angular velocity can be determined to prevent material failure subjected to centrifugal forces (burst speed). This upper limit is often expressed in terms of energy density of the flywheel, or the energy stored in the flywheel per unit mass. The mass should be the mass of the whole energy storage system, and the energy should be the energy supplied in the device. Simply put, the energy density of the rotor at the burst speed is proportional to the specific strength of the material of the flywheel, i.e., the ratio of the material strength to density (respectively σ_u and ρ). The proportionality constant is the so-called shape factor K, which depends on the geometrical configuration and the failure criterion of the material as shown in this equation:

$$\left(\frac{E}{m}\right) = K \frac{\sigma_u}{\rho} \qquad\qquad\qquad \text{Eq. (5)}$$

The value of shape factor K often in the range of 0.3-1, as shown in Figure 4-2. While FESSs made out of steel has a long history, because the energy density is proportional to the specific strength, the choice of the advanced composite materials are more favorable. Composite materials compared to steels have higher specific strength, and flywheels made from them can store two to three times as much energy per kilogram as steel flywheels. Other attractive characteristics of the composite flywheels are their relatively uncomplicated containment. The failure of composite rotors is not as catastrophic as the metallic rotors. In most of the fiber composite flywheels, fibers are wound circumferentially, and the composite fails because the radial stress produced during the spinning. Hence, failed composite fragments often do not exert high contact pressure on their housing [117]. Despite all the benefits, composites are highly anisotropic. Specially, if orthotropic materials such as carbon, glass or aramid fibers are used with

58

poor transverse strength and modulus properties, then there should be specific consideration on the geometry design as well.

One of the earliest studies that demonstrated the applicability of composite materials with significantly large specific strength for flywheel energy storage applications was by Rabenhorst et al.[118]. DeTeresa et al. [4] examined the performance of commercial high-performance reinforcement fibers for the application in the flywheel energy storage devices. Multiple factors including inherent strength of the fibers and stress-rupture lifetime were considered. Their study showed that carbon fibers are preferred for the high performance energy storage application, owed to high specific strength of carbo fibers, and E-glass for the lowest cost.
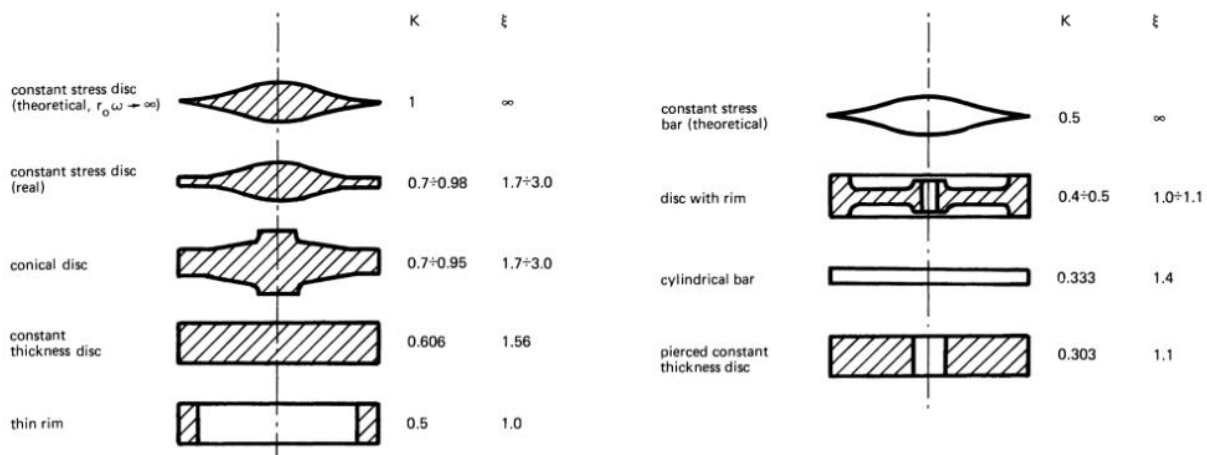
Figure 4-2. Effect of flywheel geometry on their effective shape factor.

In addition to the choice of the materials, flywheel geometry also has a major impact on the stress distribution within a flywheel for a given angular velocity and thus the energy density of the flywheel. This dependence is captured with the shape factor (Equation 2). Figure 4-2 shows the different flywheel geometries and their corresponding shape factor. Accordingly, the optimal shape that exhibits the failure at all points simultaneously and maximizes the energy density is shown in the top left corner of the figure. Other profiles are also attributed to the shape factor as

59

well [116]. Despite very promising shape factors, in case of fiber-reinforced composites, manufacturing of the structures with the shape factor exceeding 0.5 is nearly impractical and uneconomical.

In 2008, Arslan [119] investigated the effect of various shapes of the flywheel on its energy density via finite element analysis. Although the focus of the studies was mainly on steel, the results can shed light on the significance of shape in distributing stress in composite FESSs. He studied the six common geometries, a constant thickness disk, constant thickness ring, parabolic tapering, linear tapering, truncated iso-stress exponential decay tapering, and a modified iso-stress case (Figure 4-3), and ranked them according to their energy storage performance. As expected, the constant thickness profile was the worst case in terms of the energy storage and performance, while the iso-stress profile with the specific energy of the 8.977 W.h/kg showed the highest energy storage, a sheer 48.7% higher than the constant thickness disk case.
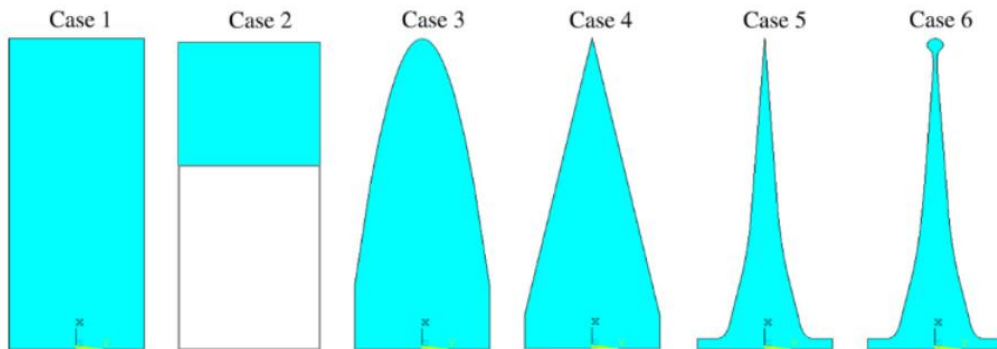
Figure 4-3. Effect of geometry on the maximum energy density of the flywheel. Case 1: a constant thickness disk, Case 2: constant thickness ring, Case 3: parabolic tapering, Case 4: linear tapering, Case 5: truncated iso-stress exponential decay tapering, and Case 6: a modified iso-stress case [Reprinted from [119]]

4.2.2. Optimal composite flywheel design for enhanced energy density

In addition to various geometries, the proper arrangement of fibers and/or inducing certain residual stress state would also result in improved performance of the flywheel. The cylindrical rotor proposed by Danfelt et al. [120] in 1977 is one example where the stress field in a multi-ring flywheel subjected to centrifugal forces was calculated through stress analysis. The authors calculate the radial and hoop stresses in a composite flywheel where soft rings was placed in between fiber reinforced stiffer rings to manipulate the stress field. The schematic of the multi-ring composite flywheel is shown in Figure 4-4. The rubber rings were places in between higher stiffness rings to lower the radial stress. Their proposed design composed of the 6 concentric rings of Kevlar/epoxy composite system of same radial thickness separated by 5 thin layers of hyper-elastic rubber rings in-between in order to reduce the radial stress distribution in the rotor. The authors considered three different scenarios. In one case, the rubber rings was placed in between composite rings, while the density and stiffness of the composite remained the same among all composite rings (benchmark). In a second and third case, they respectively and systematically varied the density and stiffness of the composite rings to manage the stress field at a given angular velocity. The stress distribution analysis of the flywheel with rubber rings and constant composite density and stiffness is shown in Figure 4-5(a). As shown in the figure, the peak radial stress in the rings varies from ~20 MPa to over 70 MPa. Following this result, Danfelt et al. attempted to find the stress field where the maximum stress in the rings at any given angular velocity are comparable to each other, so that all the rings fail around the same angular velocity.
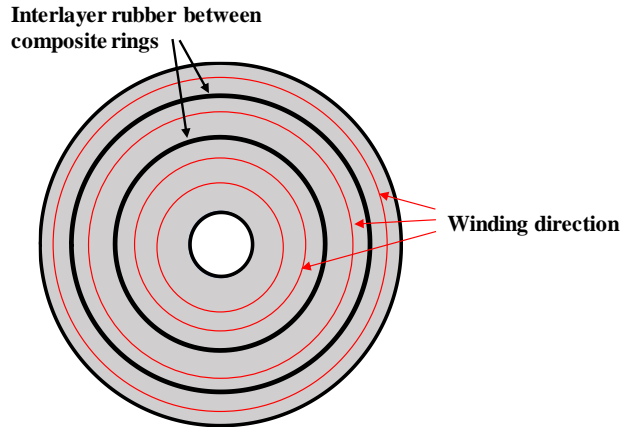
Figure 4-4. Schematic of flywheel composed of multiple concentric ring with elastomer interlayer in between.

In their initial analysis, authors decrease the density of the composite rings along the radial direction (from 0.05 lb/in3 to 0.45 lb/in3) to achieve the constant radial stress, but results showed that this could not be achieved only by changes in the density of composite rings. In some cases, this approach led to failure at lower stresses, as the maximum stress in inner rings even went above the value of the bench mark experiment. Followed by this analysis, they varied the stiffness of the inter-ring elastomer layer. The stiffness of the rings varied from very high stiffness (composite stiffness) in the inner rings to the very low stiffness at the outer ring. The obtained stress distributions showed smoother radial stress distribution compare to the first case. According to this analysis multi-ring flywheels with varying composite density and rubber rings compare to single ring flywheels are promising in terms of achievable energy storage and efficiency. However, further analysis is required to compare the data in terms of energy density.
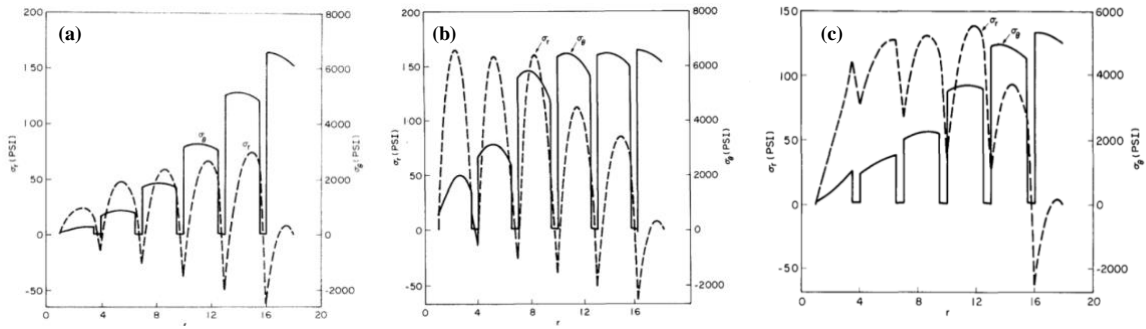
Figure 4-5. Stress distribution in the (a) flywheel composed of six composite rings separated by rubber interlayer (b) flywheel with varying density of the composite rings (from very low density in the inner ring to high density in the outer ring) (c) flywheel with varying the Young moduli of the interlayer elastomer ring (from very high stiffness of the elastomeric layer to very low stiffness of elastomeric interlayer) [Reprinted from [120]].

Among the early studies to explore the optimal design of the flywheel to maximize the specific energy, Lawrence Livermore National Laboratories (LLNL) carried out a comprehensive study under the department of energy sponsorship. In particular, LLNL sponsored a competition between industry leaders to design and develop flywheel designs for testing. The designs, shown in Figure 4-6, were selected for their performance and practicality. These designs were from Garrett AiResearch, General Electric Company, and the AVCO Corporation.

The Garrett flywheel was a wound rim of glass and Kevlar filament with a spoked hub composed of graphite/epoxy struts bonded to aluminum sheets (Figure 4-6(a)). The Garrett flywheel performed the best with the highest recorded burst energy density of 72.8 W.h/kg. The General Electric (GE) design consisted of an outer ring of filament-wound carbon/epoxy composite attached to the disk hub structure made of the cross-ply glass filaments with the maximum energy density of 68.0 W.h/kg (Figure 4-3(b)). The AVCO's "constant stress" flywheel comprised of a ring that contained a bidirectional weave of the Kevlar or glass fibers were placed in the hoop and radial directions. The goal of this weaving pattern was to produce a constant stress

profile where radial fibers would interact with the hoop fibers to transmit the outer hoop stresses to the inner hoop fibers. The AVCO design posed significant manufacturing challenges where they were only able to produce a single flywheel for testing (Figure 4-3(c)). The measure for the goodness of the flywheel was maximum energy density and stored energy in the flywheel rotor.
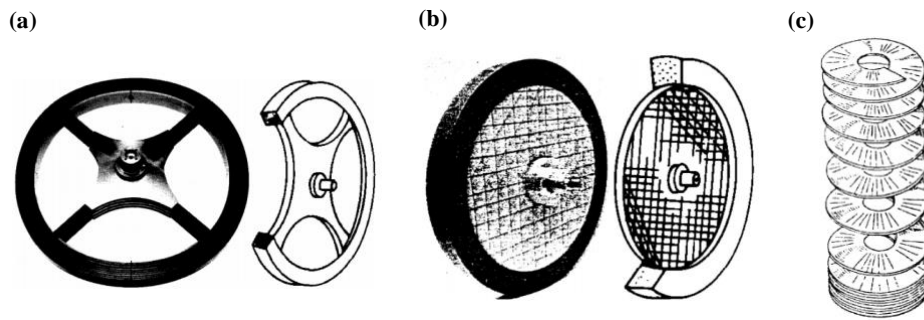
Figure 4-6. Flywheel design by (a) Garrett AiResearch (b) General Electric (c) AVCO

In 1984, Genta [121] proposed the plane stress calculation that includes the density and stiffness tuning along the radial direction of the flywheel to mitigate the radial stress produced during spinning. In order to optimize the energy stored in the flywheel, Genta assumed zero radial stress and constant radial-hoop Poisson's ratio plus constant hoop stress in the flywheel. Accordingly, this optimized design requires the hoop stiffness and density to be functions of radial distance. He suggested that the optimum design could be obtained in practice by continuously varying the fiber content as a function of radius to tune hoop stiffness. He also suggested that density of the composite along the radial direction can be tuned up by incorporating the ballasting materials such as lead particles in the polymer matrix.

In 1985, Miyata [122] proposed the optimal design for the high energy storage flywheel, using a plane stress analysis that includes the axial thickness as a parameter. Miyata's solution suggests using the hoop fiber plies of varying thickness on top of the radially arranged fibers of complementary thickness to tune up the radial and circumferential elastic moduli to more

64

uniformly distribute stress and postpone failure. His suggested model is shown in the Figure 4-7. However, this optimized flywheel is yet to be manufactured, and its fabrication is posed with major challenges related to unconventional fiber placement [123].

In 1999, Ha et al. [123] did a comprehensive study to optimize the stored energy of the flywheel that is held with the permanent magnet along the inner radius of the flywheel. This magnetic material place a compressive stress condition along the inner radius of the multi-ring rotor. In this analysis the inner and outer radius of the flywheel kept constant and the total stored energy of the flywheel is optimized. The authors varied the sequence of the composite rings along the composite rings. The five composite materials selected to be used. Glass, Aramid, and three grades of the carbon fiber as the choice for the rings. After investigating the possible permutations, the authors concluded that having materials that increase the stiffness/density ratio as the radius was increased provided the optimal sequence. This result would indicate that the more rings the flywheel contains, with the proper order, the higher the total stored energy can be.
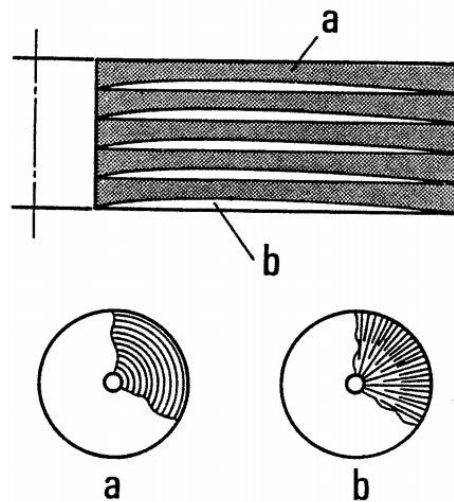
Figure 4-7. The optimized design suggested by Miyata, fibers are reinforced both in the hoop and circumferential direction

In 2012, Ha et al. [124] conducted a study to reduce the radial stress in the experiment by step-wise tuning of the stiffness and density of the fibers in the radial direction. The experimental design is in line with the guidelines presented in the analytical work of Danfelt et al. [120] that manipulated the density and stiffness of the composite to delay failure. In the flywheel in [124] the stiffness and density of the composite ring were varied by co-mingling carbon and glass fibers. The flywheel was made first as separate rings, each with a different carbon to glass fiber ratio. The inner and outer radii of the rings were designed to be press-fit inside one another, resulting in a solid FESS. The press-fitting was mainly carried out to induce compressive stresses, which will offset the tensile radial stresses that develop in the wheel at high angular velocities, during fabrication. In addition, fiber co-mingling generates the pre-stress that mitigates the radial stress build-up in the rotating flywheel. The authors studied 3 different cases, A, B, and C, of the 4-rim flywheel as depicted in Figure 4-8. There were two reinforcement materials: Carbon fiber and glass fiber, and the reinforcement volume fraction in the matrix was different in each rim. The innermost material rings of all these cases were mainly glass fibers (lower stiffness), transitioned to the mostly carbon fiber content in the outermost ring (higher stiffness). In case A, all the rims were wound simultaneously and cured by continuous filament winding. In case B, all the rims wound and cured separately and press-fitted in the flywheel. In case C, rims were wounds in two sets. Rim set 1 is composed of rim 1 and 2, and the rim set 2 is composed of the rim 3 and 4, followed by the press-fitting of the set 1 to the set 2.

The three radii in between the inner and outer radii plus the interference (the difference between the inner radius of an outer ring and the outer radius of an inner ring) for the cases that include the press-fitting were the variables of an optimization search as follows. Their stress analysis first calculated the residual stresses for the cured rings. If there was press-fitting, then the

66

rings were analyzed at each point in the press-fitting to ensure that can be removed without assistance. Once the rotor was fully assembled while surviving the stationary residual stress associated with manufacturing, then stress analysis was carried out at high angular velocities. The parameters to be optimized were the strength ratios, $R_r=\sigma_r/Y_T$ and $R_\theta=\sigma_\theta/Y_\theta$, at a given angular velocity of $\omega_{max}=$ 15 krpm. Their analysis along the experiment shows that case B with the press fit interference was the optimum design. The radial strength ratio in case B is 0.19 while the strength ratio in cases A and C reaches 0.39 and 0.75 respectively. Case A in terms of manufacturing cost and simplicity has the advantage over the case B and C.
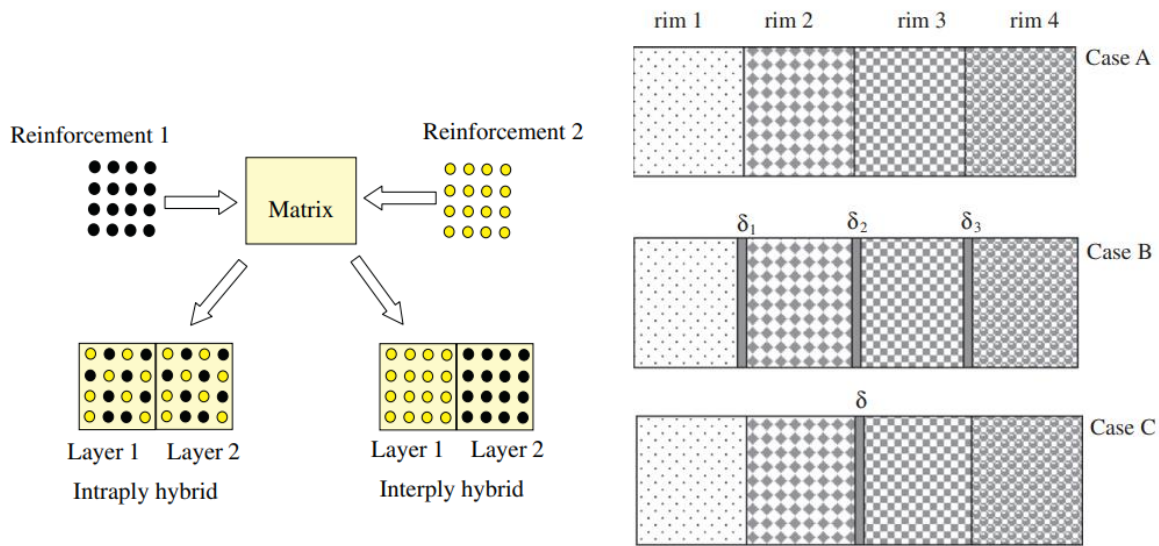
Figure 4-8. Three different cases of flywheel design [Reprinted from [124]]

Referring to the works mentioned here, there are many options for enhancing the performance of flywheels. Theoretically optimized solutions for rotors with continuously varying material or geometric properties can serve as benchmarks against new flywheel design ideas. However, manufacturing difficulties linked with continuously varying the flywheel properties can make these designs highly uneconomical. Given all of these possibilities, there is a clear need to

narrow down the research range to the most relevant analyses. Discrete variation (multi-ring rotors) is preferred from a manufacturing standpoint, but there are many options for discrete changes such as density, press-fit stresses, material selections, elastomeric interlayers, and fiber selection and orientation [113].

4.3. Stress analysis in the flywheel

One of the earliest studies to analyze the elastic stresses in the symmetrical disk was carried out by Manson [125]. His analysis was based on the finite-difference solution of the equilibrium and compatibility equations for elastic stresses in an axisymmetric disk. The advent of the composite materials pushed the researches toward new designs to mitigate the radial stress during spinning of the composite flywheel. Following by Manson, Genta [116, 121] performed extensive studies to modify the Manson's solution for orthotropic materials. The introduction of the multi-ring design to manipulate the radial stress in the flywheel attracted the number of researchers to conduct a study to further improve the energy storage capability of the flywheel. In this regard, literature is abundant with the number of studies using the multi-ring design approach attempted toward fabrication of optimized design.

This section is dedicated to the stress analysis of multi-rings flywheel, where the stress analysis of single ring flywheels is presented as an introduction. Much of the works on the single rings was carried out by Genta [116, 121], Lekhnitskii [126], and Garbys and Bakis [127], and the stress and failure formulations presented for the multiple ring rotor are based on the Arnold formulations [128, 129].

4.3.1. Single ring flywheels

Stress distribution in the axial orthotropic disk with the constant thickness, under the assumption of the axial symmetry, plane stress state and linear orthotropic behavior of the

materials can be solved following the equilibrium, displacement compatibility, and the constitutive

equation for the axially orthotropic materials using these relationships:

$$\frac{d\sigma_r}{dr} + \frac{\sigma_r - \sigma_\theta}{r} + \rho\omega^2 r^2 = 0 \text{ (Equilibrium)}$$
Eq. (6)

$$\varepsilon_r = \frac{d}{dr}(r\varepsilon_\theta) \text{ (Strain compatibility)}$$
Eq. (7)

$$\begin{bmatrix} \varepsilon_r \\ \varepsilon_\theta \end{bmatrix} = \begin{bmatrix} \frac{1}{E_T} & \frac{-\nu_L}{E_L} \\ \frac{-\nu_L}{E_L} & \frac{1}{E_T} \end{bmatrix} \begin{bmatrix} \sigma_r \\ \sigma_\theta \end{bmatrix} \text{(Constitutive equation)}$$
Eq. (8)

where the centrifugal force is included as a body force term. Equation (4), (5), and (6) are the basic

terms used in the Elasticity solution. The solution to the above set of PDEs can be obtained based

on various types of boundary conditions (BCs), and the results are typically presented in terms of

non-dimensional quantities such as $\mu = \sqrt{\frac{E_L}{E_T}}$, $\beta = \frac{r_i}{r_0}$, and $\chi = \frac{r}{r_0}$ which simplifies the stresses

equations in the flywheel. A commonly assumed set of BCs is zero radial pressure on the inner

and outer radii (traction free surfaces). The particular solution of the set of (3)-(5) PDEs becomes

$$\sigma_r = \rho\omega^2 r_0^2 \left(\frac{3+\nu}{8}\right)\left(1 + \beta^2 - \frac{\beta^2}{\chi^2} - \chi^2\right)$$
Eq. (9)

$$\sigma_c = \rho\omega^2 r_0^2 \left(\frac{3+\nu}{8}\right)\left(1 + \beta^2 + \frac{\beta^2}{\chi^2} - \frac{1+3\nu}{3+\nu}\chi^2\right)$$
Eq. (10)

Another interesting set of BCs can also be applied to describe the assembly of the rings at

zero angular velocity, where constant inner pressure, P, and outer pressure, Q, is applied (ω=0):

$$\sigma_r = \left(\frac{P-Q}{1-\beta^2}\right)\beta^2\chi^{-2} + \left(\frac{Q-P\beta^2}{1-\beta^2}\right)$$
Eq. (11)

$$\sigma_h = \left(\frac{P\beta^2-Q}{1-\beta^2}\right) + \left(\frac{Q-P\beta^2}{1-\beta^2}\right)\beta^2\chi^{-2}$$
Eq. (12)

Genta also suggested the solution for the stress distribution in the flywheel subjected to the temperature gradient. The solution to this problem dependent on the temperature profile. If the temperature profile follows the polynomial form:

$$T = \sum_{i=0}^{n} b_i \chi^i \qquad\qquad \text{Eq. (13)}$$

where the coefficients b_i have dimension of a temperature, the stress distribution in the flywheel follow the equations (14) and (15). For each term in these equations, stress distribution can be calculated separately. The stress field coming from the i_{th} term of the temperature profile is

$$\sigma_r = \frac{E b_i \alpha}{i+2} \left\{ \frac{1}{1-\beta^2} \left[1 - \beta^{2+i} - (\beta^2 - \beta^{2+i}) \frac{1}{\chi^2} \right] - \chi^i \right\} \qquad \text{Eq. (14)}$$

$$\sigma_h = \frac{E b_i \alpha}{i+2} \left\{ \frac{1}{1-\beta^2} \left[1 - \beta^{2+i} + (\beta^2 - \beta^{2+i}) \frac{1}{\chi^2} \right] - (i+1)\chi^i \right\} \qquad \text{Eq. (15)}$$

In principle, the stress field in a flywheel under the combined effect of centrifugal forces, prescribed inner and outer pressure and change in temperature can be obtained via superposition. Genta [116, 121] also further studied the more general case of the hyperbolic disc using an orthotropic material in different loading conditions, similar to the aforementioned study for the isotropic disk. For simplicity, a general solution form to the constant thickness ring is provided with this equation:

$$\sigma_c = \rho \omega^2 r_0^2 \left(\frac{3+\nu_{hr}}{9-\mu^2} \right) \left[\mu L \chi^{(\mu-1)} + \mu(L-1)\chi^{(-\mu-1)} - \chi^2 \left(\frac{\mu^2 + 3\nu_{hr}}{3+\nu_{hr}} \right) \right] + \left(\frac{P\beta^{\mu+1} - Q}{1-\beta^{2\mu}} \right) \mu \chi^{\mu-1} +$$

$$\left(\frac{P - Q\beta^{\mu-1}}{1-\beta^{2\mu}} \right) \mu \beta^{\mu+1} \chi^{-\mu-1} \qquad\qquad \text{Eq. (16)}$$

$$\sigma_r = \rho \omega^2 r_0^2 \left(\frac{3+\nu_{hr}}{9-\mu^2} \right) \left[L\chi^{(\mu-1)} - (L-1)\chi^{(-\mu-1)} - \chi^2 \right] + \left(\frac{P\beta^{\mu+1} - Q}{1-\beta^{2\mu}} \right) \chi^{\mu-1} -$$

$$\left(\frac{P - Q\beta^{\mu-1}}{1-\beta^{2\mu}} \right) \beta^{\mu+1} \chi^{-\mu-1} \qquad\qquad \text{Eq. (17)}$$

where $L = \left(\frac{\beta^{-\mu-1} - \beta^2}{\beta^{-\mu-1} - \beta^{\mu-1}} \right)$. Genta's solution, comprehensively considers different loading conditions including temperature variation on the wheel. In his analysis the temperature gradient is considered to be in the polynomial form. Other solutions have also been proposed by Arnold et al. [128] with comparable results, where the rotating disk experiencing the thermal loads (linear temperature gradient), centrifugal forces, internal and external pressure.

4.3.2. Multi-ring flywheels

Stress distribution in the flywheel composed of multiple concentric rings can be solved with the approach similar to the single ring method by employing appropriate boundary conditions, mainly the continuity of radial displacement and radial stress. Here we are referring the general idea of the Arnold et al. [128] and Ha et al. [123, 124, 130] approach and avoid going into the computational details. Arnold et al. [128, 131] takes into account the misfit between each consecutive rings as well. Radial stress continuity requires the following boundary conditions:

$$\sigma_{r_1}(r = r_1) = P_1$$

$$\sigma_{r_1}(r = r_2) = \sigma_{r_2}(r = r_2) = P_2$$

$$\sigma_{r_2}(r = r_3) = \sigma_{r_3}(r = r_3) = P_3$$

$$\vdots \qquad\qquad\qquad\qquad\qquad\qquad\qquad\qquad\qquad\qquad \text{Eq. (18)}$$

$$\sigma_{r_{n-1}}(r = r_n) = \sigma_{r_n}(r = r_n) = P_n$$

$$\sigma_{r_n}(r = r_{n+1}) = P_{n+1}$$

Where P_1 and P_{n+1} are the internal and external pressure applied to the flywheel, respectively. Also, r_1, r_2, … and r_n are the radius of the rings respectively. Similarly, same approach regarding kinematic constraint at the interface (misfit δ) can be written as

$$u_{r_2}(r = r_2) - u_{r_1}(r = r_2) = \delta_1$$

$$u_{r_3}(r = r_3) - u_{r_2}(r = r_3) = \delta_2$$

$$u_{r_4}(r = r_4) - u_{r_3}(r = r_2) = \delta_3 \qquad \text{Eq. (19)}$$

$$\vdots$$

$$u_{r_n}(r = r_n) - u_{r_{n-1}}(r = r_n) = \delta_{n-1}$$

where δ_1, δ_2, δ_3,... are the misfits between the consecutive rings that produce internal pressure P_2, P_3, P_4 ,…, P_n. The above continuity equation lead to determination of the remaining interfacial pressures. Equations (19) and (20), together with Force-displacement equation lead us to the system of *2n* equations with *2n* unknown constants (where *n* is the number of the rings in the flywheel):

$$[K]\{C\} = \{R\} \qquad \text{Eq. (20)}$$

Where {C} is the vector composed of the unknown constants, [K] is the geometry and material matrix, [R] is the vector of (misfit δ) or applied force.

4.4. Research trends

Given the various benefits of flywheels as energy storage devices, such as their wide range of operation temperature, their low maintenance and long life, there is a desire to further push them towards the upper right corner of the Ragone plot (Figure 4-1) to make FESS with remarkably high power and energy density. In this regard, it seems that the bottle neck is improving the energy density of the flywheel. That is because a flywheel can brought to full stop in seconds to extract all the energy, and that the limitations on power density mainly reflects the limitations in utilizing the energy extracted from the flywheel. On the other hand, the increase in energy density of a flywheel can be observed from two angles: Structural design and Materials design. The former includes a host of techniques where the goal was to reduce the maximum stress of a flywheel at a

given angular velocity, so that higher angular velocities can be achieved. Several examples were presented in this chapter, such as employing rubber rings to lower radial stress. The second and complementary approach is a materials design approach, where novel materials are to be developed with higher strength and utilized in the flywheel to further increase the safe angular velocity of the wheel. The use of carbon fiber reinforced composites is an example of that. However, the advent of novel materials calls for a revisit of this approach. In the following sections we briefly presented our views on the topics.

4.4.1. Additive manufacturing

Additive manufacturing (AM) facilitates the fabrication of complicated geometries, eliminating the need for expensive tooling and multi-step processing [132]. Recently, direct deposition of metals facilitated manufacturing of the functionally graded materials (FGM) to provide exciting new alternatives for the design elements. Morvan et al. [133] fabricated the graded flywheel composed of two materials: Cobalt (light/strong) and Tungsten Carbide (heavy/weak) using the AM method. Authors performed the optimization to find the optimum gradient of materials properties and geometry along the radial direction of flywheel. Following that they 3D-printed the functionally graded composite on the LENS apparatus.

The additive manufacturing, specially advanced filament winding processes, can also be used to design FESS with optimal fiber arrangements that are nearly impossible to fabricate using other methods. An example is the development of the AVCO's "constant stress" flywheel that contains a bidirectional weave of fibers were placed in the hoop and radial directions (Figure 4-6(c)).

4.4.2. Nanomaterials

Nanomaterials such as nanotubes, platelets, nanofibers, etc. with exceptional mechanical properties are promising agents in reinforcing the composites [17, 47, 134, 135]. Materials scientists predicted that composites reinforced with nanoscale fillers have the potential to possess exceptional properties ranging from the mechanical property by tailoring of tensile modulus, strength [40, 136, 137], fracture toughness [138], or wear resistance [139] as well as electrical [40] and optical properties [140]. However, based on the results acquired so far, it is still not evident whether such exceptional properties of nano-reinforcement agents can be translated to bulk composite. The reasons include the poor dispersion of nanoscale reinforcements especially at high volume fractions (more than 5-10%). On the other hand, nanomaterials have a much higher surface area per unit volume compared to the meso-size particles and fibers (such as carbon fibers). Hence, they can bond much more efficiently with a polymer matrix. Hence, compare to microfibers, significantly lower levels of nanomaterial is required to alter the properties of a composite dramatically. The number of studies have demonstrated that levels below 5% of nanofillers can significantly alter the properties of the matrix [141]. Another limiting factor is the high cost of nanomaterials. However, the latter is a problem that can be remedied likely with more research on processing and more demand.

Epoxy composites with meso-sized particle fillers are attractive for component manufacture by techniques including injection molding and fiber impregnation because they have relatively low viscosity of the uncured composition. The same manufacturing methods can be applied to resin reinforced with the nanomaterials. However, given the large surface area of these particles, measures need to be taken to avoid agglomeration. Given the dispersion challenges and high costs of nanomaterials at the moment, it seems that FESS with hybrid fillers (microfibers and

74

nanofillers) is a promising path forward that strikes a balance between the benefits of nanomaterials in terms of increasing strength measures and cost is achieved. Alternatively, cheap nanomaterials may also be employed.

Boyle et al. [142] investigated the effect of TiO_2 nanowires on the mechanical properties of the composite flywheels. TiO_2 are relatively inexpensive, easy to prepare and easy to surface functionalize (a process required to achieve good bonding between filler and matrix, and to enhance dispersion). The composite flywheel was fabricated through winding of the carbon fiber in resin bath infused with TiO_2 nanowires functionalized with silane. The results from 3-point bending test of the composite flywheel showed that the incorporation of TiO_2 nanowires can increase the strength of the composite by 30 %. Authors noted that improvement in the mechanical properties of the composite flywheel has huge economic impact by reduction of about 20-30% in the flywheel energy storage cost. This improvement can lead to increase in the power capacity from 20 MW to 26 MW and energy capacity from 6.5 MW to 7.5 MW-service hours, which effectively decreases the average energy storage cost by 20-25%.

Lin et al. [143] proposed that the incorporation of the carbon nanotubes into the epoxy matrix could increase the performance of flywheels. The authors performed the Finite element analysis to calculate the stress field inside the centrifugally loaded flywheel ring. The authors suggested a design that involves the gradual changes of the nanotube concentration in the rotor along the radial direction. The nanotube concentration is higher in the inner part of the rotor to provide a higher strength for the composite. The nanotube concentration lowered while moving along the radial direction.

Herein, we have evaluated the role nanoscale reinforcing agent in strengthening and improving the fracture toughness of the composite flywheel. In this study following the results

75

obtained in the chapter 3, we have evaluated the role of the well-dispersed electrospun carbon nanofibers in the region of experiencing high radial stress with Finite Element Analysis (FEA).

The primary rotor was filament wound using a wet method wherein conventional carbon fiber passed through a resin bath and is wrapped around a mandrel sandwiched between two disks that form the flywheel's flat faces. Flywheels with diameter of 20 cm and 40 cm, with thickness of the 7 mm and the hub diameter of 24 mm is manufactured. In order to find the high radial stress region of the flywheel, FEM modeling of the wheel has been done. Critical angular velocity and region of the high radial stress has been identified. According to our model, improvement in the tensile strength and modulus of the CNFs/epoxy nanocomposite coupon can lead to improvement in critical angular velocity. Figure 4-9 shows the improvement in the critical angular velocity of 20 cm diameter flywheel infused with different mass ratio of CNFs in the epoxy matrix.

The composite flywheel with an average diameter of 40 cm and thickness of 7 mm operating at and average angular velocity of 79000 RPM is modeled with the aid of ABAQUS CAE, finite element software. Volume fraction of the fiber in the composite flywheel is considered to be 60% fiber (T700SC Toray). In each step, high radial stress region in the composite flywheel is replaced with hybrid multi-scale composite consisting of the matrix reinforced with 1 wt. % and 2 wt. % CNFs, respectively. Mechanical properties of the hybrid composite estimated using rule of mixture.

Our calculation shows that improving the region of experiencing high radial stress can increase the energy density of the flywheel by almost ~14%. Implementing the 2 wt% carbon nanofiber/epoxy in the region of high radial stress zone instead of conventional epoxy can boost the minimum angular velocity for fracture of the flywheel from 79000 RPM to 84000 RPM
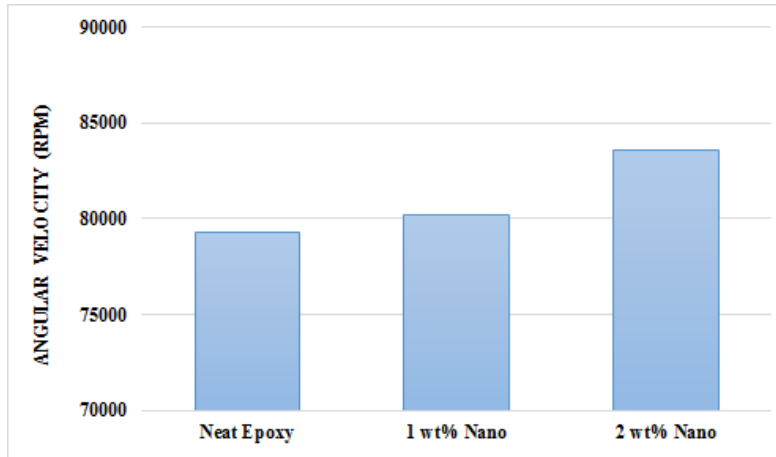
Figure 4-9: Improvement in the maximum allowable angular velocity of the flywheel

Figure 4-10 shows the schematic of the flywheel and the region experiencing the high radial stress. High radial stress zone of the flywheel was modified by the 1 wt.% and 2 wt.% of the CNFs/ epoxy which in turn shows the improvement in the critical angular velocity of flywheel before failure.
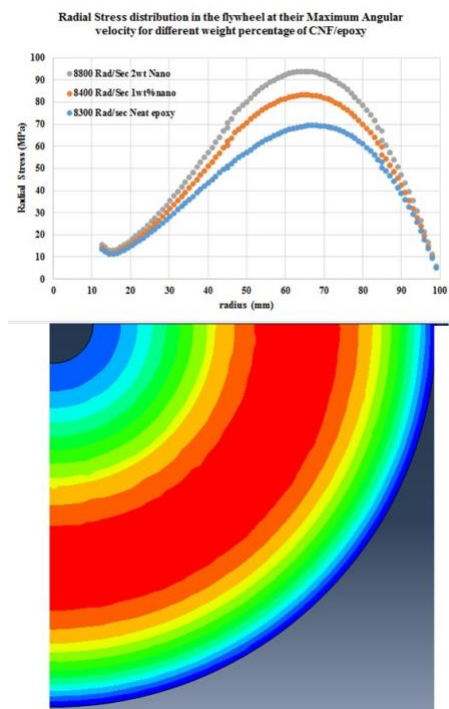
Figure 4-10: Radial stress along flywheel radius at different angular velocity

4.5. Conclusion

Despite the preliminary work, it seems a lot more needs to be carried out in terms of the application of nanomaterials to flywheels. The most intriguing path forward seems to be addressing the problems that are common between flywheels design and nanocomposite processing in general, such as nanofiller dispersion and alignment to better transfer load. Another intriguing direction is with respect to the specific application of nanomaterials to flywheels, including the variations of filler alignment and concentration as a function of radius to modulate strength and stiffness. This approach should be intended to both reduce stress fields (by modulating stiffness) and strength, allowing for higher angular velocities.

An economic impact of increasing the energy and power density using the nanomaterials in the high radial stress region is also significant. Based on the increase in the increase in critical angular velocity of the flywheel and also increase in the interlaminar fracture strength of flywheel carbon fiber-epoxy composite by almost 30%, a 20-30% reduction in flywheel energy storage cost ($/kW-h) may be enabled. This technological improvement will decrease the average storage cost to $1500/kW and $6000/kW-h. After accounting for new-technology and additional production costs, return on improved-nanocomposite investment is 4%-6% per year over 20-year service life.

Further work is underway to disperse the nanofiller evenly throughout the resin in order to garner the greatest impact. Once this is determined, the optimal nanofillers will be used to build mock flywheels and test their spin strengths/speeds.

5. SUMMARY AND FUTURE DIRECTION

5.1. Summary

The main goal of the presented work was to study the mechanics of hybrid composite flywheels with carbon microfibers and carbon nanofibers (CNFs) reinforcements under centrifugal forces and evaluate the role of nanoscale fillers in delaying failure caused by centrifugal forces and enhance gravimetric energy storage.

Since the major failure mode of the composite flywheels is the matrix-dominated failure, our study is focused on improving the resin strength. Herein, we studied the role of the nanofillers in improving the strength and fracture toughness of the resin. Nanofillers can be added at a very low level due to their higher surface areas and their exceptional mechanical properties. The nanofillers we used in this study was carbon nanofibers fabricated from electrospun Polyacrylonitrile (PAN) nanofibers.

To this end, three major objectives of this research study were set as I) Study the trade-offs between surface functionalization of CNFs as a means to enhance CNF-matrix load transfer and the mechanics of individual carbon nanofiber, II) Study the mechanics of CNF/epoxy nanocomposite and hybrid nano/micro fiber-reinforced composites as a function of dispersion, surface chemistry and mechanics of individual CNFs, and III) Study the failure mechanisms of flywheel subjected to centrifugal forces as a function of the nanofillers content.

Chemical functionalization intended to enhance carbon nanomaterial interactions with a polymer matrix while it may adversely affect the strength in individual nanomaterials by disrupting their graphitic structure. In this work, we evaluated the strength loss caused by functionalization in CNFs that are composed of a highly crosslinked network containing amorphous and graphitic carbon. Our study pointed to an optimum condition for chemical functionalization of the CNFs to

79

improve the functionality of the CNFs without any substantial loss in the strength of the CNFs. In addition, comparison of CNFs and carbon fibers with similar O/C ratio revealed that the nanomaterials can be much more sensitive to acid treatment effects on strength.

Our studies on the mechanics of the nanocomposites containg 1 wt. % of CNFs reaveled that nanocomposites containing functionalized CNFs have tensile strenght and modulus comparing to the prisitne CNFs. This is due to the higher interfacial bonding between the CNFs and epoxy matrix which comes from grafting functional groups on the CNFs surfaces. Effect of melamine functionalization on the mechanics of the CNFs/ epoxy nanocomposite was also studied. It is showed that melamine functionalization improve the interfacial bonding of the nanofillers in the polymer matrix and this led to an increase of about ~76% in the modulus of the nanocomposite containing 2 wt.% CNFs. Moreover, it is successfully shown that the strength of the nanocomposite containing 2 wt. % CNFs functionalized with melamine is increased to ~30% compare to neat epoxy specimens.

Our studies on the effect CNFs in improving the fracture toughness mode I of multiscale carbon fiber-carbon nanofibers composite pointed to an increase of at most 25% in the interlaminar fracture toughness of the carbon fiber composite laminate due to the introduction of CNFs mat interleafs in the interlaminar regions. The effect of the 2 wt. % CNFs/epoxy interleaf on mode I fracture toughness of the unidirectional fabric carbon fiber/epoxy composite was also compared to the those of non-interleaved control panels. A more moderate improvement of 18% for the case of B-staged CNF epoxy interleaves was observed. The results suggest that the addition of M-CNFs can effectively increase the crack initiation fracture toughness, but the crack follows an unstable growth pattern. While CNFs bridge crack growth and delay crack initiation, SEM images suggest

80

that the crack finds a lower resistance path by tearing the CNFs or propagating along the resin-rich interface of the CNF mats and the fibers.

Our results to pointed to an increase in the energy density of the flywheel to about ~14% by introduction of the CNFs mat in the interlayer regions. According to our model, improvement in the tensile strength, modulus and fracture toughness of the CNFs/epoxy nanocomposite coupon can lead to improvement in critical angular velocity of the flywheel from 79000 RPM to 84000 RPM.

5.2. Future directions

Through the discussions in the previous chapters and the summary presented above, a few immediate directions of the work in this thesis are presented below. They include fabrication of the long and continuous nanofibers, fabrication of the fast cured nanocomposites, and grafting of the CNFs on the surface of the CFs fabric for increasing the Fracture toughness.

5.2.1. Fabrication of the long and continuous CNFs

CNFs mat consists of thousands of entangled and bundled nanofibers. The diameter of the typical carbon nanofiber is in the range of the 100-500 nm. The reported strength of the single CNFs reaches to ~7 GPa which is comparable to the reported values of the high-strength carbon microfiber with an average diameter of 4.4 µm (IM10 Hexcel). However, the reported strength of the CNFs yarn is around 400 MPa (10 times smaller) which limits their application in terms of strengthening of nanocomposites.

There are number of possible underlying reasons which take in part to such difference. One of the main reasons is the discontinuous nature and short length of the nanofibers. As mentioned earlier in previous section of this thesis, CNFs went through multiple thermomechanical processes

to be fabricated such as stabilization and carbonization. Within these processes, soft and ductile PAN nanofiber turn into brittle and strong CNFs.

The force required to break the single carbon nanofiber based on the reported strength and diameter of the nanofiber is around few hundred micro-newtons (~100 µN) which is small enough to break nanofibers just by single touch.

Nanofibers are entangled and bundled randomly in the CNFs mat. Any point of the interaction where nanofibers crossing each others led to fracture of the nanofibers since nanofibers are orthotropic materials and their strength in other directions are much lower than longitudinal direction which led to easy fracture of the nanofibers. Due to such limitation, CNFs processing needs to be modified to avoid crossing and interaction of the nanofibers. One possible approach is to use the near-field electrospinning in which the electrospinning is more controllable and architecture of the nanofibers is not determined by the Taylor cone.

Another promising approach is to use co-axial electrospinning with the sacrificial outer polymeric layer. This sacrificial layer can cover the PAN nanofibers and will be removed during the thermomechanical processing of the CNF fabrication. This sacrificial layer cover and protect the CNFs and avoid their interaction. The suggested sacrificial layer can be polystyrene or polyamide which will be removed during the pyrolysis.

5.2.2. Grafting of CNFs on the surface of the CFs

As mentioned in the third chapter of this thesis, CNFs are able to bridge the cracks and improve the fracture toughness of the hybrid multi-scale composites. Nanofiber mat interleafs and B-staged nano-epoxy interlayer thin films are good candidate to reinforce the resin rich areas between the consecutive plies. However, fabrication of the hybrid composite with the above methods are limited to the pocket of epoxy formed between the fabric and such interleafs, either

nanofibers mat or B-staged nano-epoxy thin film. Resin rich areas are the weakest part ahead of the cracks and as crack progress they preferably propagate along these weak regions.

One possible approach to shorten the gap between the fabric and the nanofiber constituents is to graft and grow the nanomaterials on the surface of the fabric. Literature is abundant with number of methods to graft the nanomaterials on the surface of the fabric such as electrophoresis of CNTs or CVD growth of CNTs on the surface of CF fabric.

Our proposed approach was successfully capable of grafting melamine on the surface of the CNFs. Grafting the Melamine on the surface of the functionalized carbon fiber was also done following the method mentioned by Fang et al. However, Melamine can be used as glue to graft CNFs on the surface of the individuals CFs. Melamine has three amine group (-NH$_2$) and each amine group can be grafted to the carboxyl group on the surface of the surface of the either CFs or CNFs. If Melamine functionalization of the CFs and CNFs occurs simultaneously there would be a high chance of grafting the CNFs on the surface of the carbon fibers. In other words, melamine acts as a glues to graft CNFs on CF surface. This proposed approach can effectively increase the facture toughness and also enhance the interfacial bonding between fibers and matrix.

5.2.3. DMA/ DSC analysis of the epoxy thin film

There is an obvious difference between the measured value of the modulus of epoxy from the experiment and the modulus of the epoxy provided by the Miller Stephenson data sheet. The reported value of the modulus following the Miller Stephenson data sheet is 2.92 GPa. However, our reported value from the experiment is 1.5 GPa. It should be noted that specimen for different conditions and different loading of the CNFs were performed with the same epoxy resin (same bottle). This discrepancy may come from different sources. Here are some possible reason of such difference.

The First possible reason of this difference is our modified curing profile. The suggested ratio of the resin to hardener following the data sheet is (100:26.4). In our modified curing profile we added the total amount of the required hardener to resin in two steps. First, we added the 20% of the total amount of the hardener to the resin and stirred it for 3 hours at 120 C and after that we added the rest of the hardener at 80 and we degassed it. After all these procedures, we went through our modified curing profile to deter the agglomeration of the CNFs. Adding the curing agent in to steps may result in partially curing the epoxy and doesn't let the rest of the curing agent involve in the reaction.

The second possible reason could be the use of outdated resin which we have used it for fabricating of our samples. However, all the specimens are made with that resin and all the improvements are valid throughout the studies.

The future direction of this research study is to perform the DMA or DSC analysis to measure the transition glass temperature of the epoxy resin fabricated with our suggest curing profile. This will help us to find out if our epoxy system following our modified curing profile is cured completely or not.

Also there is a big jump in the modulus of epoxy when 2 wt. % melamine functionalized CNFs are added to the epoxy resin. We initially suggested that the possible reason for this difference is due to formation of interphase region around the CNFs which led to such increase. However, further research needs to be done to validate our hypothesis.

Another possible reason for such increase could be partially curing of the epoxy resin which led to the low modulus of the composite. However, when amine rich CNFs are added to the epoxy resin, curing of the epoxy is facilitated and modulus of the epoxy increased abruptly.

Due to this reason and other reasons mentioned earlier, author suggests performing the

DMA or DSC analysis to fully understand the underlying chemistry of this difference.

REFERENCES

[1]   B. Bolund, H. Bernhoff, and M. Leijon, "Flywheel energy and power storage systems," (in English), *Renew Sust Energ Rev,* vol. 11, no. 2, pp. 235-258, Feb 2007, doi: 10.1016/j.rser.2005.01.004.

[2]   A. H. Alami, "Flywheel Storage Systems," in *Mechanical Energy Storage for Renewable and Sustainable Energy Resources*: Springer, 2020, pp. 35-49.

[3]   D. W. Rabenhorst, "Potential applications for the superflywheel," in *Intersociety Energy Conversion Engineering Conference*, 1971, pp. 1118-1125.

[4]   S. DeTeresa and S. Groves, "Properties of fiber composites for advanced flywheel energy storage devices," Lawrence Livermore National Lab., CA (US), 2001.

[5]   T. Kawaguchi and R. A. Pearson, "The effect of particle–matrix adhesion on the mechanical behavior of glass filled epoxies. Part 2. A study on fracture toughness," *Polymer,* vol. 44, no. 15, pp. 4239-4247, 2003, doi: 10.1016/s0032-3861(03)00372-0.

[6]   J. Cha, S. Jin, J. H. Shim, C. S. Park, H. J. Ryu, and S. H. Hong, "Functionalization of carbon nanotubes for fabrication of CNT/epoxy nanocomposites," (in English), *Mater Design,* vol. 95, pp. 1-8, Apr 5 2016, doi: 10.1016/j.matdes.2016.01.077.

[7]   J. F. Shen, W. S. Huang, L. P. Wu, Y. Z. Hu, and M. X. Ye, "Thermo-physical properties of epoxy nanocomposites reinforced with amino-functionalized multi-walled carbon nanotubes," (in English), *Compos Part a-Appl S,* vol. 38, no. 5, pp. 1331-1336, 2007, doi: 10.1016/j.compositesa.2006.10.012.

[8]   V. Eskizeybek, A. Yar, and A. Avci, "CNT-PAN hybrid nanofibrous mat interleaved carbon/epoxy laminates with improved Mode I interlaminar fracture toughness," (in English), *Compos Sci Technol,* vol. 157, pp. 30-39, Mar 22 2018, doi: 10.1016/j.compscitech.2018.01.021.

[9]   Y. Li, N. Hori, M. Arai, N. Hu, Y. L. Liu, and H. Fukunaga, "Improvement of interlaminar mechanical properties of CFRP laminates using VGCF," (in English), *Compos Part a-Appl S,* vol. 40, no. 12, pp. 2004-2012, Dec 2009, doi: 10.1016/j.compositesa.2009.09.002.

[10]   Y. H. Tang, L. Ye, D. H. Zhang, and S. Q. Deng, "Characterization of transverse tensile, interlaminar shear and interlaminate fracture in CF/EP laminates with 10 wt% and 20 wt% silica nanoparticles in matrix resins," (in English), *Compos Part a-Appl S,* vol. 42, no. 12, pp. 1943-1950, Dec 2011, doi: 10.1016/j.compositesa.2011.08.019.

[11]   N. A. Siddiqui, R. S. Woo, J.-K. Kim, C. C. Leung, and A. Munir, "Mode I interlaminar fracture behavior and mechanical properties of CFRPs with nanoclay-filled epoxy matrix," *Composites Part A: Applied science and manufacturing,* vol. 38, no. 2, pp. 449-460, 2007.

[12]   S. Khatri, J. Z. Cai, and M. Naraghi, "Formation of wavy carbon nanofibers and nanocoils via precursor constrained microbuckling," (in English), *J Mech Phys Solids,* vol. 134, p. 103763, Jan 2020, doi: ARTN 10376310.1016/j.jmps.2019.103763.

[13]   Q. Chen, L. F. Zhang, A. Rahman, Z. P. Zhou, X. F. Wu, and H. Fong, "Hybrid multi-scale epoxy composite made of conventional carbon fiber fabrics with interlaminar regions containing electrospun carbon nanofiber mats," (in English), *Compos Part a-Appl S,* vol. 42, no. 12, pp. 2036-2042, Dec 2011, doi: 10.1016/j.compositesa.2011.09.010.

[14]   Q. Chen, W. D. Wu, Y. Zhao, M. Xi, T. Xu, and H. Fong, "Nano-epoxy resins containing electrospun carbon nanofibers and the resulting hybrid multi-scale composites," (in English), *Compos Part B-Eng,* vol. 58, pp. 43-53, Mar 2014, doi: 10.1016/j.compositesb.2013.10.048.

[15]   B. Peng *et al.*, "Measurements of near-ultimate strength for multiwalled carbon nanotubes and irradiation-induced crosslinking improvements," *Nat Nanotechnol,* vol. 3, no. 10, pp. 626 - 631, 2008, doi: doi:10.1038/nnano.2008.211.

[16]   M. F. Yu, B. S. Files, S. Arepalli, and R. S. Ruoff, "Tensile loading of ropes of single wall carbon nanotubes and their mechanical properties," (in English), *Phys. Rev. Lett.,* vol. 84, no. 24, pp. 5552-5555, Jun 12 2000. [Online]. Available: <Go to ISI>://000087522200024.

[17]   M. F. Yu, O. Lourie, M. J. Dyer, K. Moloni, T. F. Kelly, and R. S. Ruoff, "Strength and breaking mechanism of multiwalled carbon nanotubes under tensile load," (in English), *Science,* vol. 287, no. 5453, pp. 637-640, Jan 28 2000. [Online]. Available: <Go to ISI>://000084989400043.

[18]   C. Lee, X. D. Wei, J. W. Kysar, and J. Hone, "Measurement of the elastic properties and intrinsic strength of monolayer graphene," (in English), *Science,* vol. 321, no. 5887, pp. 385-388, Jul 18 2008, doi: DOI 10.1126/science.1157996.

[19]   T. Ramanathan *et al.*, "Functionalized graphene sheets for polymer nanocomposites," (in English), *Nat. Nanotechnol.,* vol. 3, no. 6, pp. 327-331, Jun 2008, doi: 10.1038/nnano.2008.96.

[20]   S. Roy, R. S. Petrova, and S. Mitra, "Effect of carbon nanotube (CNT) functionalization in Epoxy-CNT composites," (in eng), *Nanotechnol Rev,* vol. 7, no. 6, pp. 475-485, 2018, doi: 10.1515/ntrev-2018-0068.

[21]   R. J. Young, I. A. Kinloch, L. Gong, and K. S. Novoselov, "The mechanics of graphene nanocomposites: A review," (in English), *Compos. Sci. Technol.,* vol. 72, no. 12, pp. 1459-1476, Jul 23 2012, doi: 10.1016/j.compscitech.2012.05.005.

[22]   T. Ramanathan *et al.*, "Graphitic nanofillers in PMMA nanocomposites - An investigation of particle size influence on nanocomposite and dispersion and their properties," (in

English), *J. Polym. Sci. Pt. B-Polym. Phys.,* vol. 45, no. 15, pp. 2097-2112, Aug 1 2007, doi: 10.1002/polb.21187.

[23]   A. Mikhalchan, T. Gspann, and A. Windle, "Aligned carbon nanotube-epoxy composites: the effect of nanotube organization on strength, stiffness, and toughness," (in English), *J. Mater. Sci.,* vol. 51, no. 22, pp. 10005-10025, Nov 2016, doi: 10.1007/s10853-016-0228-6.

[24]   Q. F. Cheng *et al.*, "Carbon nanotube/epoxy composites fabricated by resin transfer molding," *Carbon,* vol. 48, no. 1, pp. 260-266, 2010/01/01/ 2010, doi: https://doi.org/10.1016/j.carbon.2009.09.014.

[25]   D. Tasis, N. Tagmatarchis, A. Bianco, and M. Prato, "Chemistry of carbon nanotubes," (in English), Chem. Rev., vol. 106, no. 3, pp. 1105-1136, Mar 2006, doi: 10.1021/cr050569o.

[26]   Y. H. Liao, O. Marietta-Tondin, Z. Y. Liang, C. Zhang, and B. Wang, "Investigation of the dispersion process of SWNTs/SC-15 epoxy resin nanocomposites," (in English), *Materials Science and Engineering a-Structural Materials Properties Microstructure and Processing,* vol. 385, no. 1-2, pp. 175-181, Nov 15 2004, doi: 10.1016/j.msea.2004.06.031.

[27]   T. Xiao, J. Liu, and H. Xiong, "Effects of different functionalization schemes on the interfacial strength of carbon nanotube polyethylene composite," *Acta Mechanica Solida Sinica,* vol. 28, no. 3, pp. 277-284, 2015/06/01/ 2015, doi: https://doi.org/10.1016/S0894-9166(15)30014-8.

[28]   Z. Q. Zhang, B. Liu, Y. L. Chen, H. Jiang, K. C. Hwang, and Y. Huang, "Mechanical properties of functionalized carbon nanotubes," (in English), *Nanotechnology,* vol. 19, no. 39, Oct 1 2008, doi: Artn 395702 Doi 10.1088/0957-4484/19/39/395702.*

[29]   *S. L. Mielke et al., "The role of vacancy defects and holes in the fracture of carbon* nanotubes," (in English), *Chem. Phys. Lett.,* vol. 390, no. 4-6, pp. 413-420, Jun 1 2004, doi: 10.1016/j.cplett.2004.04.054.

[30]   A. Zandiatashbar *et al.*, "Effect of defects on the intrinsic strength and stiffness of graphene," (in English), *Nat. Commun.,* vol. 5, Jan 2014, doi: Artn 318610.1038/Ncomms4186.*

[31]   *A. R. Khoei and M. S. Khorrami, "Mechanical properties of graphene oxide: A molecular* dynamics study," (in English), *Fuller Nanotub Car N,* vol. 24, no. 9, pp. 594-603, 2016, doi: 10.1080/1536383x.2016.1208180.

[32]   L. T. Drzal, N. Sugiura, and D. Hook, "The role of chemical bonding and surface topography in adhesion between carbon fibers and epoxy matrices," *Composite Interfaces,* vol. 4, no. 5, pp. 337-354, 1996/01/01 1996, doi: https://doi.org/10.1163/156855497X00073.

[33] O. P. Bahl, R. B. Mathur, and T. L. Dhami, "Effects of Surface-Treatment on the Mechanical-Properties of Carbon-Fibers," (in English), *Polym. Eng. Sci.,* vol. 24, no. 7, pp. 455-459, 1984, doi: DOI 10.1002/pen.760240702.

[34] A. M. Beese, D. Papkov, S. Y. Li, Y. Dzenis, and H. D. Espinosa, "In situ transmission electron microscope tensile testing reveals structure-property relationships in carbon nanofibers," (in English), *Carbon,* vol. 60, pp. 246-253, Aug 2013, doi: 10.1016/j.carbon.2013.04.018.

[35] D. Papkov *et al.*, "Extraordinary Improvement of the Graphitic Structure of Continuous Carbon Nanofibers Templated with Double Wall Carbon Nanotubes," (in English), *ACS Nano,* vol. 7, no. 1, pp. 126-142, Jan 2013, doi: Doi 10.1021/Nn303423x.

[36] S. Chawla, J. Z. Cai, and M. Naraghi, "Mechanical tests on individual carbon nanofibers reveals the strong effect of graphitic alignment achieved via precursor hot-drawing," (in English), *Carbon,* vol. 117, pp. 208-219, Jun 2017, doi: 10.1016/j.carbon.2017.02.095.

[37] E. Zussman *et al.*, "Mechanical and structural characterization of electrospun PAN-derived carbon nanofibers," (in English), *Carbon,* vol. 43, no. 10, pp. 2175-2185, Aug 2005, doi: 10.1016/j.carbon.2005.03.031.

[38] S. N. Arshad, M. Naraghi, and I. Chasiotis, "Strong carbon nanofibers from electrospun polyacrylonitrile," (in English), *Carbon,* vol. 49, no. 5, pp. 1710-1719, Apr 2011, doi: 10.1016/j.carbon.2010.12.056.

[39] Y. Chen, A. Amiri, J. G. Boyd, and M. Naraghi, "Promising Trade-Offs Between Energy Storage and Load Bearing in Carbon Nanofibers as Structural Energy Storage Devices," *Advanced Functional Materials,* vol. 29, no. 33, p. 1901425, 2019.

[40] F. Gardea and D. C. Lagoudas, "Characterization of electrical and thermal properties of carbon nanotube/epoxy composites," (in English), *Compos Part B-Eng,* vol. 56, pp. 611-620, Jan 2014, doi: 10.1016/j.compositesb.2013.08.032.

[41] M. Naraghi and S. Chawla, "Carbonized Micro- and Nanostructures: Can Downsizing Really Help?," *Materials (Basel),* vol. 7, no. 5, pp. 3820-3833, May 14 2014, doi: 10.3390/ma7053820.

[42] G. Krekel, K. J. H�ttinger, W. P. Hoffman, and D. S. Silver, "The relevance of the surface structure and surface chemistry of carbon fibres in their adhesion to high-temperature thermoplastics," *Journal of Materials Science,* vol. 29, no. 11, pp. 2968-2980, 1994/06/01 1994, doi: 10.1007/bf01117609.

[43] S. Rana, R. Alagirusamy, R. Fangueiro, and M. Joshi, "Effect of carbon nanofiber functionalization on the in-plane mechanical properties of carbon/epoxy multiscale

composites," *Journal of Applied Polymer Science,* vol. 125, no. 3, pp. 1951-1958, 2012, doi: https://doi.org/10.1002/app.36302.

[44]   K. L. Klein *et al.*, "Surface characterization and functionalization of carbon nanofibers," (in English), *J. Appl. Phys.,* vol. 103, no. 6, Mar 15 2008, doi: Artn 06130110.1063/1.2840049.

[45]   K. L. Klein et al., "Surface characterization and functionalization of carbon nanofibers," (in English), *J Appl Phys,* vol. 103, no. 6, p. 061301, Mar 15 2008, doi: Artn 06130110.1063/1.2840049.

[46]   S. D. Gardner, C. S. K. Singamsetty, G. L. Booth, G. R. He, and C. U. Pittman, "Surface Characterization of Carbon-Fibers Using Angle-Resolved Xps and Iss," (in English), *Carbon,* vol. 33, no. 5, pp. 587-595, 1995, doi: Doi 10.1016/0008-6223(94)00144-O.

[47]   J. Cai and M. Naraghi, "Non-intertwined graphitic domains leads to super strong and tough continuous 1D nanostructures," *Carbon,* vol. 137, pp. 242-251, 2018/10/01/ 2018, doi: https://doi.org/10.1016/j.carbon.2018.05.030.

[48]   Y. Chen, J. Cai, J. G. Boyd, W. J. Kennedy, and M. Naraghi, "Mechanics of Emulsion Electrospun Porous Carbon Fibers as Building Blocks of Multifunctional Materials," *ACS Appl Mater Interfaces,* vol. 10, no. 44, pp. 38310-38318, Nov 7 2018, doi: 10.1021/acsami.8b10499.

[49]   Z. H. Wu, C. U. Pittman, and S. D. Gardner, "Nitric-Acid Oxidation of Carbon-Fibers and the Effects of Subsequent Treatment in Refluxing Aqueous Naoh," (in English), *Carbon,* vol. 33, no. 5, pp. 597-605, 1995, doi: Doi 10.1016/0008-6223(95)00145-4.

[50]   H. Gao, B. Ji, I. L. JÃ¤ger, E. Arzt, and P. Fratzl, "Materials become insensitive to flaws at nanoscale: Lessons from nature," *Proceedings of the National Academy of Sciences,* vol. 100, no. 10, pp. 5597-5600, May 13, 2003 2003, doi: 10.1073/pnas.0631609100.

[51]   M. Erickson and M. Kirk, "Direct Use of Fracture Toughness for Flaw Evaluations of Pressure Boundary Materials in Section XI, Division 1, Class 1 Ferritic Steel Components," (in English), *Proceedings of the Asme Pressure Vessels and Piping Conference, 2017, Vol 1a,* 2017. [Online]. Available: <Go to ISI>://WOS:000422810300005.

[52]   C. H. Cao *et al.*, "Nonlinear fracture toughness measurement and crack propagation resistance of functionalized graphene multilayers," (in English), *Sci Adv,* vol. 4, no. 4, Apr 2018, doi: ARTN eaao720210.1126/sciadv.aao7202.

[53]   L. Yang, I. Greenfeld, and H. D. Wagner, "Toughness of carbon nanotubes conforms to classic fracture mechanics," (in English), *Sci Adv,* vol. 2, no. 2, Feb 2016, doi: UNSP e150096910.1126/sciadv.1500969.

[54]   X. S. Zhang, Y. J. Chen, and J. L. Hu, "Recent advances in the development of aerospace materials," (in English), *Prog Aerosp Sci,* vol. 97, pp. 22-34, Feb 2018, doi: 10.1016/j.paerosci.2018.01.001.

[55]   M. S. Scholz *et al.*, "The use of composite materials in modern orthopaedic medicine and prosthetic devices: A review," (in English), *Compos Sci Technol,* vol. 71, no. 16, pp. 1791-1803, Nov 14 2011, doi: 10.1016/j.compscitech.2011.08.017.

[56]   K. Talukdar, *Nanomaterials-Based Composites for Energy Applications: Emerging Technology and Trends*. CRC Press, 2020.

[57]   B. Haghgouyan, C. Hayrettin, T. Baxevanis, I. Karaman, and D. C. Lagoudas, "Fracture toughness of niti–towards establishing standard test methods for phase transforming materials," *Acta Materialia,* vol. 162, pp. 226-238, 2019.

[58]   S. Goldstein, R. J. Levy, V. Labhasetwar, and J. F. Bonadio, "Compositions and methods for coating medical devices," USA Patent Appl. 08/662341, 2000.

[59]   A. P. Mouritz, C. Baini, and I. Herszberg, "Mode I interlaminar fracture toughness properties of advanced textile fibreglass composites," (in English), *Compos Part a-Appl S,* vol. 30, no. 7, pp. 859-870, 1999, doi: Doi 10.1016/S1359-835x(98)00197-3.

[60]   E. N. Gilbert, B. S. Hayes, and J. C. Seferis, "Interlayer toughened unidirectional carbon prepreg systems: effect of preformed particle morphology," (in English), *Compos Part a-Appl S,* vol. 34, no. 3, pp. 245-252, 2003, doi: Pii S1359-835x(02)00141-0 Doi 10.1016/S1359-835x(02)00141-0.

[61]   L. Tong, A. P. Mouritz, and M. Bannister, 3D fibre reinforced polymer composites. Elsevier, 2002.

[62]   K. Dransfield, C. Baillie, and Y.-W. Mai, "Improving the delamination resistance of CFRP by stitching—a review," *Compos Sci Technol,* vol. 50, no. 3, pp. 305-317, 1994, doi: 10.1016/0266-3538(94)90019-1.

[63]   R. T. Brown and E. C. Crow Jr, "Automatic through-the-thickness braiding," in *37th international SAMPE symposium and exhibition*, 1992, pp. 832-842.

[64]   L. W. Byrd and V. Birman, "Effectiveness of z-pins in preventing delamination of co-cured composite joints on the example of a double cantilever test," (in English), *Compos Part B-Eng,* vol. 37, no. 4-5, pp. 365-378, 2006, doi: 10.1016/j.compositesb.2005.05.019.

[65]   L. K. Jain and Y. W. Mai, "In the Effect of Stitching on Mode-I Delamination Toughness of Laminated Composites," (in English), *Compos Sci Technol,* vol. 51, no. 3, pp. 331-345, 1994, doi: Doi 10.1016/0266-3538(94)90103-1.

[66]   I. K. Partridge and D. D. R. Cartié, "Delamination resistant laminates by Z-Fiber® pinning: Part I manufacture and fracture performance," *Composites Part A: Applied Science and Manufacturing,* vol. 36, no. 1, pp. 55-64, 2005, doi: 10.1016/s1359-835x(04)00180-0.

[67]   S. K. Sharma and B. V. Sankar, "Effect of stitching on impact and interlaminar properties of graphite/epoxy laminates," (in English), *J Thermoplast Compos,* vol. 10, no. 3, pp. 241-253, May 1997, doi: Doi 10.1177/089270579701000302.

[68]   X. Zhang, L. Hounslow, and M. Grassi, "Improvement of low-velocity impact and compression-after-impact performance by z-fibre pinning," (in English), *Compos Sci Technol,* vol. 66, no. 15, pp. 2785-2794, Dec 2006, doi: 10.1016/j.compscitech.2006.02.029.

[69]   R. P. Singh, M. Zhang, and D. Chan, "Toughening of a brittle thermosetting polymer: Effects of reinforcement particle size and volume fraction," (in English), *J Mater Sci,* vol. 37, no. 4, pp. 781-788, Feb 15 2002, doi: Doi 10.1023/A:1013844015493.

[70]   A. F. Yee and R. A. Pearson, "Toughening mechanisms in elastomer-modified epoxies," *J Mater Sci,* vol. 21, no. 7, pp. 2462-2474, 1986, doi: 10.1007/bf01114293.

[71]   L. Aktas, D. P. Bauman, S. T. Bowen, M. C. Saha, and M. C. Altan, "Effect of Distribution Media Length and Multiwalled Carbon Nanotubes on the Formation of Voids in VARTM Composites," (in English), *Journal of Engineering Materials and Technology-Transactions of the ASME,* vol. 133, no. 4, Oct 2011, doi: Artn 04100610.1115/1.4004700.

[72]   Z. H. Fan, M. H. Santare, and S. G. Advani, "Interlaminar shear strength of glass fiber reinforced epoxy composites enhanced with multi-walled carbon nanotubes," (in English), *Composites Part a-Applied Science and Manufacturing,* vol. 39, no. 3, pp. 540-554, 2008, doi: 10.1016/j.compositesa.2007.11.013.

[73]   R. J. Sager, P. J. Klein, D. C. Davis, D. C. Lagoudas, G. L. Warren, and H. J. Sue, "Interlaminar Fracture Toughness of Woven Fabric Composite Laminates with Carbon Nanotube/Epoxy Interleaf Films," (in English), *J Appl Polym Sci,* vol. 121, no. 4, pp. 2394-2405, Aug 15 2011, doi: 10.1002/app.33479.

[74]   L. Liu, L. L. Shen, and Y. X. Zhou, "Improving the interlaminar fracture toughness of carbon/epoxy laminates by directly incorporating with porous carbon nanotube buckypaper," (in English), *J Reinf Plast Comp,* vol. 35, no. 2, pp. 165-176, Jan 2016, doi: 10.1177/0731684415610919.

[75]   H. Qian, E. S. Greenhalgh, M. S. P. Shaffer, and A. Bismarck, "Carbon nanotube-based hierarchical composites: a review," (in English), *J. Mater. Chem.,* vol. 20, no. 23, pp. 4751-4762, 2010, doi: 10.1039/c000041h.

[76]   R. Sadeghian, S. Gangireddy, B. Minaie, and K. T. Hsiao, "Manufacturing carbon nanofibers toughened polyester/glass fiber composites using vacuum assisted resin transfer molding for enhancing the mode-I delamination resistance," (in English), *Composites Part a-Applied Science and Manufacturing,* vol. 37, no. 10, pp. 1787-1795, 2006, doi: 10.1016/j.compositesa.2005.09.010.

[77]   P. Karapappas, A. Vavouliotis, P. Tsotra, V. Kostopoulos, and A. Paipetis, "Enhanced Fracture Properties of Carbon Reinforced Composites by the Addition of Multi-Wall Carbon Nanotubes," (in English), *J. Compos. Mater.,* vol. 43, no. 9, pp. 977-985, May 2009, doi: 10.1177/0021998308097735.

[78]   Y. A. Dzenis and D. H. Reneker, "Delamination resistant composites prepared by small diameter fiber reinforcement at ply interfaces," USA Patent US 6,265,333, 2001.

[79]   G. Li *et al.*, "Inhomogeneous toughening of carbon fiber/epoxy composite using electrospun polysulfone nanofibrous membranes by in situ phase separation," (in English), *Compos Sci Technol,* vol. 68, no. 3-4, pp. 987-994, Mar 2008, doi: 10.1016/j.compscitech.2007.07.010.

[80]   A. Zucchelli, M. L. Focarete, C. Gualandi, and S. Ramakrishna, "Electrospun nanofibers for enhancing structural performance of composite materials," *Polymers for Advanced Technologies,* vol. 22, no. 3, pp. 339-349, 2011.

[81]   E. Sancaktar and D. Aussawasathien, "Nanocomposites of Epoxy with Electrospun Carbon Nanofibers: Mechanical Behavior," (in English), *J. Adhes.,* vol. 85, no. 4-5, pp. 160-179, 2009, doi: Pii 91123380510.1080/00218460902881758.

[82]   S. R. Dhakate et al., "Excellent mechanical properties of carbon fiber semi-aligned electrospun carbon nanofiber hybrid polymer composites," (in English), *Rsc Adv,* vol. 6, no. 43, pp. 36715-36722, 2016, doi: 10.1039/c6ra02672a.

[83]   J. Z. Cai, S. Chawla, and M. Naraghi, "Microstructural evolution and mechanics of hot-drawn CNT-reinforced polymeric nanofibers," (in English), *Carbon,* vol. 109, pp. 813-822, Nov 2016, doi: 10.1016/j.carbon.2016.08.080.

[84]   M. Zhao *et al.*, "Layer-by-layer grafting CNTs onto carbon fibers surface for enhancing the interfacial properties of epoxy resin composites," *Compos. Sci. Technol.,* vol. 154, pp. 28-36, 2018/01/18/ 2018, doi: https://doi.org/10.1016/j.compscitech.2017.11.002.

[85]   Q. Peng *et al.*, "Interfacial enhancement of carbon fiber composites by poly(amido amine) functionalization," *Compos. Sci. Technol.,* vol. 74, pp. 37-42, 2013/01/24/ 2013, doi: https://doi.org/10.1016/j.compscitech.2012.10.005.

[86] Q. Y. Peng *et al.*, "Interfacial enhancement of carbon fiber composites by poly(amido amine) functionalization," (in English), *Composites Science and Technology,* vol. 74, pp. 37-42, Jan 24 2013, doi: 10.1016/j.compscitech.2012.10.005.

[87] M. Zhao *et al.*, "Layer-by-layer grafting CNTs onto carbon fibers surface for enhancing the interfacial properties of epoxy resin composites," (in English), *Composites Science and Technology,* vol. 154, pp. 28-36, Jan 18 2018, doi: 10.1016/j.compscitech.2017.11.002.

[88] J. Z. Cai and M. Naraghi, "Non-intertwined graphitic domains leads to super strong and tough continuous 1D nanostructures," (in English), *Carbon,* vol. 137, pp. 242-251, Oct 2018, doi: 10.1016/j.carbon.2018.05.030.

[89] J. Kavosi, T. Creasy, A. Palazzolo, and M. Naraghi, "Crosslinked Network Microstructure of Carbon Nanomaterials Promotes Flaw-Tolerant Mechanical Response," *Nanotechnology,* Apr 21 2020, doi: 10.1088/1361-6528/ab8b92.

[90] H. Krenchel, *Fibre reinforcement : theoretical and practical investigations of the elasticity and strength of fibre-reinforced materials*. Copenhagen: Akademisk forlag (in English), 1964.

[91] K. W. Putz, M. J. Palmeri, R. B. Cohn, R. Andrews, and L. C. Brinson, "Effect of cross-link density on interphase creation in polymer nanocomposites," (in English), *Macromolecules,* vol. 41, no. 18, pp. 6752-6756, Sep 23 2008, doi: 10.1021/ma800830p.

[92] Y. Gu, M. Li, J. Wang, and Z. Zhang, "Characterization of the interphase in carbon fiber/polymer composites using a nanoscale dynamic mechanical imaging technique," *Carbon,* vol. 48, no. 11, pp. 3229-3235, 2010.

[93] R. Folkson, *Alternative fuels and advanced vehicle technologies for improved environmental performance: towards zero carbon transportation*. Elsevier, 2014.

[94] X. Zhao, B. M. Sanchez, P. J. Dobson, and P. S. Grant, "The role of nanomaterials in redox-based supercapacitors for next generation energy storage devices," *Nanoscale,* vol. 3, no. 3, pp. 839-55, Mar 2011, doi: 10.1039/c0nr00594k.

[95] T. Christen and M. W. Carlen, "Theory of Ragone plots," *Journal of Power Sources,* vol. 91, no. 2, pp. 210-216, 2000/12/01/ 2000, doi: https://doi.org/10.1016/S0378-7753(00)00474-2.

[96] Y. Kato *et al.*, "High-power all-solid-state batteries using sulfide superionic conductors," *Nature Energy,* vol. 1, no. 4, p. 16030, 2016/03/21 2016, doi: 10.1038/nenergy.2016.30.

[97] T. Christen and C. Ohler, "Optimizing energy storage devices using Ragone plots," *Journal of Power Sources,* vol. 110, no. 1, pp. 107-116, 2002.

[98]   D. V. Ragone, "Review of battery systems for electrically powered vehicles," SAE Technical Paper, 0148-7191, 1968.

[99]   J. W. Choi and D. Aurbach, "Promise and reality of post-lithium-ion batteries with high energy densities," *Nature Reviews Materials,* vol. 1, no. 4, p. 16013, 2016.

[100]   S. Chu, Y. Cui, and N. Liu, "The path towards sustainable energy," *Nature materials,* vol. 16, no. 1, p. 16, 2017.

[101]   K. J. Zhao, M. Pharr, J. J. Vlassak, and Z. G. Suo, "Fracture of electrodes in lithium-ion batteries caused by fast charging," (in English), *J Appl Phys,* vol. 108, no. 7, p. 073517, Oct 1 2010, doi: Artn 07351710.1063/1.3492617.

[102]   P. G. Balakrishnan, R. Ramesh, and T. P. Kumar, "Safety mechanisms in lithium-ion batteries," (in English), *Journal of Power Sources,* vol. 155, no. 2, pp. 401-414, Apr 21 2006, doi: 10.1016/j.jpowsour.2005.12.002.

[103]   J. M. Tarascon and M. Armand, "Issues and challenges facing rechargeable lithium batteries," *Nature,* vol. 414, no. 6861, pp. 359-67, Nov 15 2001, doi: 10.1038/35104644.

[104]   Y. Sun, N. Liu, and Y. Cui, "Promises and challenges of nanomaterials for lithium-based rechargeable batteries," *Nature Energy,* vol. 1, no. 7, pp. 1-12, 2016.

[105]   Y. Yang, G. Zheng, and Y. Cui, "Nanostructured sulfur cathodes," *Chem Soc Rev,* vol. 42, no. 7, pp. 3018-32, Apr 7 2013, doi: 10.1039/c2cs35256g.

[106]   P. G. Bruce, S. A. Freunberger, L. J. Hardwick, and J.-M. Tarascon, "Li–O2 and Li–S batteries with high energy storage," *Nature Materials,* vol. 11, no. 1, pp. 19-29, 2012/01/01 2012, doi: 10.1038/nmat3191.

[107]   D. Lisbona and T. Snee, "A review of hazards associated with primary lithium and lithium-ion batteries," (in English), *Process Saf Environ,* vol. 89, no. 6, pp. 434-442, Nov 2011, doi: 10.1016/j.psep.2011.06.022.

[108]   M. Salanne *et al.*, "Efficient storage mechanisms for building better supercapacitors," *Nature Energy,* vol. 1, no. 6, p. 16070, 2016.

[109]   X. Lang, A. Hirata, T. Fujita, and M. Chen, "Nanoporous metal/oxide hybrid electrodes for electrochemical supercapacitors," *Nature nanotechnology,* vol. 6, no. 4, p. 232, 2011.

[110]   V. Ruiz, C. Blanco, M. Granda, and R. Santamaría, "Enhanced life-cycle supercapacitors by thermal treatment of mesophase-derived activated carbons," *Electrochimica Acta,* vol. 54, no. 2, pp. 305-310, 2008.

[111] A. Burke, "Ultracapacitor technologies and application in hybrid and electric vehicles," (in English), *International Journal of Energy Research,* vol. 34, no. 2, pp. 133-151, Feb 2010, doi: 10.1002/er.1654.

[112] R. Kotz, M. Hahn, and R. Gallay, "Temperature behavior and impedance fundamentals of supercapacitors," (in English), *J Power Sources,* vol. 154, no. 2, pp. 550-555, Mar 21 2006, doi: 10.1016/j.jpowsour.2005.10.048.

[113] J. W. Ross, "On the Optimization of Composite Flywheel Rotors," Doctor of Philosophy Doctoral dissertation, Engineering Science and Mechanics, Penn state university, 2013. [Online]. Available: https://etda.libraries.psu.edu/catalog/18997

[114] H. Abdi, B. Mohammadi-ivatloo, S. Javadi, A. R. Khodaei, and E. Dehnavi, "Energy Storage Systems," in *Distributed Generation Systems*, G. B. Gharehpetian and S. M. Mousavi Agah Eds.: Butterworth-Heinemann, 2017, pp. 333-368.

[115] P. J. Hall and E. J. Bain, "Energy-storage technologies and electricity generation," *Energy policy,* vol. 36, no. 12, pp. 4352-4355, 2008.

[116] G. Genta, *Kinetic energy storage: theory and practice of advanced flywheel systems*. Butterworth-Heinemann, 2014.

[117] P. B. Mohr and C. E. Walter, "Flywheel rotor and containment technology development. Final report," Lawrence Livermore National Lab., CA (USA), 1983.

[118] D. W. Rabenhorst, "Potential applications for the superflywheel," in *Proceedings of the 6th Inetrsociety Energy Conversion Engineering Conference*, 1971, pp. 1118-1125.

[119] M. A. Arslan, "Flywheel geometry design for improved energy storage using finite element analysis," (in English), *Mater Design,* vol. 29, no. 2, pp. 514-518, 2008, doi: 10.1016/j.matdes.2007.01.020.

[120] E. L. Danfelt, S. A. Hewes, and T. W. Chou, "Optimization of Composite Flywheel Design," (in English), *International Journal of Mechanical Sciences,* vol. 19, no. 2, pp. 69-78, 1977/02/01/ 1977, doi: Doi 10.1016/0020-7403(77)90001-7.

[121] G. Genta, "On the Design of Thick Rim Composite-Material Filament Wound Flywheels," (in English), *Composites,* vol. 15, no. 1, pp. 49-55, 1984, doi: Doi 10.1016/0010-4361(84)90961-3.

[122] K. Miyata, "Optimal Structure of Fiber-Reinforced Flywheels with Maximized Energy Density," (in English), *B Jsme,* vol. 28, no. 238, pp. 565-570, 1985, doi: https://doi.org/10.1299/jsme1958.28.565.

[123] S. K. Ha, H. I. Yang, and D. J. Kim, "Optimal design of a hybrid composite flywheel with a permanent magnet rotor," (in English), *Journal of Composite Materials,* vol. 33, no. 16, pp. 1544-1575, 1999, doi: Doi 10.1177/002199839903301605.

[124] S. K. Ha, S. J. Kim, S. U. Nasir, and S. C. Han, "Design optimization and fabrication of a hybrid composite flywheel rotor," (in English), *Composite Structures,* vol. 94, no. 11, pp. 3290-3299, Nov 2012, doi: 10.1016/j.compstruct.2012.04.015.

[125] S. Manson, "Determination of elastic stresses in gas-turbine disks," *NACA Technical Note 1279.,* January 01, 1947 1947, Art no. 19930081895 [Online]. Available: https://ntrs.nasa.gov/search.jsp?R=19930081895.

[126] Lekhnitskii, S.G., *Anisotropic Plates*, *2nd Ed.*, 1968, Translated from the 2nd Russian Ed.by S.W. Tsai and Cheron, Bordon and Breach,

[127] C. W. Gabrys and C. E. Bakis, "Design and testing of composite flywheel rotors," in *Composite Materials: Testing and Design, Thirteenth Volume*: ASTM International, 1997.

[128] S. M. Arnold, A. F. Saleeb, and N. R. Al-Zoubi, "Deformation and life analysis of composite flywheel disk systems," (in English), *Compos Part B-Eng,* vol. 33, no. 6, pp. 433-459, 2002, doi: Pii S1359-8368(02)00032-X Doi 10.1016/S1359-8368(02)00032-X.

[129] S. Arnold, A. Saleeb, and N. Al-Zoubi, "Deformation and life analysis of composite flywheel disk systems," *Composites part B: engineering,* vol. 33, no. 6, pp. 433-459, 2002.

[130] S. K. Ha, M. H. Kim, S. C. Han, and T. H. Sung, "Design and spin test of a hybrid composite flywheel rotor with a split type hub," (in English), *Journal of Composite Materials,* vol. 40, no. 23, pp. 2113-2130, Dec 2006, doi: 10.1177/0021998306061324.

[131] S. Arnold, A. F. Saleeb, and N. AlZoubi, "Deformation and life analysis of composite flywheel disk and multi-disk systems," 2001.

[132] L. Costa and R. Vilar, "Laser powder deposition," (in English), *Rapid Prototyping Journal,* vol. 15, no. 4, pp. 264-279, 2009, doi: 10.1108/13552540910979785.

[133] S. Morvan, G. Fadel, J. Love, and D. Keicher, "Manufacturing of a Heterogeneous Flywheel on a LENS Apparatus 553," in *2001 International Solid Freeform Fabrication Symposium*, 2001.

[134] S. Chawla, J. Cai, and M. Naraghi, "Mechanical tests on individual carbon nanofibers reveals the strong effect of graphitic alignment achieved via precursor hot-drawing," *Carbon,* vol. 117, pp. 208-219, 6// 2017, doi: http://dx.doi.org/10.1016/j.carbon.2017.02.095.

[135]	C. Lee, X. Wei, J. W. Kysar, and J. Hone, "Measurement of the elastic properties and intrinsic strength of monolayer graphene," *Science,* vol. 321, no. 5887, pp. 385-8, Jul 18 2008, doi: 10.1126/science.1157996.

[136]	D. Sun, C. C. Chu, and H. J. Sue, "Simple Approach for Preparation of Epoxy Hybrid Nanocomposites Based on Carbon Nanotubes and a Model Clay," (in English), *Chemistry of Materials,* vol. 22, no. 12, pp. 3773-3778, Jun 22 2010, doi: 10.1021/cm1009306.

[137]	S. Peeterbroeck *et al.*, "Polymer-layered silicate–carbon nanotube nanocomposites: unique nanofiller synergistic effect," *Composites Science and Technology,* vol. 64, no. 15, pp. 2317-2323, 2004.

[138]	S. Q. Li, F. Wang, Y. Wang, J. W. Wang, J. Ma, and J. Xiao, "Effect of acid and TETA modification on mechanical properties of MWCNTs/epoxy composites," (in English), *Journal of Materials Science,* vol. 43, no. 8, pp. 2653-2658, Apr 2008, doi: 10.1007/s10853-008-2489-1.

[139]	E. Vassileva and K. Friedrich, "Epoxy/alumina nanoparticle composites. II. Influence of silane coupling agent treatment on mechanical performance and wear resistance," (in English), *Journal of Applied Polymer Science,* vol. 101, no. 6, pp. 4410-4417, Sep 15 2006, doi: 10.1002/app.23297.

[140]	M. Nyman, L. E. Shea-Rohwer, J. E. Martin, and P. Provencio, "Nano-YAG:Ce Mechanisms of Growth and Epoxy-Encapsulation," (in English), *Chemistry of Materials,* vol. 21, no. 8, pp. 1536-1542, Apr 28 2009, doi: 10.1021/cm803137h.

[141]	Z. H. Guo, T. Pereira, O. Choi, Y. Wang, and H. T. Hahn, "Surface functionalized alumina nanoparticle filled polymeric nanocomposites with enhanced mechanical properties," (in English), *Journal of Materials Chemistry,* vol. 16, no. 27, pp. 2800-2808, 2006, doi: 10.1039/b603020c.

[142]	T. J. Boyle, N. Bell, M. Ehlen, B. Anderson, and W. Miller, "Improved Flywheel Materials: Characterization of Nanofiber Modified Flywheel Test Specimen," 2013.

[143]	K.-C. Lin, J. Gou, C. Ham, S. Helkin, and Y. H. Joo, "Flywheel energy storage system with functionally gradient nanocomposite rotor," in *2010 5th IEEE Conference on Industrial Electronics and Applications*, 2010: IEEE, pp. 611-613, doi: 10.1109/ICIEA.2010.5517040.